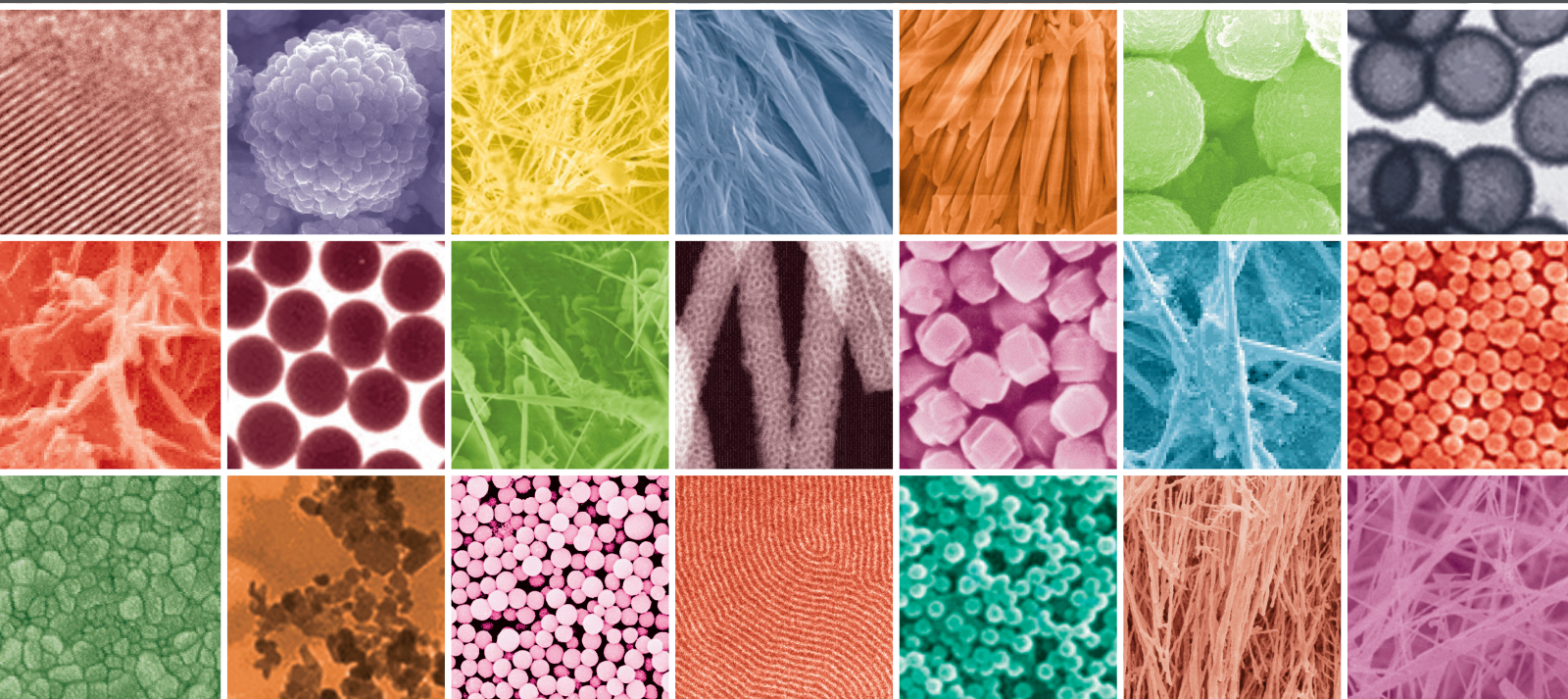
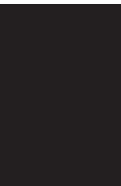


Journal of
Nanomaterials

Cancer Nanomedicine

Guest Editors: Haiyan Li, Martin M. Pike, Xiliang Luo, and Li-Hong Liu





Cancer Nanomedicine

Journal of Nanomaterials

Cancer Nanomedicine

Guest Editors: Haiyan Li, Martin M. Pike, Xiliang Luo,
and Li-Hong Liu



Copyright © 2013 Hindawi Publishing Corporation. All rights reserved.

This is a special issue published in "Journal of Nanomaterials." All articles are open access articles distributed under the Creative Commons Attribution License, which permits unrestricted use, distribution, and reproduction in any medium, provided the original work is properly cited.

Editorial Board

Katerina Aifantis, Greece
Nageh K. Allam, USA
Margarida Amaral, Portugal
Xuedong Bai, China
Lavinia Balan, France
Enrico Bergamaschi, Italy
Theodorian Borca-Tasciuc, USA
C. Jeffrey Brinker, USA
Christian Brosseau, France
Xuebo Cao, China
Sang-Hee Cho, Republic of Korea
Shafiul Chowdhury, USA
Kwang-Leong Choy, UK
Cui ChunXiang, China
Miguel A. Correa-Duarte, Spain
Shadi A. Dayeh, USA
Claude Estournés, France
Alan Fuchs, USA
Lian Gao, China
Russell E. Gorga, USA
Hongchen Chen Gu, China
Mustafa O. Guler, Turkey
John Zhanhu Guo, USA
Smrati Gupta, Germany
Michael Harris, USA
Zhongkui Hong, USA
Michael Z. Hu, USA
David Hui, USA
Y.-K. Jeong, Republic of Korea
Sheng-Rui Jian, Taiwan
Wanqin Jin, China
Rakesh K. Joshi, India
Zhenhui Kang, China
Fathallah Karimzadeh, Iran
Alireza Khataee, Iran

Do Kyung Kim, Republic of Korea
Alan K. T. Lau, Hong Kong
Burtrand Lee, USA
Benxia Li, China
Jun Li, Singapore
Xing-Jie Liang, China
Shijun Liao, China
Gong Ru Lin, Taiwan
J.-Y. Liu, USA
Jun Liu, USA
Tianxi Liu, China
Songwei Lu, USA
Daniel Lu, China
Jue Lu, USA
Ed Ma, USA
Gaurav Mago, USA
Sanjay R. Mathur, Germany
Santanu K. Maiti, India
A. McCormick, USA
Vikas Mittal, UAE
Weihai Ni, Germany
Sherine Obare, USA
Atsuto Okamoto, Japan
Abdelwahab Omri, Canada
Edward Andrew Payzant, USA
Kui-Qing Peng, China
Anukorn Phuruangrat, Thailand
Suprakas Sinha Ray, South Africa
Ugur Serincan, Turkey
Huaiyu Shao, Japan
Donglu Shi, USA
Vladimir Sivakov, Germany
Marinella Striccoli, Italy
Bohua Sun, South Africa
Saikat Talapatra, USA

Nairong Tao, China
Titipun Thongtem, Thailand
Somchai Thongtem, Thailand
Alexander Tolmachev, Ukraine
Valeri P. Tolstoy, Russia
Tsung-Yen Tsai, Taiwan
Takuya Tsuzuki, Australia
Raquel Verdejo, Spain
Mat U. Wahit, Malaysia
Shiren Wang, USA
Yong Wang, USA
Cheng Wang, China
Zhenbo Wang, China
Jinquan Wei, China
Ching Ping Wong, USA
Xingcai Wu, China
Guodong Xia, Hong Kong
Zhi Li Xiao, USA
Ping Xiao, UK
Shuangxi Xing, China
Yangchuan Xing, USA
N. Xu, China
Doron Yadlovker, Israel
Ying-Kui Yang, China
Khaled Youssef, USA
Kui Yu, Canada
William W. Yu, USA
Haibo Zeng, China
Tianyou Zhai, Japan
Renyun Zhang, Sweden
Yanbao Zhao, China
Lianxi Zheng, Singapore
Chunyi Zhi, Japan

Contents

Cancer Nanomedicine, Haiyan Li, Martin M. Pike, Xiliang Luo, and Li-Hong Liu
Volume 2013, Article ID 353941, 2 pages

Antimicrobial Activity of Hippurate Nanocomposite and Its Cytotoxicity Effect in Combination with Cytarabine against HL-60, Samer Hasan Hussein Al Ali, Mothanna Al-Qubaisi, Mohamed El Zowalaty, Mohd Zobir Hussein, and Maznah Ismail
Volume 2013, Article ID 843647, 9 pages

Nanomedicine in Action: An Overview of Cancer Nanomedicine on the Market and in Clinical Trials, Ruibing Wang, Paul S. Billone, and Wayne M. Mullett
Volume 2013, Article ID 629681, 12 pages

Nanostructured Surfaces to Target and Kill Circulating Tumor Cells While Repelling Leukocytes, Michael J. Mitchell, Carlos A. Castellanos, and Michael R. King
Volume 2012, Article ID 831263, 10 pages

Formulation of LDL Targeted Nanostructured Lipid Carriers Loaded with Paclitaxel: A Detailed Study of Preparation, Freeze Drying Condition, and In Vitro Cytotoxicity, Jaber Emami, Mahboubeh Rezazadeh, Jaleh Varshosaz, Majid Tabbakhian, and Abolfazl Aslani
Volume 2012, Article ID 358782, 10 pages

Single-Molecule Sandwich Immunoassay for Quantification of Alpha-Fetoprotein Based on Evanescent Field-Enhanced Fluorescence Imaging, Seungah Lee and Seong Ho Kang
Volume 2012, Article ID 582531, 7 pages

Semiconductor Quantum Dots Surface Modification for Potential Cancer Diagnostic and Therapeutic Applications, Jidong Wang, Shumin Han, Dandan Ke, and Ruibing Wang
Volume 2012, Article ID 129041, 8 pages

Gold Nanorod-Mediated Photothermal Modulation for Localized Ablation of Cancer Cells, Yoochan Hong, Eugene Lee, Jihye Choi, Seung Jae Oh, Seungjoo Haam, Yong-Min Huh, Dae Sung Yoon, Jin-Suck Suh, and Jaemoon Yang
Volume 2012, Article ID 825060, 7 pages

Editorial

Cancer Nanomedicine

Haiyan Li,¹ Martin M. Pike,² Xiliang Luo,³ and Li-Hong Liu⁴

¹ Department of Physics, Portland State University, Portland, OR 97207, USA

² Advanced Imaging Research Center and Department of Biomedical Engineering, Oregon Health & Science University, Portland, OR 97239, USA

³ Key Laboratory of Biochemical Analysis of Ministry of Education, College of Chemistry and Molecular Engineering, Qingdao University of Science and Technology, Qingdao 266042, China

⁴ Department of Chemistry, Portland State University, Portland, OR 97207, USA

Correspondence should be addressed to Haiyan Li; haiyanl@pdx.edu and Xiliang Luo; xiliangluo@hotmail.com

Received 7 February 2013; Accepted 7 February 2013

Copyright © 2013 Haiyan Li et al. This is an open access article distributed under the Creative Commons Attribution License, which permits unrestricted use, distribution, and reproduction in any medium, provided the original work is properly cited.

Bioengineered nanomaterials have inspired revolutionary imaging and drug delivery methods whose clinical application in cancer research has resulted in powerful medical devices for early diagnosis, treatment, and prevention of cancer. Recent advances in super imaging agents have resulted in improved resolution and sensitivity. For instance, fluorescent quantum dots with wavelength-tunable emissions, plasmon-resonant gold nanostructures with shape-controlled near-infrared absorptions, and MRI-active iron oxide nanoparticles are well-established molecular imaging probes for noninvasive cancer imaging. Nanomaterials are also considered to be the most effective vectors that can break through transport biobarriers and deliver a constant dose of multiple therapeutic agents to tumors and intracellular endocytic compartments for cancer gene therapy, immunotherapy, or chemotherapy. Furthermore, nanowire- or nanotube-based electronic devices demonstrate extraordinary sensitivity capable of detection at the single molecule or protein level. It is anticipated that developing nanotechnology-driven imaging, sensing, and therapeutic systems will dramatically advance cancer research and clinical treatments.

We organized this special issue aiming to visualize the current progress in the emerging multidisciplinary field of cancer nanomedicine. We specifically invited Dr. R. Wang and his colleagues to analyze the trend of cancer nanomedicine development. In a review, they examined a dozen cases of particulate nanomedicine for cancer therapeutics or diagnostics applications. At least ten kinds of cancer nanomedicines have been approved by regulatory bodies to

be commercialized for clinical use, and many therapeutic or theranostics cancer nanomedicines have been involved in clinical trials. These encouraging facts show that cancer nanomedicine is in action, although many technical issues need to be addressed and it is still a big challenge to meet safety guidelines for gaining clinical acceptance.

Next, we focus on some technique issues. For example, surface modification is required to stabilize and functionalize fluorescent quantum dots for cancer diagnostic and therapeutic applications. J. Wang et al. summarized some recent progress and strategies to modify quantum dots, such as silanization, ligand exchange, and amphiphilic polymer coatings. These solutions will be applied to optimize the interface chemistry of quantum dots for potential biological applications of bioimaging and drug delivery.

In a research article, J. Emami et al. demonstrated the fabrication of paclitaxel-loaded cholesterol nanostructured lipid carriers and characterization by measuring the size, zeta potential, entrapment efficiency, drug loading capacity, and drug release profiles of the carriers. The results indicate that the size of carriers is associated with oleic acid content and surfactant percent, and the ratio of drug payload to lipid weight significantly affects the entrapment efficiency and drug release from carriers.

In another research article, S. H. H. Ali et al. synthesized hippuric acid nanocomposite by intercalating hippuric acid into zinc-layered hydroxide. Compared to cytarabine alone, coupling cytarabine with hippuric acid nanocomposite has higher therapeutic efficacy against human promyelocytic

leukemia cells. In addition, hippuric acid nanocomposite demonstrated the capability against bacteria, such as *Pseudomonas aeruginosa* and methicillin-resistant *Staphylococcus aureus*.

Recently, gold nanorods have become a rising star in cancer medicine, because under near-infrared light, the geometry-related photothermal effect enables gold nanorods to provide optical coherence tomography contrast for non-invasive cancer imaging and to ablate targeting cancer cells. In a research article, Y. Hong et al. systematically investigated how gold nanorod concentration and irradiation laser power affect the photothermal transduction efficiency of gold nanorod suspension. The therapeutic efficacy of gold nanorod-mediated ablation is estimated using MDA-MB-231 breast cancer cell line by live-dead cell staining. They also developed a versatile system that can simultaneously monitor the temperature variation, uptake of photothermal agents, and the targeting cell viability.

Toward cancer immunotherapy, a gold nanoparticle array-based sensor on chip fabricated by S. Lee and S. H. Kang can accurately detect immunomolecules by measuring the fluorescence signal from the interaction between the gold nanoparticle-captured biotin-labeled antibody and a streptavidin-labeled dye. The developed single-molecule sandwich immunoassay is simple, reliable, and sensitive (40,000-fold higher than conventional chemiluminescence immunosensors).

Interestingly, besides particulate cancer nanomedicines, M. J. Mitchell et al. demonstrated a unique device that can selectively capture and kill flowing cancer cells using microtube surfaces with immobilized halloysite nanotubes and E-selectin functionalized liposomal doxorubicin, without toxic effects on health cells. This nonparticulate cancer nanomedicine opens a new path to conduct cancer diagnosis and treatment.

The diverse and vigorous investigations published in this special issue clearly show that cancer nanomedicine is revolutionizing the field of medicine for cancers.

Haiyan Li
Martin M. Pike
Xiliang Luo
Li-Hong Liu

Research Article

Antimicrobial Activity of Hippurate Nanocomposite and Its Cytotoxicity Effect in Combination with Cytarabine against HL-60

Samer Hasan Hussein Al Ali,¹ Mothanna Al-Qubaisi,¹ Mohamed El Zowalaty,²
Mohd Zobir Hussein,³ and Maznah Ismail^{1,4}

¹Laboratory of Molecular Biomedicine, Institute of Bioscience, Universiti Putra Malaysia, 43400 Serdang, Selangor, Malaysia

²Laboratory of Vaccines and Immunotherapeutics, Institute of Bioscience, Universiti Putra Malaysia, 43400 Serdang, Selangor, Malaysia

³Materials Synthesis and Characterization Laboratory (MSCL), Institute of Advanced Technology, Universiti Putra Malaysia, 43400 Serdang, Selangor, Malaysia

⁴Department of Nutrition and Dietetics, Faculty of Medicine and Health Science, Universiti Putra Malaysia, 43400 Serdang, Selangor, Malaysia

Correspondence should be addressed to Mohd Zobir Hussein; mzobir@putra.upm.edu.my

Received 27 August 2012; Revised 27 November 2012; Accepted 28 November 2012

Academic Editor: Xiliang Luo

Copyright © 2013 Samer Hasan Hussein Al Ali et al. This is an open access article distributed under the Creative Commons Attribution License, which permits unrestricted use, distribution, and reproduction in any medium, provided the original work is properly cited.

Hippuric acid (HA) was intercalated into a zinc-layered hydroxide (ZLH) by direct reaction of an aqueous suspension of zinc oxide with an aqueous solution of hippuric acid to obtain hippurate nanocomposite (HAN). Various concentrations of hippuric acid (0.05, 0.2, and 0.4 molar) were used for the synthesis of the nanocomposite. The as-synthesized HAN using 0.2 molar was found to give a well-ordered layered nanocomposite material with an increase in the basal spacing to 21.3 Å which indicated the insertion of hippurate organic moiety into the ZLH interlayers. The cytotoxicity of HAN in combination with cytarabine against human promyelocytic leukemia cells (HL-60) was tested using MTT cell viability assay and trypan blue dye exclusion assay. The combination of cytarabine with HAN showed higher tumor suppression efficiency as compared to that of cytarabine alone. The IC₅₀ values of HAN/cytarabine combination and cytarabine alone were 0.16 ± 0.07 µg/mL and 0.17 ± 0.09 µg/mL, respectively. DNA fragmentation was also studied, and the exposure of HL-60 cells to cytarabine produced 10.70 ± 0.96% DNA fragmentation compared to 18.90 ± 1.33% when cells were exposed to combination of cytarabine with HAN. The antimicrobial activity of hippuric acid and HAN nanocomposite was carried out against Gram-positive bacteria, Gram-negative bacteria, and yeasts. It was found that *Pseudomonas aeruginosa* and methicillin-resistant *Staphylococcus aureus* were more sensitive to HAN compared to *Bacillus subtilis* and *Salmonella choleraesuis*.

1. Introduction

Metal hydroxide compounds can be classified according to their structures and chemical compositions into two groups. The first group is the layered double hydroxide (LDH) derived from the brucite structure (Mg(OH)₂) through substitution part of the divalent cations by the trivalent ones. As a result, the layers acquire excess positive charge, which is balanced by the incorporation of anions into the interlayer space. The general formula may be thus given as (LDH –

$M_{1-x}^{2+}M_x^{3+}(\text{OH})_2(\text{A}^{m-})_{x/m} \cdot n\text{H}_2\text{O}$), where M²⁺ is divalent cations, M³⁺ is trivalent cations, and A^{m-} is exchangeable anion with a charge (m⁻) [1]. The second group is the metal hydroxide compounds which are layered metal hydroxide salt (LHS) that can be represented by the general formula (LHS – M²⁺(OH)_{2-x}(A^{m-})_{x/m} · nH₂O) [2]. The interlayer anion exchangeable capability of LDH and LHS meets the requirement of inorganic layers for encapsulating organic drugs with negative charge and is used in drug delivery applications [3], as well as controlled release systems [4–7].

Zinc layered hydroxide (ZLH) is an example of the layered hydroxide salt in which zinc atoms are octahedrally coordinated with six hydroxide groups to give an empirical formula of $Zn_5(OH)_8(NO_3)_2 \cdot 2H_2O$ [8].

Our previous work showed that hippuric acid intercalated into zinc layered hydroxide potentiated the cytotoxicity of tamoxifen against hepatocellular carcinoma HepG2 [9]. The present study was conducted to investigate whether HAN could enhance the toxic effect for cytarabine, another chemotherapy used commonly to treat human promyelocytic leukemia. A parallel to that, antimicrobial activity of HAN nanocomposite against different micro-organisms was also determined.

2. Materials

Hippuric acid ($C_9H_9NO_3$) with 98% purity was purchased from Merck and was used as received. Cytarabine ($C_9H_{13}N_3O_5$) with 99% purity was purchased from Bioscience (Tocris, Bristol, UK). Zinc oxide of the American chemical society reagent grade was purchased from Fisher Scientific, and dimethyl sulfoxide (DMSO) was purchased from Ajax Finechem and used without further purification. Diphenylamine reagent containing 100 mL glacial acetic acid, 1.5 g diphenylamine, 1.5 mL concentrated sulfuric acid, and 0.5 mL 16 mg/mL acetaldehyde stock and trypan blue solution were purchased from Sigma-Aldrich. The cell line HL-60 was purchased from the American type culture collection (ATCC number CCL-240). Deionized water was used in all the experiments. The microbial strains were provided by the UNiCC, Institute of Bioscience, Universiti Putra Malaysia.

3. Preparation of Hippurate Nanocomposite, HAN

Hippurate nanocomposite (HAN) was synthesized by direct reaction using zinc oxide (ZnO) as the starting material as reported previously [9–11]. The concentrations of hippuric acid of 0.05, 0.2, and 0.4 molar were prepared using appropriate weights of active material in 20 mL of DMSO and adjusting the final volume to 50 mL by the addition of deionized water. A weight of 0.2 g of zinc oxide was suspended in 50 mL water. Hippurate solutions were added slowly dropwise to the suspended zinc oxide, with vigorous stirring until the addition was completed and the solution became clear; the pH was adjusted to 7.9 using an aqueous solution of NaOH (0.5 molar). The resulting precipitate was magnetically stirred for 18 hours at 70°C and washed with deionized water. Finally, the as-synthesized HAN was dried in an oven at 60°C overnight and kept in a sample bottle for further characterizations.

4. MTT Cytotoxicity Assay

Human promyelocytic leukemia (HL-60) cells were used in the present study. Cells were routinely cultured at 37°C a humidified atmosphere with 5% CO₂ in 96-well plates for 24 hours. When cells were grown up to 80%–90% of

cellular confluence, the cells were treated with cytarabine alone and an equivalent cytostatic mixture of either hippuric acid or HAN. After 72 hours of incubation in a humidified atmosphere with 5% CO₂ at 37°C, MTT assay with 3-(4,5-dimethylthiazole-2-yl)-2, 5-diphenyltetrazolium bromide was carried out with incubation times to determine the number of viable cells. Twenty microliters of MTT was added to all wells, and the cells were incubated for an additional 4 hours. After incubation, the upper part of the solution was removed to leave 30 µL in all wells, and the formazan precipitate was dissolved in 10% sodium dodecyl sulfate in dimethyl sulfoxide containing 0.6% acetic acid. The microplates were then gently shaken in the dark for 30 minutes, and the absorbance at 570 nm and 630 nm (background) was measured spectrophotometrically using a microtiter plate reader. All experiments were carried out in triplicate. The IC₅₀ was generated from the dose-response curves for the cell line. MTT assay of HL-60 cells treated with a combination of doxorubicin with hippuric acid and HAN was used as positive control.

5. Antiproliferative Assay

Human promyelocytic leukemia (HL-60) cells were used; the cells were seeded at a density of 1×10^5 viable cells/mL in six-well plates. After incubation for 24 hours, the cells were treated with cytarabine (0.5 µg/mL) alone and its combination with hippuric acid or HAN. The plates were incubated at 37°C in the presence of 5% CO₂, for 24, 48, and 72 hours. After incubation, the media were aspirated off, and cells were washed with cold PBS buffer to get rid of dead cells and replaced with 1 mL of 0.05% trypsin-EDTA (2 mg/mL). The plates were incubated at 37°C for 10–15 minutes, until the majority of the cells were detached. The cells were harvested, and the cell suspension was centrifuged at 1000 rpm for 10 minutes, and the supernatant discarded. Twenty microliters of cell suspension was mixed with 20 µL of 0.4% trypan blue solution. Cells were resuspended, and dye-excluding viable cells were microscopically counted using a hemocytometer.

6. Examination of DNA Fragmentation

DNA fragmentation was quantitatively determined using diphenylamine reagent for cells treated with 1 µg/mL cytarabine alone and in equal combination with either 1 µg/mL hippuric acid or 1 µg/mL HAN. A volume of 108 µL of 5 molar perchloric acid was added, and samples were heated at 70°C for 15 min. Two volumes of a solution containing diphenylamine reagent were added, and the samples were stored at 4°C for 48 hours. The colorimetric reaction was determined spectrophotometrically at 575 nm using a UV spectrophotometer (UV-160A; Shimadzu Co. Ltd., Tokyo, Japan). DNA aliquots from both pellet and supernatant were quantified. The degree of DNA fragmentation referred to the percentage of DNA in the supernatant divided by the total DNA from the pellet and supernatant was determined.

7. Microbial Strains and Cultural Conditions

Four well-characterized species of bacteria including two Gram-positive micro-organisms: methicillin-resistant *Staphylococcus aureus* (MRSA) and *Bacillus subtilis* and two Gram-negative species: *Salmonella choleraesuis* and *Pseudomonas aeruginosa*, and yeast: *Candida albicans* were used in the screening of the synthesized HAN. Cultures were maintained on Luria-Bertani (LB) agar (1st Base, Singapore) or potato dextrose agar in case of yeast. Prior to incubation with nanoparticles, the bacteria were cultured overnight in 5 mL of LB broth (1st Base, Singapore) in a Certomat SII incubation shaker (Sartorius Stedim Biotech, Aubagne, France) at 37°C and 150 rpm until the culture reached an OD₆₀₀ of 1.0 (Ultrospec UV VIS 3000 pro, Amersham Pharmacia Biotech, Cambridge, England) corresponding to approximately 10⁸ CFU mL⁻¹. The overnight cultures were diluted to approximately 10⁷ CFU mL⁻¹ using sterile LB broth.

8. Antimicrobial Activity Testing

The antimicrobial properties of the HAN nanocomposite were evaluated against the aforementioned micro-organisms using the disk diffusion method as described previously [12]. Microorganisms were cultured in LB broth in case of bacteria (1st Base, Singapore) or potato dextrose broth (Fluka) in case of yeast to achieve a culture growth turbidity of 1 by measuring optical density (OD) spectrophotometrically at 600 nm. The suspension of each micro-organism was serially diluted in LB broth to a concentration of 1 ~ 2 10⁴ CFU/mL. The inhibitory activity was read after 24 hours of incubation at 37°C. HAN-free discs (distilled water only) cultured under the same conditions were used as a control.

9. Characterization

Powder X-ray diffraction patterns were recorded with a Shimadzu XRD-6000 instrument (Shimadzu, Tokyo, Japan) using CuK α radiation ($\lambda = 1.5418 \text{ \AA}$) and a dwell time of 4 degrees per minute. Cell count was carried using Neubauer hemocytometer (Weber, England) using clear field microscopy (Nikon, Japan). The bacteria were cultured overnight in a Certomat SII incubation shaker (Sartorius Stedim Biotech, Aubagne, France). UV spectrophotometer (UV-160A; Shimadzu Co. Ltd., Tokyo, Japan) was used in the determination of DNA fragmentation.

10. Results and Discussion

10.1. Powder X-Ray Diffraction. Figures 1(a) and 1(e) show PXRD patterns of the ZnO and free hippuric acid, respectively. In addition, Figures 1(b)–(d) show hippurate nanocomposites prepared using various concentrations of hippuric acid: 0.05, 0.2, and 0.4 molar, respectively. As shown in Figure 1(a), the ZnO sample shows five intense reflections between 30–60° correspond to diffractions due to 100, 002, 101, 102, and 110 planes [13]. It was reported previously that the basal spacing for zinc layered hydroxide with nitrate

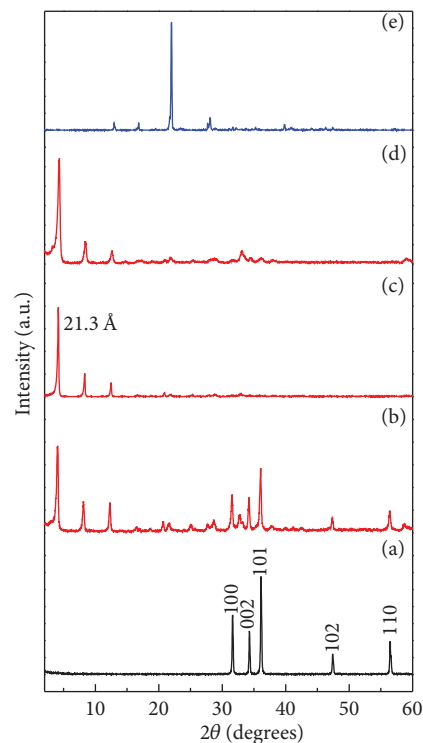


FIGURE 1: PXRD patterns for ZnO (a), hippurate nanocomposite prepared at various concentrations of hippuric acid (0.05, 0.2, and 0.4 molar for (b), (c), and (d), resp.), and free hippuric acid (e).

(ZLH) as the interlamella anion was 9.74 Å which appeared at $2\theta = 9.12$ due to the 200 plane of the monoclinic structure [14]. The PXRD pattern for HAN is shown in Figure 2(c) with basal spacing of 21.3 Å. The expansion of basal spacing from ZLH to HAN was due to the inclusion of hippuric acid anion, namely, hippurate into the ZLH lamella with a vertical monolayer orientation that warrants the expansion of the ZLH lamella [9]. This can only be achieved when suitable concentration of hippuric acid is available in the mother liquor, under the experimental conditions as stated earlier. At Figure 1(d) HAN prepared using 0.4 molar hippuric acid, a number of peaks are observed due to hippuric acid phase. This might be due to the non-intercalated hippuric acid, which was adsorbed onto the surface of ZLH. HAN prepared using 0.05 molar hippuric acid shows the presence of ZnO phase. HAN prepared using 0.2 molar hippuric acid produced sharp, symmetrical, and intense peaks, especially for the (003) peak, and the relatively pure intercalated compound was obtained at this concentration. As a result of relatively pure phase, HAN prepared from 0.2 molar hippuric acid was subsequently used for further characterizations.

10.2. Cytotoxicity of Combination of HAN with Cytarabine. Figure 2 shows the cytotoxicity of hippuric acid, HAN nanocomposite, and their combinations with cytarabine against HL-60 cells. The cytotoxicity of cytarabine was investigated using human promyelocytic (HL-60) cells as described previously [15]. The hippuric acid and HAN

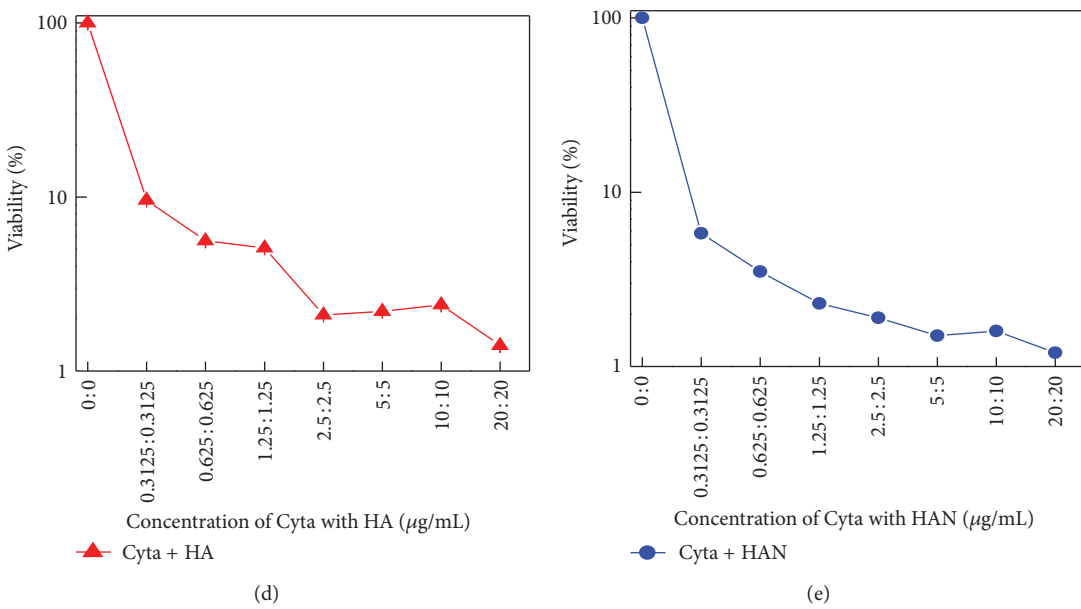
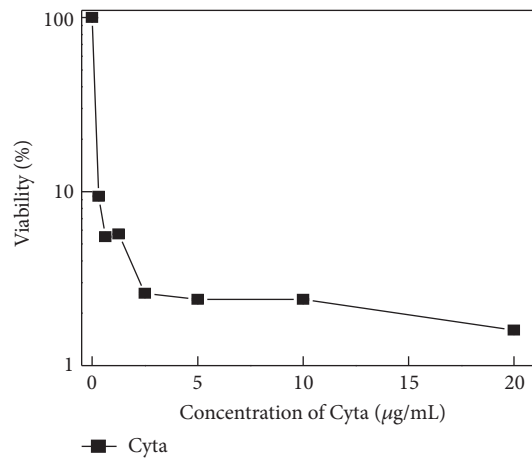
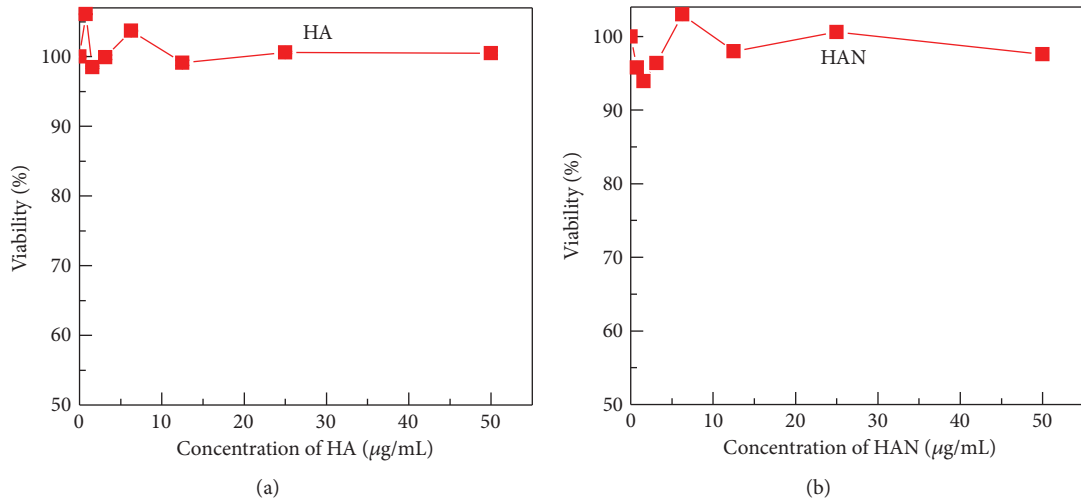


FIGURE 2: MTT assays of HL-60 cell line treated with free hippuric acid, HAN and the combination of cytarabine with hippuric acid and HAN.

TABLE 1: Viability of HL-60 cells during incubation with cytarabine, combination of cytarabine with hippuric acid, and cytarabine with HAN nanocomposite.

Concentration of Cyta ($\mu\text{g/ml}$)	Viability (%)	Concentration of Cyta : HA or HAN ($\mu\text{g/ml}$)	Viability (%)	
			HA	HAN
20.0	1.6	20 : 20	1.4	1.2
10.0	2.4	10 : 10	2.4	1.6
5.0	2.4	5 : 5	2.2	1.5
2.5	2.6	2.5 : 2.5	2.1	1.9
1.25	5.7	1.25 : 1.25	5.1	2.3
0.625	5.5	0.625 : 0.625	5.6	3.5
0.3125	9.4	0.3125 : 0.3125	9.6	5.8
0.00	100.0	0 : 0	100.0	100.0

TABLE 2: IC_{50} for HL-60 cells during incubation with cytarabine, doxorubicin, and combination of drugs with hippuric acid and with HAN nanocomposite.

	Cytarabine			Doxorubicin		
	Cyta	Cyta + HA	Cyta + HAN	Doxo	Doxo + HA	Doxo + HAN
IC_{50}	$0.17 \pm 0.09 \mu\text{g/mL}$	$0.17 \pm 0.07 \mu\text{g/mL}$	$0.16 \pm 0.07 \mu\text{g/mL}$	$2.70 \pm 0.07 \mu\text{g/mL}$	$1.80 \pm 0.11 \mu\text{g/mL}$	$1.03 \pm 0.19 \mu\text{g/mL}$

TABLE 3: Antiproliferative assays of HL-60 cells after 24, 48, and 72 hours treatment with cytarabine alone and combination of cytarabine with hippuric acid and HAN nanocomposite.

Incubation time	HL-60		
	Cytarabine	Cytarabine + HA	Cytarabine + HAN
24 hours	83.50%	82.40%	88.20%
48 hours	91.40%	91.40%	95.10%
72 hours	95.50%	95.10%	97.40%

nanocomposite, up to a concentration of $50 \mu\text{g/mL}$ did not show any inhibition in the cell growth of treated HL-60 cells (Figures 2(a) and 2(b)). In the absence of hippuric acid or HAN (Figure 2(c)), the cytarabine suppressed the growth of HL-60 cells with IC_{50} values of $0.17 \pm 0.09 \mu\text{g/mL}$. As shown in Figure 2(d) and Table 1, the combination of hippuric acid with cytarabine show inhibition in the cell growth, similarly with cytarabine action and with IC_{50} $0.17 \pm 0.07 \mu\text{g/mL}$.

The combination of cytarabine with HAN (Figure 2(e)) shows slightly higher tumor suppression as compared to cytarabine alone with IC_{50} values of $0.16 \pm 0.07 \mu\text{g/mL}$. This indicate that the suppression percentage using HAN reached 4.1%. A detailed look at Table 1, the results of MTT assay show that HAN exposure potentiates the toxic activity of cytarabine in HL-60 cells in a dose-dependent manner, and the lowest two combinations ($0.62 \mu\text{g/mL}$ and $0.31 \mu\text{g/mL}$) show the most notable effect.

Furthermore, compared with cytarabine, doxorubicin (Doxo) showed lower cytotoxicity toward the HL-60 cell line (Figures 3(a)–3(c)). Table 2 shows the IC_{50} values for the combination of cytarabine and doxorubicin with hippuric acid and HAN nanocomposite.

10.3. Antiproliferative Effect of Cytarabine Alone and Combinations of Cytarabine with Hippuric Acid and HAN. Figure 4(a) shows the effect of free cytarabine or in

combination with hippuric acid and HAN on the proliferation of HL-60 cells at various incubation periods 24, 48, and 72 hours. Cytarabine and its combination with HAN suppressed the proliferation of HL-60 tumor cells. The combination of the drug with HAN was more efficient than the free drug in suppressing the tumor cells.

As shown in Table 3 at 24 hours, the combination of cytarabine with HAN showed 88.20% suppression of the proliferation as compared to the free cytarabine, which showed only 83.50% suppression. Additionally, at 72-hour treatment, the growth suppression for cytarabine with HAN showed 97.40%, compared to 95.50% for free cytarabine.

The result in Figure 4(b) confirmed that the combination of cytarabine with HAN can inhibit the cell proliferation more than doxorubicin with HAN.

In general, the current study showed that HAN did not potentiate the toxicity of cytarabine. However, these results are clearly distinct from our previous findings with tamoxifen, in which HAN showed a dramatic inhibition of HepG2 cell proliferation [9].

10.4. Examination of DNA Fragmentation. DNA fragmentation is an important feature of nucleus that occurs in the apoptotic process. It is worth mentioning that Bouffard and Momparler have studied the effect of cytarabine versus DNA damages in leukemic cell HL60 line. Cytarabine at $5 \mu\text{m}$

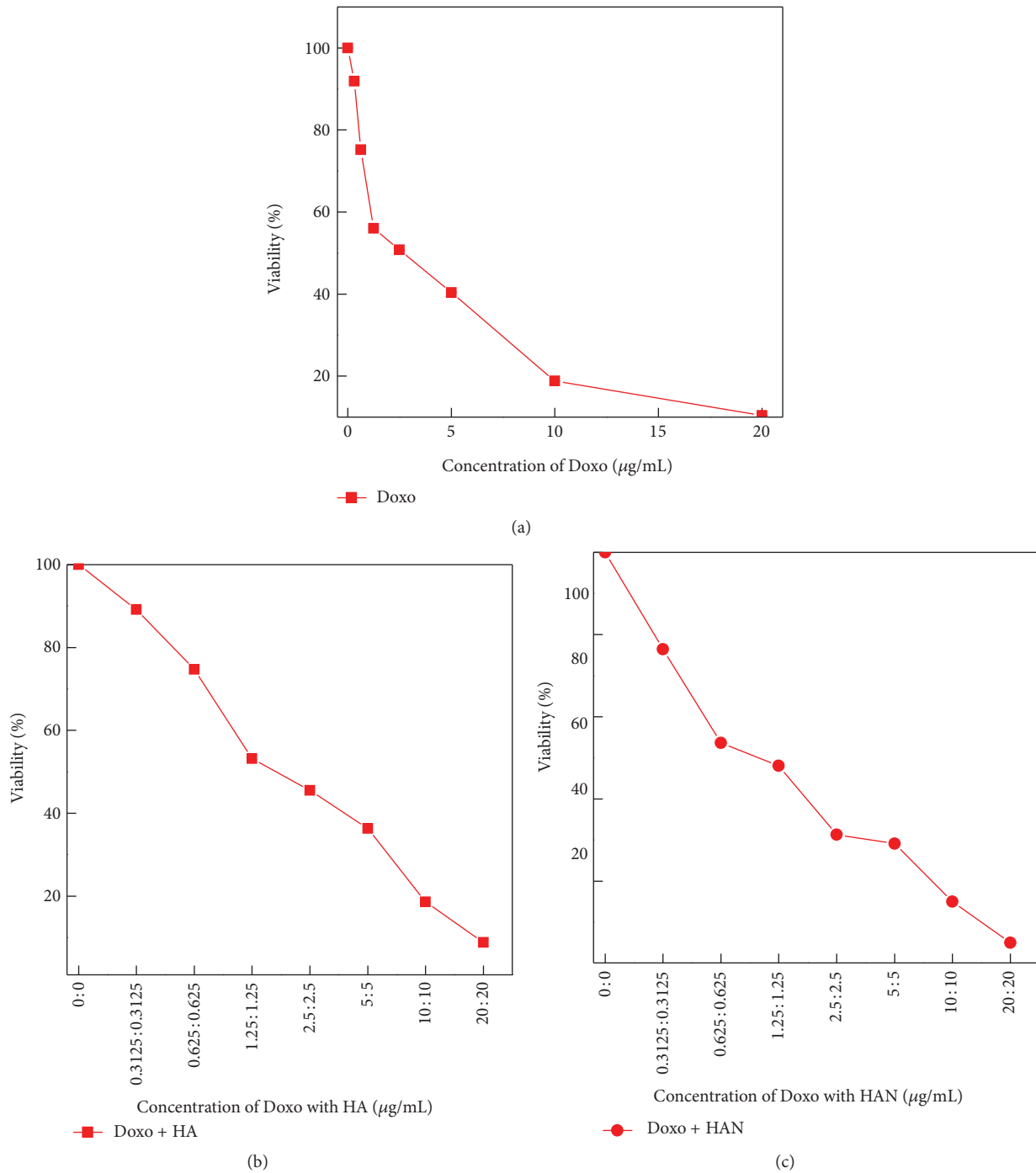


FIGURE 3: MTT assays of HL-60 cell line treated with a combination of doxorubicin with hippuric acid and HAN as positive control.

showed DNA fragmentation, verified by DNA ladder assay [16]. These nuclear changes were investigated in the presence and the absence of hippuric acid or HAN in the presence of cytarabine.

The degree of DNA fragmentation in the untreated control and in cells exposed to the drugs for 72 hours is shown in Figure 5. The fragmentation background in the untreated control was approximately $2.00 \pm 0.26\%$. Both

cytarabine alone and its combination of hippuric acid exhibited an increase in a similar manner through a significant increase in percentage of DNA fragmentation by $10.70 \pm 0.96\%$ and $10.80 \pm 1.10\%$, respectively, as compared to an untreated group without any marked difference as a result of the combination. The double-stranded DNA fragmentation has generally occurred with $18.90 \pm 1.33\%$ when HL-60 cancer cells are exposed to an equal combination of cytarabine

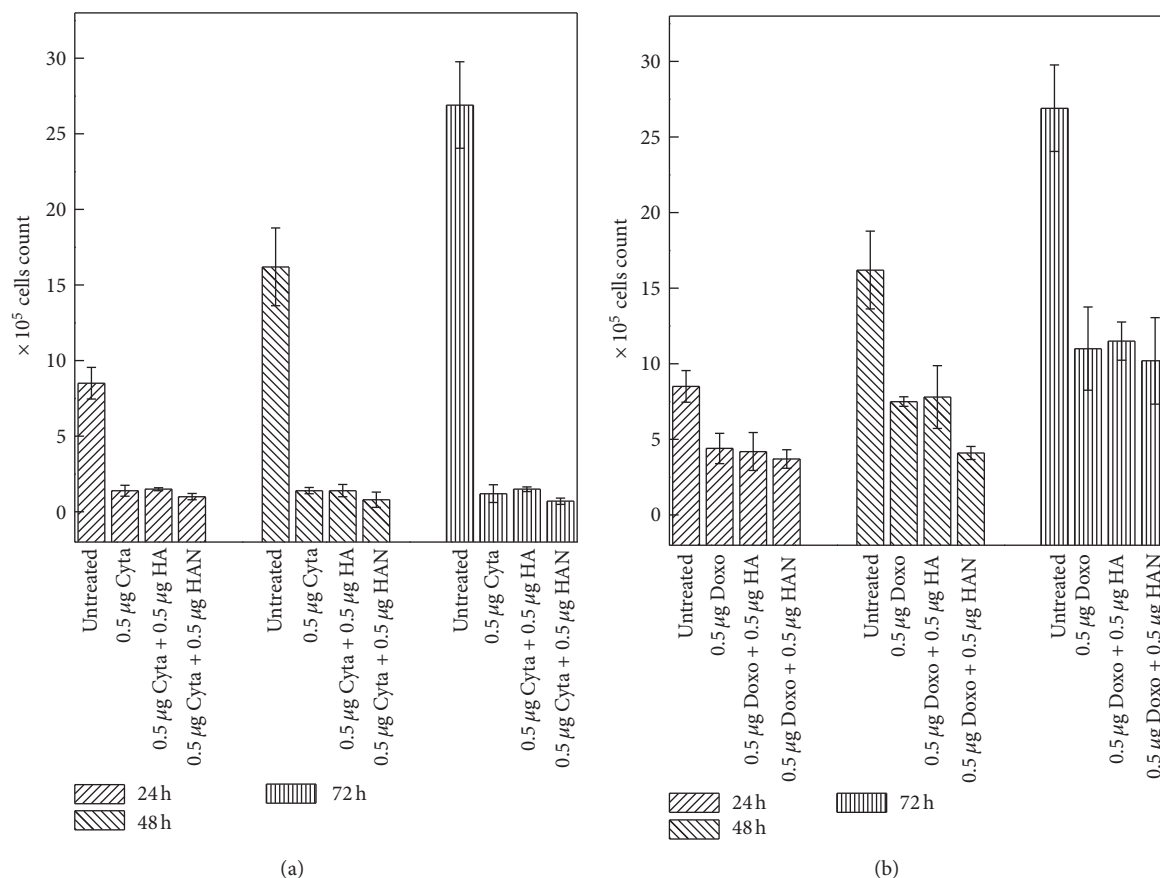


FIGURE 4: Antiproliferative assays of HL-60 cell line after, 24, 48, and 72 hours of treatment with free cytarabine and a combination of free cytarabine with hippuric acid and HAN (a) and positive control using doxorubicin (b).

TABLE 4: Antimicrobial activities of hippuric acid and HAN nanocomposite against different microorganisms after 24 hours treatment*.

Sample	SC	BS	PA	MRSA	CA
HA	8	13	11	10	9
HAN	7	7	10	8	7

SC: *Salmonella choleraesuis*; BS: *Bacillus subtilis*; PA: *Pseudomonas aeruginosa*; MRSA: methicillin-resistant *Staphylococcus aureus*; CA: *Candida albicans*; HA: hippuric acid; HAN: hippurate nanocomposite.

*Diameters of zones of inhibition were measured to nearest mm.

to HAN concentration. This result provides a rationale for the synergistic property of HAN when combined with cytarabine more than that was observed in MTT results. This indicates that drug delivery to the tumor cell was noticeably enhanced by nanocomposite with ZLH. In the nanocomposite system, however, drugs can reach the tumor cell membrane without any early decomposition, since the drug is stabilized and protected in the interlayer space of the ZLH layers. This result clearly confirmed that the intercalation reaction not only resulted in avoidance of drug denaturation but also enhanced the permeability of the drug into the target cells without any noticeable side effects [17].

10.5. Antimicrobial Activity of Hippuric Acid and Its HAN Nanocomposite. There were many previous studies reported on the antimicrobial activity of hippuric acid [18–22]. The

effect of HAN against different microorganisms is reported in the present study. The work principle depends on the measurement of the diameter of inhibition zones where the increase in the inhibition zone indicating the highest antimicrobial activity. HAN exhibited antimicrobial activity against the tested organisms by showing the clear inhibition zones using the disk diffusion method. The diameters of the inhibition zone are shown in Table 4. Similar to antibiotic sensitivity testing, the antimicrobial activity of the hippuric acid against different microorganisms was determined using the disk diffusion method, employing the nanoparticles impregnated disks.

In the present study, 100 μ g/mL suspension of hippuric acid and 25 μ g/mL suspension of HAN were used to impregnate 6 mm diameter sterilized filter paper disks. The nanocomposite laden disks were placed on the surface of

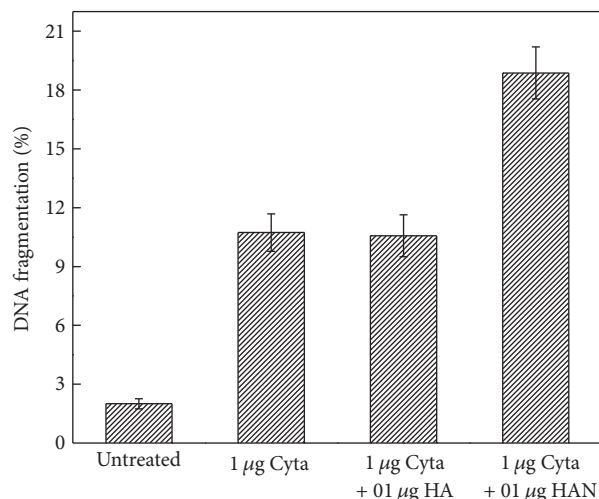


FIGURE 5: DNA fragmentation percentage of HL-60 cell line after 72 hours by cytarabine and combinations of cytarabine with hippuric acid and HAN.

LB agar plates containing the tested microorganism. The microbial suspension ($100 \mu\text{L}$ of 10^4 CFU mL^{-1}) was applied uniformly on the surface of the dried LB agar plates in case of bacteria or potato dextrose agar plates in case of yeast before placing the disks on the plate (3 plates per microorganism). The plates were incubated at 37°C for 24 hours. At the end of the incubation period, the average diameter (mm) of the inhibition zone surrounding the disk was measured using a ruler with up to 1 mm resolution.

The most susceptible organisms to the hippuric acid were *Bacillus subtilis* and *Pseudomonas aeruginosa*. In addition, *Pseudomonas aeruginosa* and methicillin-resistant *Staphylococcus aureus* were more sensitive to HAN as compared to other micro-organisms, and this might be attributed to the smaller particle size of HAN as compared to hippuric acid alone. The small particle size of HAN allowed more drug uptake by Gram-negative bacteria. As shown in Table 4, hippuric acid and HAN show similar antimicrobial activity against all the tested organisms, although hippuric acid shows a slightly larger zone of inhibition than HAN. This might be attributed to that HAN is known of slow release of active hippuric acid.

It is worth mentioning that *Pseudomonas aeruginosa* and MRSA are major pathogens causing problematic infections in human and animals such as septicemia, wound, burns, and deadly infections [23, 24]. In addition, these two pathogens are known of multidrug resistance to several classes of currently used antibiotics making the treatment process problematic and concerning [25, 26]. Nanointercalation of $9.5 \mu\text{g}$ hippuric acid (38% of the $25 \mu\text{g}$ HAN) between two zinc-layered hydroxide (ZLH) increases its efficacy and exhibits the approximate reduction of $100 \mu\text{g/mL}$ hippuric acid in bacterial growth after 24 hours exposure as seen in *Pseudomonas aeruginosa*. The application of HAN would improve control of infections caused by these pathogens by its slow release of antibacterial activity. Our results were in accordance with the prospective importance of nanoparticles

in the treatment of bacterial infections and nanomedicine [27, 28].

11. Conclusion

A new nanocomposite compound in which hippuric acid is intercalated into the interlayer of zinc layered hydroxide was synthesized by direct reaction of zinc oxide aqueous suspension with anions of hippuric acid. The resulting phase pure nanocomposite was synthesized using 0.2 molar hippuric acid and had a basal spacing of 21.3 \AA . The combination of cytarabine with HAN showed higher tumor suppression efficiency compared to cytarabine alone with IC_{50} values $0.165 \pm 0.070 \mu\text{g/mL}$. The exposure of HL-60 cancer cells to cytarabine alone resulted in $10.70 \pm 0.96\%$ DNA fragmentation compared to $18.90 \pm 1.33\%$ in the case of combination of cytarabine with HAN. Furthermore, the HAN nanocomposite showed antimicrobial activity against *Pseudomonas aeruginosa* and methicillin-resistant *Staphylococcus aureus*.

Conflict of Interests

The authors declare that they have no conflict of interests in this work.

Acknowledgments

The authors would like to thank the Ministry of Higher Education of Malaysia for financial support under Grant no. FRGS/1/11/SG/UPM/01/2 (Vot. 5524165) and to the Malaysian International Scholarship (MIS) for Financial support of Dr. MEZ, from the department of Microbiology and Immunology, Faculty of Pharmacy, Zagazig University, Egypt, through a postdoctors scholarship.

References

- [1] V. Rives, *Layered Double Hydroxides: Present and Future*, Nova Science, New York, NY, USA, 2001.
- [2] G. G. C. Arizaga, K. G. Satyanarayana, and F. Wypych, "Layered hydroxide salts: synthesis, properties and potential applications," *Solid State Ionics*, vol. 178, no. 15–18, pp. 1143–1162, 2007.
- [3] K. Ladewig, P. X. Zhi, and Q. L. Gao, "Layered double hydroxide nanoparticles in gene and drug delivery," *Expert Opinion on Drug Delivery*, vol. 6, no. 9, pp. 907–922, 2009.
- [4] S. Aisawa, "Nucleotide transport efficiency to leukemia cells by layered double hydroxide," *Kagaku to Kogyo*, vol. 55, no. 7, p. 809, 2002.
- [5] J. H. Choy, M. Park, and J. M. Oh, "Bio-nanohybrids based on layered double hydroxide," *Current Nanoscience*, vol. 2, no. 3, pp. 275–281, 2006.
- [6] J. H. Choy, "Biological hybrid materials for drug delivery system," *Solid State Phenomena*, vol. 111, pp. 1–6, 2006.
- [7] J. H. Choy and M. Park, "Nanohybridization of biomolecules with layered double hydroxides and hydroxy double salts for advanced applications," *Clay Science*, vol. 12, pp. 52–56, 2005.
- [8] M. Louer, D. Louer, and D. Grandjean, "Etude structurale des hydroxynitrates de nickel et de zinc. I. Classification

- structurale,” *Acta Crystallographica B*, vol. 29, pp. 1696–1703, 1973.
- [9] S. H. H. Al Ali, M. Al-Qubaisi, M. Z. Hussein, Z. Zainal, and M. N. Hakim, “Preparation of hippurate-zinc layered hydroxide nanohybrid and its synergistic effect with tamoxifen on HepG2 cell lines,” *International Journal of Nanomedicine*, vol. 6, pp. 3099–3111, 2011.
- [10] S. H. Al Ali, M. Al-Qubaisi, M. Z. Hussein, M. Ismail, Z. Zainal, and M. N. Hakim, “Controlled-release formulation of antihistamine based on cetirizine zinc-layered hydroxide nanocomposites and its effect on histamine release from basophilic leukemia (RBL-2H3) cells,” *International Journal of Nanomedicine*, vol. 7, pp. 3351–3363, 2012.
- [11] M. Z. Hussein, S. H. Al Ali, Z. Zainal, and M. N. Hakim, “Development of antiproliferative nanohybrid compound with controlled release property using ellagic acid as the active agent,” *International Journal of Nanomedicine*, vol. 6, pp. 1373–1383, 2011.
- [12] J. M. Andrews, “BSAC standardized disc susceptibility testing method,” *Journal of Antimicrobial Chemotherapy*, vol. 48, no. 1, pp. 43–57, 2001.
- [13] M. Yin, Y. Gu, I. L. Kuskovsky et al., “Zinc oxide quantum rods,” *Journal of the American Chemical Society*, vol. 126, no. 20, pp. 6206–6207, 2004.
- [14] S. P. Newman and W. Jones, “Comparative study of some layered hydroxide salts containing exchangeable interlayer anions,” *Journal of Solid State Chemistry*, vol. 148, no. 1, pp. 26–40, 1999.
- [15] J. M. Leclerc and R. L. Momparler, “Effect of the interval between exposures to cytarabine on its cytotoxic action on HL-60 myeloid leukemic cells,” *Cancer Treatment Reports*, vol. 68, no. 9, pp. 1143–1148, 1984.
- [16] D. Y. Bouffard and R. L. Momparler, “Comparison of the induction of apoptosis in human leukemic cell lines by 2', 2'-difluorodeoxycytidine (gemcitabine) and cytosine arabinoside,” *Leukemia Research*, vol. 19, no. 11, pp. 849–856, 1995.
- [17] J. H. Choy, J. S. Jung, J. M. Oh et al., “Layered double hydroxide as an efficient drug reservoir for folate derivatives,” *Biomaterials*, vol. 25, no. 15, pp. 3059–3064, 2004.
- [18] J. M. T. Hamilton-Miller and W. Brumfitt, “Methenamine and its salts as urinary tract antiseptics. Variables affecting the antibacterial activity of formaldehyde, mandelic acid, and hippuric acid in vitro,” *Investigative Urology*, vol. 14, no. 4, pp. 287–291, 1977.
- [19] D. Kaye, “Antibacterial activity of human urine,” *Journal of Clinical Investigation*, vol. 47, no. 10, pp. 2374–2390, 1968.
- [20] Y. L. Lee, J. Owens, L. Thrupp, and T. C. Cesario, “Does cranberry juice have antibacterial activity?” *Journal of the American Medical Association*, vol. 283, no. 13, p. 1691, 2000.
- [21] I. Ofek, J. Goldhar, D. Zafriri, H. Lis, R. Adar, and N. Sharon, “Anti-*Escherichia coli* adhesin activity of cranberry and blueberry juices,” *The New England Journal of Medicine*, vol. 324, no. 22, p. 1599, 1991.
- [22] R. Raz, B. Chazan, and M. Dan, “Cranberry juice and urinary tract infection,” *Clinical Infectious Diseases*, vol. 38, no. 10, pp. 1413–1419, 2004.
- [23] N. Mesaros, P. Nordmann, P. Plésiat et al., “*Pseudomonas aeruginosa*: resistance and therapeutic options at the turn of the new millennium,” *Clinical Microbiology and Infection*, vol. 13, no. 6, pp. 560–578, 2007.
- [24] A. R. Naylor, P. D. Hayes, and S. Darke, “A prospective audit of complex wound and graft infections in Great Britain and Ireland: the emergence of MRSA,” *European Journal of Vascular and Endovascular Surgery*, vol. 21, no. 4, pp. 289–294, 2001.
- [25] J. N. Sharpe, E. H. Shively, and H. C. Polk, “Clinical and economic outcomes of oral linezolid versus intravenous vancomycin in the treatment of MRSA-complicated, lower-extremity skin and soft-tissue infections caused by methicillin-resistant *Staphylococcus aureus*,” *American Journal of Surgery*, vol. 189, no. 4, pp. 425–428, 2005.
- [26] D. M. Livermore, “Multiple mechanisms of antimicrobial resistance in *Pseudomonas aeruginosa*: our worst nightmare?” *Clinical Infectious Diseases*, vol. 34, no. 5, pp. 634–640, 2002.
- [27] A. J. Huh and Y. J. Kwon, “‘Nanoantibiotics’: a new paradigm for treating infectious diseases using nanomaterials in the antibiotics resistant era,” *Journal of Controlled Release*, vol. 156, pp. 128–145, 2011.
- [28] S. Parveen, R. Misra, and S. K. Sahoo, “Nanoparticles: a boon to drug delivery, therapeutics, diagnostics and imaging,” *Nanomedicine*, vol. 8, no. 2, pp. 147–166, 2012.

Review Article

Nanomedicine in Action: An Overview of Cancer Nanomedicine on the Market and in Clinical Trials

Ruibing Wang, Paul S. Billone, and Wayne M. Mullett

Nordion Inc., 447 March Road, Ottawa, ON, Canada K2K 1X8

Correspondence should be addressed to Ruibing Wang; ruibing.wang@nordion.com

Received 22 October 2012; Accepted 9 November 2012

Academic Editor: Haiyan Li

Copyright © 2013 Ruibing Wang et al. This is an open access article distributed under the Creative Commons Attribution License, which permits unrestricted use, distribution, and reproduction in any medium, provided the original work is properly cited.

Nanomedicine, defined as the application of nanotechnology in the medical field, has the potential to significantly change the course of diagnostics and treatment of life-threatening diseases, such as cancer. In comparison with traditional cancer diagnostics and therapy, cancer nanomedicine provides sensitive cancer detection and/or enhances treatment efficacy with significantly minimized adverse effects associated with standard therapeutics. Cancer nanomedicine has been increasingly applied in areas including nanodrug delivery systems, nanopharmaceuticals, and nanoanalytical contrast reagents in laboratory and animal model research. In recent years, the successful introduction of several novel nanomedicine products into clinical trials and even onto the commercial market has shown successful outcomes of fundamental research into clinics. This paper is intended to examine several nanomedicines for cancer therapeutics and/or diagnostics-related applications, to analyze the trend of nanomedicine development, future opportunities, and challenges of this fast-growing area.

1. Introduction

According to National Nanotechnology Initiative (NNI, a multiagency US government program initiated in 2001), nanotechnology is broadly defined as the science and engineering involved in the design, synthesis, characterization, and application of materials and devices with at least one of the dimensions on the nanoscale (typically 1–100 nanometers) [1]. Since its inception several decades ago, nanotechnology has drawn increasing attention from both the academic and industrial sectors for applications not only in materials science and engineering, such as light-emitting devices and solar cells, but also in the biotechnology and medical fields including disease diagnostics, prevention, and treatment. Accordingly, the level of interest in nanotechnology shown by both academic and industrial investigators has led to the increased development of novel nanotechnology platforms for medical applications, sharp increases in government funding, and venture capital investment [2]. Nanomedicine as a newly created subterm, refers to the application of engineered nanomaterials to the medical field.

Nanotechnology offers many potential benefits to medical applications including the early detection of cancers

and cancer treatment, passive and active disease targeting, increased biocompatibility, and multifunctionality encompassing both imaging and therapeutic capabilities, allowing for simultaneous disease treatment and monitoring [3]. The major advantages of nanomaterials in medical applications include the following. (1) They are on the same size scale with biomolecules such as receptors, antibodies, and nucleic acids. Nanomaterials can also be functionalized with biomolecules, enabling them to target specific organelles within certain tissues or even the entire cells for localization in the targeted area. (2) Nanostructures can often overcome solubility and stability issues through surface modification/wrappings or additional formulation. (3) Nanostructures have novel physical properties, such as optical properties from quantum dots, which can be utilized for bioimaging. (4) Due to the nanosize, they are normally composed of thousands of atoms with a high surface area so that a higher therapeutic payload (e.g., radioactive isotopes or chemotherapy drugs) can be carried to or encapsulated in the nanostructure. Once delivered and recognized by a receptor, the high-dose therapeutic load can cause more devastating damage to cancer cells at the targeted site. (5) Nanoparticle (NP) formulations, through passive or active targeting, can often release therapeutic payloads at

TABLE 1: Nanomedicines approved by one or more regulatory bodies.

Product	Nanoplatfrom/agent	Indication	Status	Company
Doxil	PEGylated liposome/doxorubicin hydrochloride	Ovarian cancer	Approved 11/17/1995 FDA50718	Ortho Biotech (acquired by JNJ)
Myocet	Non-PEGylated liposomal doxorubicin nanomedicine	Metastatic breast cancer	Approved in Europe and Canada, in combination with cyclophosphamide	Sopherion Therapeutics, LLC in North America and Cephalon, Inc. in Europe
DaunoXome	Lipid encapsulation of daunorubicin	First-line treatment for patients with advanced HIV-associated Kaposi's sarcoma	Approved in the USA	Galen Ltd.
ThermoDox	Heat-activated liposomal encapsulation of doxorubicin	Breast cancer, primary liver cancer	Received Fast Track Designation, approval expected by 2013	Celsion
Abraxane	Nanoparticulate albumin/paclitaxel	Various cancers	Approved 1/7/2005 FDA21660	Celgene
Rexin-G	Targeting protein tagged phospholipid/microRNA-122	Sarcoma, osteosarcoma, pancreatic cancer, and other solid tumor	Fully approved in Philippine Phase II/III (Fast Track Designation, Orphan Drug Status Acquired) in USA	Epeius Biotechnologies Corp.
Oncaspar	PEGylated asparaginase	Acute lymphoblastic leukemia	Approved 24/06/2006	Enzon Pharmaceuticals, Inc.
Resovist	Iron oxide nanoparticles coated with carboxydextran	Liver/spleen lesion imaging	In 2001, approved for the European market	Bayer Schering Pharma AG
Feridex	Iron oxide nanoparticles coated with dextran	Liver/spleen lesion imaging	Approved by US-FDA in 1996	Berlex Laboratories
Endorem	Iron oxide nanoparticles coated with dextran	Liver/spleen lesion imaging	Approved in Europe	Guerbet

cancer sites, thus significantly reducing nonspecific toxicity [3].

However, challenges always exist together with opportunities. First, nanomedicine may pose a myriad of full characterization challenges. Second, concerns about safety and manufacturability should not be ignored. For instance, each nanomedicine's batch-to-batch consistency needs to be verified with effective quality control methods [4]. In addition, nanomedicine may be ineffective if the therapeutic moiety of a particle disassociates from the nanoparticle platform upon administration or during circulation in the bloodstream or is degraded inside the particle. Pretargeting release of a therapeutic payload (e.g., a chemotherapeutic) from the nanoplatfrom may result in an acute toxicity independent of the pharmacokinetics of the nanoparticle platform itself [3, 5]. Clinical translation of NPs requires a complete understanding of particle size, composition, formulation, internal and external structure, chemical reactivity and stability, and their relationship with the human body, namely, biodistribution, toxicity, and biocompatibility [6].

Even with these and other challenges, a few first-generation nanomedicines have already obtained recognition in the clinical cancer research community as effective tools. For instance, Doxil (a liposomal formulation of doxorubicin) was approved by the FDA in the mid-1990s and demonstrated a decreased cardiotoxicity compared with free doxorubicin

TABLE 2: Half-life of ASNase (native versus PEGylated) [50].

Product	Manufacturer	$T_{1/2}$
E. coli native ASNase (Elspar)	Merck & Co. Inc.	1.15 days
PEG-ASNase (Oncaspar)	Enzon Pharmaceuticals	5.85 days

[7]. Another prime example of the budding success of nanomedicine is Abraxane, a nanoscale albumin-bound form of paclitaxel, approved by FDA in 2005 [8]. This nanoparticle has a size around 100 nm and solubilizes a poorly soluble drug (paclitaxel) so that the notable side effects of paclitaxel are significantly decreased. Tables 1 and 3 list nanomedicine, constructs currently on the market and in clinical trials, respectively. It is noteworthy from the list that most of the FDA approved marketed nanomedicines, including Doxil, Abraxane, ThermoDox, and Rexin-G, are organic-based formulations, presumably due to better biocompatibility and the low (or no) toxicity of the organic platforms. However, inorganic materials-based medical devices and nanomedicines, such as Aurimune (colloidal gold platform based) and AuroLase (gold-coated silica nanoparticle platform based), have recently gained FDA recognition and are in various phases of clinical trials [9, 10]. The majority of the agents are therapeutics, where market sizes are larger and potentially more profitable than diagnostics, given equal or similar

TABLE 3: Nanoparticle cancer therapeutics undergoing clinical investigation.

Product/agent	Nanoplatform	Indication	Status	Company
Cycloset	Cyclodextrin nanoparticles (Cyclodextrin NP/SiRNA)	Solid tumors	Phase I	Insert Therapeutics (now Calando Pharmaceuticals)
CRLX101	Cyclodextrin NPs/Campothecin	Various cancers	Phase II	Cerulean Pharma
S-CKD602	PEGylated liposomal CKD602 (topoisomerase inhibitor)	Various cancers	Phase I/II	Alza Corporation
CPX-1	Liposomal irinotecan	Colorectal cancer	Phase II	Celator Pharmaceuticals
CPX-351	Liposomal cytarabine and daunorubicin	Acute myeloid leukemia	Phase I	Celator Pharmaceuticals
LE-SN38	Liposomal SN38	Colorectal cancer	Phase II	Neopharm
INGN-401	Liposomal/FUS1	Lung cancer	Phase I	Introgen
NC-6004	Polymetric nanoparticle (PEG-polyaspartate) formulation of cisplatin	Various cancers	Phase I	NanoCarrier Co.
NK-105	Polymetric nanoparticle (PEG-polyaspartate) formulation of paclitaxel	Various cancers	Phase II	Nippon Kayaku Co. Ltd.
NK-911	Polymetric nanoparticle (PEG-polyaspartate) formulation of doxorubicin	Various cancers	Phase I	Nippon Kayaku Co. Ltd.
NK-012	Polymetric micelle of SN-38	Various cancers	Phase II	Nippon Kayaku Co. Ltd.
SP1049C	Glycoprotein of doxorubicin	Various cancers	Phase II	Supratek Pharma Inc.
SP1-077	PEGylated liposomal cisplatin	Head/neck and lung cancer	Phase II	Alza Corporation
ALN-VSP	Lipid nanoparticle formulation of siRNA	Liver cancer	Phase I	Alnylam Pharmaceuticals
OSI-7904L	Liposomal thymidylate synthase inhibitor	Various cancers	Phase II	OSI Pharmaceuticals
OSI-211	Liposomal lurtotecan	Various cancers	Phase II	OSI Pharmaceuticals
Combix	Iron oxide	Tumor imaging	Phase III	Advanced Magnetics
Aurimmune	Colloidal gold/TNF	Solid tumors	Phase II	CytImmune Sciences
SGT-53	Liposome Tf antibody/p53 gene	Solid tumors	Phase I	SynerGene Therapeutics
BIND-014	PLGA/PLA NPs/Docetaxel	Prostate cancer and others	Phase I	BIND Biosciences
AuroLase	Gold-coated silica NPs	Head and neck cancer	Phase I	Nanospectra Biosciences
Rexin-G	Targeting protein tagged phospholipid/microRNA-122	Sarcoma, osteosarcoma, pancreatic cancer, and other solid tumor	Phase II/III (Fast Track Designation, Orphan Drug Status Acquired) in USA fully approved in Philippine	Epeius Biotechnologies Corp.

TABLE 3: Continued.

Product/agent	Nanoplatform	Indication	Status	Company
ThermoDox	Heat-activated liposomal encapsulation of doxorubicin	Breast cancer, primary liver cancer	Approved for Breast Cancer; Phase III for primary liver cancer	Celsion
BIND-014	Polymeric nanoparticle formulation of docetaxel	Various cancers	Phase I	BIND Bioscience
SGT53-01	Transferrin targeted liposome with p53 gene	Solid tumors	Phase I	SynerGene Therapeutics
PEG-PGA and DON	PEG-glutaminase combined with glutamine antimetabolite 6-diazo-5-oxo-l-norleucine (DON)	Various cancers	Phase I/II	EvaluatePharma
PEG-IFN α 2a	PEG-asys	Melanoma, chronic myeloid leukemia, and renal-cell carcinoma	Phase I/II	Genentech
PEG-IFN α 2b	PEG-Intron	Melanoma, multiple myeloid, and renal-cell carcinoma	Phase I/II	Merck
ADI-PEG20	PEG-arginine deiminase	Hepatocellular carcinoma	Phase I	Polaris

development costs associated with a regulatory approval for either type [6].

The following sections will discuss nanomedicines that are on the market (approved from one or more regulatory authorities for commercial use) and nanomedicines that are still in clinical trials, as listed in Tables 1 and 3, respectively.

2. Cancer Nanomedicine on the Market

2.1. Liposomal Anthracyclines. There are several nanoparticle technologies based on the liposomal encapsulation of anthracyclines, which are known to be potent cytotoxic agents for various types of cancers. Three of the most widely known and marketed technologies are Doxil (also marketed in Canada and Europe as Caelyx, Janssen Biotech, Inc.), Myocet (marketed by Sopherion Therapeutics, LLC in North America and Cephalon, Inc. in Europe), and DaunoXome (Galen Ltd.).

2.1.1. Doxil. Doxil was initially approved by the FDA in 1995 as a treatment for AIDS-related Kaposi's sarcoma. It is considered the first approved "nanodrug" and has been successful since its market introduction, with over \$600 million USD in annual sales across all of its markets [11].

Doxil liposomes consist of a single lipid bilayer membrane composed of hydrogenated soy phosphatidylcholine (HSPC) and cholesterol with doxorubicin encapsulated in the internal compartment [12]. The mean size of the vesicles is in the range of 80–90 nm [13] and because doxorubicin is a small-molecule therapeutic, each vesicle can hold a payload of up to 15,000 molecules [12]. In order to mitigate the stability and early release issues that traditional liposomal encapsulations of doxorubicin have [14], 2000 Da segments of poly(ethylene glycol) (PEG) are grafted to the liposome surface. In addition to providing stability to the particles, the PEG functionalization makes the particles nearly invisible to the reticuloendothelial system (RES), earning them the distinction of stealth liposomes [12, 13].

Doxil vesicles rely on a passive targeting mechanism in order to accumulate at tumor sites [13]. While not specific to the Doxil formulation (as evident from the other technologies discussed below), the primary mechanism for accumulation and distribution throughout tumor sites is believed to be due to the combination of long circulation time (half-life of 2-3 days for clearance) [12] and the microvasculature of tumors, along with the enhanced permeability and retention (EPR) effect [15, 16]. The volume of the distribution of Doxil is only slightly larger than the plasma volume itself, indicating that there is a very little uptake of the liposomes by healthy tissue. Consequently, many studies have indicated that Doxil efficacy is substantially higher than that of free doxorubicin on a mg-to-mg scale [13], likely due to the liposomal targeting mechanism discussed above. However there is still no consensus on the mechanism of doxorubicin delivery itself to the cancerous cells within the tumor once the vesicles have been uptaken. Barenholz discusses two mechanisms [11] but concludes that the most likely mechanism for doxorubicin delivery is that a collapse of the ammonium sulfate gradient in the tumor interstitial fluid results in the release of the

doxorubicin outside the tumor cells, after which it is taken up by the cells; this mechanism still lacks conclusive clinical evidence.

Despite its significantly longer circulation time than doxorubicin itself (which has an *in vivo* half-life of ~5 min) [12], Doxil has dramatically different, and less severe, side effects than the free drug [15]. In particular, Doxil shows a drastic decrease in the cardiotoxicity over doxorubicin, for which cardiotoxicity is the dose-limiting side effect. Early Phase I-II studies with Doxil revealed that the cardiotoxicity in solid tumor patients is insignificant [12], attributed to nearly negligible levels of the free drug in the blood stream and the minimal distribution of Doxil to the heart itself. The maximum tolerated dose (MTD) of Doxil, as defined during Phase II trials, was 50 mg/m² every four weeks [17]. The two most severe side effects of Doxil are mucositis and palmar plantar erythrodysesthesia (PPE) [12]. PPE, which is a schedule-limiting and critical dose-limiting factor for multiple-course treatment regimes [12], is a toxic effect unique to Doxil (not observed with free doxorubicin) and is attributed largely to the long circulation time of the vesicles and a tendency of stealth liposomes to accumulate at the skin [18].

As of 2012, indications for Doxil include second-line treatment of AIDS-related Kaposi's sarcoma (1995), recurrent ovarian cancer (1998), metastatic breast cancer (2003), and multiple myeloma in combination with bortezomib (2007) [11].

2.1.2. Myocet. Myocet is a liposomal doxorubicin nanomedicine whose main difference from Doxil is that it lacks the PEG functionalization on the particle surface. Advantages of the formulation are mainly to do with toxicity. Without PEGylation, the circulation time is significantly shorter than observed for Doxil (~2.5 hrs) and the liposomes are not "invisible" to the RES. Therefore, Myocet is not associated with PPE, the dose-limiting toxicity of Doxil, and shows significantly reduced incidence of mucositis when compared to Doxil [19]. However, Myocet still has a circulation time long enough to ensure the effective passive targeting of tumor sites. Despite the significantly increased circulation time of Myocet as compared to doxorubicin, efficacy is essentially the same in most clinical tests [20]. In one particular Phase III head-to-head comparison between doxorubicin and Myocet for the treatment of metastatic breast cancer, response rates and progression-free survival were identical for the two treatments [21]. However, the incidence of cardiac-related toxicity was lower with Myocet. The major dose limiting toxicity (DLT) of Myocet has been shown to be leukopenia or neutropenia [22].

The Myocet liposome is composed of a bilayer membrane of egg phosphatidylcholine and cholesterol in a 55 : 45 mole ratio. Doxorubicin is loaded into the internal aqueous core of the particle using an active loading process driven by a pH gradient; once the doxorubicin is loaded into the liposomes, the molecules stack into fibres that are noncovalently cross-linked with citrate [23]. Unlike Doxil, Myocet has been observed to release its doxorubicin quite rapidly. Within 24 hours, 90% of its doxorubicin content is released *in vivo* [19]. The increased release rate as compared to Doxil is attributed

primarily to the lack of PEG coating, which stabilizes the membrane of the liposome and prevents the leakage of the payload [16].

Myocet is not yet approved for use in the USA (Phase III clinical trials as first-line treatment for HER2 positive metastatic breast cancer is underway) but it is marketed in Canada and Europe in combination with cyclophosphamide as a first-line treatment for metastatic breast cancer [23].

2.1.3. DaunoXome. Unlike the previous two technologies, DaunoXome is a lipid encapsulation of a different anthracycline, daunorubicin. Daunorubicin differs from the more commonly used doxorubicin in that the former lacks a hydroxyl group at the 14-position [24]. DaunoXome was originally developed using daunorubicin instead of doxorubicin due to its increased aqueous stability and its increased cytotoxicity for certain types of solid tumors [19]. The DaunoXome liposome consists of a bilayer membrane of distearoyl phosphatidylcholine and cholesterol at a 2 : 1 molar ratio. The citrate salt of daunorubicin is encapsulated within the inner aqueous core of the vesicle [25]. The particles themselves are approximately 50 nm in diameter [26] and demonstrate the high stability and minimal leakage of the entrapped daunorubicin [27].

Like the previously discussed doxorubicin-based technologies, DaunoXome also relies on a passive-targeting mechanism for the targeting of tumor sites. Because of the small vesicle size, net neutral charge, and incorporation of cholesterol and a lipid molecule with a high phase-transition temperature, DaunoXome is able to avoid the RES and has a circulation half-life of 2–4 hours [28]. Early trials with DaunoXome versus free daunorubicin showed higher accumulation of free daunorubicin within tumors for the DaunoXome than for the free drug. The free drug showed 9.6 $\mu\text{g/g}$ accumulation in the tumor after 1 hr, with further decreasing levels thereafter, while DaunoXome treatment resulted in 100 $\mu\text{g/g}$ accumulation of daunorubicin equivalents through 11 hours [24].

DaunoXome is approved in the USA as a first-line treatment for patients with advanced HIV-associated Kaposi's sarcoma [29]. There are also many active and/or recruiting clinical trials trying to prove the clinical efficacy for various forms of leukemia [30].

2.2. ThermoDox. While not currently approved in any markets, Celsion's ThermoDox is very similar to Doxil and Myocet, as discussed above; in that it is composed of doxorubicin encapsulated within the aqueous inner core of bilayer liposomes. The property that makes ThermoDox unique and has garnered it so much attention is that upon heating the liposomes to temperatures $\geq 39.5^\circ\text{C}$, they release their payloads of doxorubicin within seconds [31, 32]. This property enables the payload of doxorubicin to be delivered as a burst to a tumor site without the associated systemic toxicity observed with the administration of the free drug itself [33].

The ThermoDox liposome is comprised of dipalmitoylphosphatidylcholine (DPPC), monostearoylphosphatidylcholine (MSPC), and DSPE-MPEG-2000 in a 90 : 10 : 4 molar ratio [31]. DPPC, which has a gel-to-liquid crystalline phase

transition temperature (T_c) of 41.5°C , induces membrane instability in the ThermoDox liposome at temperatures around T_c . Because of its size (~ 100 nm) and nature, the liposomes are rapidly identified by the RES and are concentrated in the liver [33]. Therefore, ThermoDox was identified as an ideal candidate for the treatment of hepatocellular carcinoma (HCC). In order to deliver the thermal energy required to release the ThermoDox payload of doxorubicin, radiofrequency ablation (RFA) is a convenient means as it is already widely used in the treatment of HCC. Two of the main drawbacks of RFA in the treatment of HCC tumors are the following. (1) Large tumors (>3 cm) are ineffectively treated and (2) cancerous cells at the periphery of the tumor often survive following RFA treatment and result in incidents of recurrence [33]. However, when ThermoDox was administered prior to RFA treatment in various preclinical and early-phase clinical trials, there were synergistic effects on treatment. The doxorubicin released by the ThermoDox upon RFA-induced heating increases the tumoricidal effect at the ablation margin, while RFA improves the efficacy of the doxorubicin at killing cancerous cells. The latter point has been observed through many studies and is attributed to the upregulation of doxorubicin induced at the high temperatures reached during RFA [33].

The MTD of ThermoDox was determined to be 50 mg/m^2 ; the dose-limiting toxicities were grade 3 alanine aminotransferase increase and grade 4 neutropenia. There does not seem to be any abnormal liver toxicity for the treatment based on the use of ThermoDox; all of the adverse events during early phase clinical trials were consistent with the adverse event profile of free doxorubicin.

There is currently one major Phase III clinical trial ongoing for ThermoDox in conjunction with RFA for the treatment of unresectable HCC [34]. According to the information on Celsion's website (<http://celsion.com/>), results of the pivotal HEAT clinical trial are expected sometime in 2013. The FDA has given the HEAT trial a Fast Track Designation and it is being conducted under an FDA Special Protocol Assessment. In addition, the National Institutes of Health (NIH) has designated the study as a Priority Trial for liver cancer. The US-FDA, European Medicines Agency (EMA), and the Chinese, South Korean, and Taiwanese regulatory bodies have all confirmed that the HEAT study provides an acceptable basis for the submission of a marketing authorization application [35]. ThermoDox treatment is also being investigated for various forms of breast cancer and bone metastases [36].

2.3. Abraxane. Unlike the previously discussed liposomal technologies, Abraxane (marketed by Celgene) is a nanoparticle-based cancer treatment that utilize albumin nanoparticles as the carriers of the active agent. The active agent in Abraxane is paclitaxel, a diterpene that has dramatic chemotherapeutic effects based on its ability to stabilize microtubules causing mitotic arrest [37]. While paclitaxel has been used widely as a chemotherapeutic agent for various forms of cancer, its original formulation (known as Taxol and also including ethanol) included the solvent Cremophor, which itself caused a number of adverse reactions, including

acute hypersensitivity [38]. Because of paclitaxel's hydrophobic nature, it needs a nonpolar carrier to make it clinically viable. Albumin is an ideal carrier as it is the natural carrier of hydrophobic molecules such as vitamins and hormones with favorable noncovalent binding interactions [39]. The nanoconjugates of albumin and paclitaxel are easily synthesized by mixing paclitaxel and human serum albumin in an aqueous solvent and passing the solution through a high pressure jet, resulting in nanoparticles in the size range of 100–200 nm [40]. Upon injection into biological systems, the nanoparticles rapidly dissolve into smaller 10 nm complexes consisting of albumin molecules with bound paclitaxel [38]. As expected, the Abraxane formulation lacks the toxicity effects attributed to the Cremophor solvent.

Abraxane has been shown to not only decrease the toxicity of traditional paclitaxel formulations but to actually increase the efficacy of the drug in clinical trials involving patients with an advanced breast cancer [38]. The increased efficacy has been proposed to be due to both increased uptake from the intravascular space and an increased transport into cancer cells. Albumin is known to bind to endothelial glycoprotein receptor gp60, which in turn is bound to an intracellular protein cavloin-1. This process causes the formation of transcytotic vesicles known as caveolae that transport the plasma constituents within the vesicle through the endothelial cell, including the albumin-bound paclitaxel [39]. Once the drug has been delivered from the intravascular space into the intratumoral space, albumin also facilitates the intratumoral uptake of paclitaxel. A recent *in vivo* study showed a 33% higher accumulation of paclitaxel in the intratumoral space for an albumin-conjugated form of paclitaxel when equal doses of paclitaxel were administered using the albumin-based and the Cremophor-formulated paclitaxel [41]. Current explanation for this phenomenon is that albumin is also able to bind to SPARC (secreted protein acid and rich in cysteine), a protein that is overexpressed in the extracellular space for a variety of cancers [39].

Abraxane (also commonly referred to as *nab*-paclitaxel) was approved by the FDA in 2005 for the treatment of breast cancer after the failure of the combination chemotherapy for metastatic disease or relapse within 6 months of adjuvant chemotherapy. Prior therapy should have included an anthracycline unless clinically contraindicated [42]. Several other indications are currently being pursued through aggressive clinical trials, including first-line metastatic breast cancer, nonsmall cell lung cancer, and recurrent ovarian, peritoneal, or fallopian tube cancers in platinum-sensitive patients.

2.4. Regin-G. The cancer collagen matrix targeting nanomedicine platform is a liposome platform with a high-affinity collagen-binding motif, derived from coagulation von Willebrand factor (vWF), which is genetically engineered into liposome surface proteins [43]. The model product of this platform, Regin-G, an Epeius proprietary product, is a replication-incompetent, pathotropic (disease-seeking) tumor matrix (collagen-) targeted retro vector encoding an N-terminal deletion mutant of the cyclin G1 gene with potential antineoplastic activity [43, 44]. The microRNA is

encapsulated into the said platform. When injected intravenously, the nanoparticles (~100 nm) seek out and accumulate in cancerous lesions wherein collagenous matrix proteins are exposed by tumor invasion, neoangiogenesis, and extracellular remodeling. The accumulation of nanoparticles within the tumor microenvironment, in the vicinity of cancer cells, enhances gene transfer efficiency via natural viral cell receptor mechanisms. In Epeius early preclinical and clinical studies, Regin-G demonstrated a significant antitumor activity in a broad spectrum of solid tumors [45, 46].

Although Epeius is currently conducting a number of clinical trials in the USA and abroad for Regin-G as therapeutic intervention for metastatic or locally advanced cancers, Regin-G in fact has been approved for use in “all solid tumors” in the Philippines based on profound evidence of single-agent efficacy in a broad spectrum of chemoresistant tumors [43]. The clinical data including the documentation of safety and efficacy of Regin-G from studies conducted in the Philippines has helped Regin-G to gain Orphan Drug Designation as an effective treatment for pancreatic cancer in 2003, followed by Orphan Drug Status for both osteosarcoma and soft tissue sarcoma in 2008 [44]. By 2009, Epeius completed its Advanced Phase I/II and confirmatory Phase II trials for pancreatic cancer, sarcoma, and osteosarcoma, respectively, with all primary and secondary endpoints achieved. Consequently, Regin-G has received FAST Track Status and priorities from the US-FDA and is in the process of applying for an accelerated approval for these clinical indications. The market in the USA may grow sharply if Phase III clinical trials go well [44].

It is worthwhile to point out that the Regin-G technology is the first of its kind (gene therapy of cancer) accessible on the market (e.g., in the Philippines) and has been considered revolutionary in the field of cancer treatment [47].

2.5. Oncaspar. Asparaginase (ASNase), a naturally occurring enzyme expressed and produced by microorganisms, catalyzes the hydrolysis of asparagine to aspartic acid. ASNase was identified as a potential chemotherapeutic agent for acute lymphoblastic leukemia (ALL) in 1961 when it was observed that guinea pig serum-treated lymphoma-bearing mice underwent a rapid and often complete regression [48]. The potential of ASNase as a childhood ALL therapeutic was confirmed with the consecutive series of clinical trials [49].

The working mechanism behind ASNase therapeutic effect on ALL is that ASNase catalyzes the conversion of L-asparagine to aspartic acid and ammonia (as shown by the equation below) whereas leukemic cells growth depends on circulating asparagine, since that ALL leukemic cells and some other suspected tumor cells are unable to synthesize the nonessential amino acid asparagine, whereas normal cells are able to make their own asparagine [50]. The presence of ASNase deprives the leukemic cell of circulating asparagine, which leads to cell death:



In the USA there are two forms of commercially available asparaginase: Elspar, an *E. coli*-derived asparaginase manufactured by Merck (Whitehouse Station, NJ, USA), and pegaspargase (Oncaspar), a PEGylated form of asparaginase, manufactured by Enzon Pharmaceuticals, Inc. (Bridgewater, NJ, USA) from the Merck asparaginase bulk drug product [50]. The technology of polyethylene glycol covalent conjugation to the native asparaginase increases the drug hydrodynamic radius, prolongs its circulation and retention time, decreases proteolysis, decreases renal excretion, and shields antigenic determinants from immune detection without obstructing the substrate-interaction site, and thus reduces the side effect of the native asparaginase such as hypersensitivity [51, 52].

Oncaspar was first approved by the US-FDA in 1994 for use in ALL patients who developed hypersensitivity to the native form of asparaginase. It was then approved by the US-FDA in 2006 as the first-line treatment of patients with ALL as a component of a multiagent chemotherapy regimen [53]. In addition to circumventing hypersensitivity to Elspar, PEGylation results in Oncaspar having a longer biological half-life than Elspar, as shown by Table 2. In most treatment protocols for ALL, Elspar is given three times weekly for six or nine doses. Because of the longer half-life of Oncaspar, it is often possible to achieve a similar or equal therapeutic effect with fewer injections [53].

This nanomedicine demonstrates again that drug surface modification (i.e., PEGylation) can significantly alter drug's pharmacokinetics and pharmacodynamics, thus eliminating some side effects (such as hypersensitivity) and/or enhancing treatment effect with a reduced dose.

2.6. Cancer Imaging Nanomedicine: Resovist and Feridex/Endorem. One of the very few fully approved inorganic-based cancer nanomedicines are superparamagnetic iron oxide (SPIO) nanoparticle agents for MR imaging. SPIO nanoparticle MR imaging contrast agents have been of great interest in research and clinical applications for the past decades [54]. While there are still some in clinical trials or experimental study stages, a few SPIO products have been approved by various regulatory bodies including the US-FDA [55]. Of these approved SPIOs, the most phenomenal products for cancer diagnostics are Resovist, Endorem, and Feridex [55].

Resovist, ferumoxide SPIO nanoparticles with 4.2 nm core diameters and 62 nm hydrodynamic diameters, is an organ-specific MRI contrast agent used for the detection and characterization of especially small focal liver lesions [56]. Resovist consists of SPIO nanoparticles coated with carboxydextran, which are accumulated by phagocytosis in cells of the reticuloendothelial system (RES) of the liver. The uptake of Resovist injection in the reticuloendothelial cells results in a decrease of the signal intensity of normal liver parenchyma on both *T2*- and *T1*-weighted images. Most malignant liver tumors do not contain RES cells and therefore do not uptake the iron particles. The resulting imaging effect is an improved contrast between the tumor (bright) and the surrounding tissue (dark). Resovist can be injected as an intravenous bolus, which allows for the immediate imaging of the liver and reduces the overall examination time.

A dynamic imaging strategy after bolus injection supports characterizing lesions. In comprehensive clinical trials, it demonstrated an excellent safety profile [57, 58]. In 2001, Resovist was approved for the European market. However, Resovist competed with Primovist, the other liver imaging agent of Bayer Schering Pharma AG. Due to this reason, the production of Resovist was unfortunately abandoned in 2009.

Endorem, marketed by Guerbet, and Feridex (approved by US-FDA in 1996), marketed by Berlex Laboratories, are also ferumoxide SPIO nanoparticles but coated with dextran instead of carboxydextran. The iron oxide core is 4.8–5.6 nm and the hydrodynamic diameter is about 80–150 nm. These nanoparticles efficiently accumulate in the liver (about 80% of injected dose) and spleen (about 5–10% of injected dose) within only minutes of administration, due to RES uptake [59]. But tumor tissues such as metastases, primary liver cancer, cysts and various benign tumors, adenomas, and hyperplasia do not take these materials and thus retain their native signal intensity, so the contrast between normal and abnormal tissue is increased. Peak concentrations of iron were found in liver after 2 hours and in the spleen after 4 hours and the blood half-life is only about 6 min [59]. Unlike Resovist, Endorem and Feridex show some side effects such as cardiovascular problems and lumbar pain [60].

Further development of SPIO-enhanced MR imaging depends on the improved knowledge of the fundamental mechanism of SPIO agents on MR signal, the pharmacokinetic control of these agents, including appropriate selection of particle charge, size, and coating, linking these agents with molecules capable of accurate specific targeting, and the development of new imaging sequences [60].

3. Cancer Nanomedicine in Clinical Trials

This section is focused on the cancer nanomedicines that are in clinical trials for any cancer indications and have not been approved by FDA or other regulatory bodies for commercial production.

3.1. Therapeutic Nanomedicine in Clinical Trials. Even with development challenges, a few first-generation nanoparticle therapeutics, such as Doxil and Abraxane, have already obtained recognition in the clinical cancer research community. Considerable research and clinical trials are now being invested in qualifying nanoparticles as “platforms” for various drugs. Table 3 provides an updated summary of the nanomedicine constructs currently undergoing clinical trials as previously published by Zhang et al. [61] and Tiwari et al. [62].

A large number of preclinical nanoparticle delivery systems have been developed with potential for cancer detection and therapy. The European Science and Technology Observatory (ESTO) conducted a global survey in 2006 and identified that over 150 companies are developing nanoscale therapeutics [63]. As indicated by this blossoming research area, the synthesis and formulation possibilities for nanoparticles are almost endless considering the ability to incorporate various chemical and biology entities that provide both imaging and therapeutic capabilities. However, this multimodality

approach combined with the ability to control and target the delivery of a therapeutic agent requires a sophisticated engineering of nanoparticles. For example, multiple factors affect the pharmacokinetic behavior of nanoparticles, but the surface charge, size, nanoparticle shape, and stealth properties are among the most critical. Researchers have exploited these properties at the benchtop for introduction into various preclinical models for the optimization of the stability and delivery characteristics of the nanoparticle. More significantly, this research work has now also led into the introduction of nanoparticle candidates into the clinical and commercial market.

In particular, therapeutically loaded nanomedicines have the potential for achieving improved therapeutic indexes for cancer treatment. Nanoparticles have shown a significant promise as improved drug delivery systems improving the formulation characteristics of the existing drugs that may have poor administration. Several commercial examples now exist, confirming the promise of nanoparticle reformulation approaches to reduce drug side effects, while potentially increasing efficacy. One additional promise of nanoparticles is the reformulation of therapeutic agents that have failed in clinical development due to pharmacology challenges. For example, Shim et al. [64] recently described a proof of a principle nanoparticle approach to overcome drug delivery challenges and revive the clinical potential of wortmannin.

A series of clinical studies have substantiated the potential of nanoparticle-based therapeutics for demonstrating the enhanced tumor accumulation of delivered therapeutics with less adverse effects. Although most commercialized nanomedicines have been based on a passive-targeting strategy that exploits the EPR effect, there is an increasing need for the development of active-targeting technologies. The leading strategy has been the conjugation of ligand molecules that specifically bind to receptors that are overexpressed on tumor cells relative to normal cells [62].

As indicated during previous discussions and by a recent review [65], six common types of nanoparticles are approved or in late stages of clinical trials: polymer-drug conjugates, micelles, protein-based carriers, liposomes, polymeric nanoparticles, and inorganic nanoparticles. As previously discussed and seen from Table 3 a majority of nanoparticles under clinical/commercial development are therapeutics, and most of them are organic based due to a relatively low toxicity and high biocompatibility.

To further extend the capabilities of nanoparticles for simultaneous imaging and therapeutic applications, researchers have begun to increasingly exploit various inorganic matrices, such as gold, iron oxide, quantum dots, and silica nanoparticles [66]. In this respect, nanomedicines can be developed as theranostics, which possess both imaging and therapy capabilities.

3.2. Theranostics in Clinical Trials. Cancer nanotheranostics are the use of nanoparticles for combined diagnosis and therapy in cancer applications. Incorporating imaging capability into a nanoparticle is a very useful attribute for monitoring the distribution of the treatment *in vivo*. This provides direct and confirmatory information about the mechanism

of action for a specific patient, thereby providing a significant advantage over more traditional drug therapies for cancer treatment. The development of multifunctional nanoparticles has the potential for the rapid disease verification and identification of the effected tissues for improved treatment protocols. Wang et al. [66] indicated in a recent review article that a combined technique will result in an acceleration of the drug development and improved disease management with reduced risks and costs.

The clinical development of theranostic agents is still preliminary and several challenges, such as efficient and targeted guidance of the therapeutic/imaging nanoparticles, still exist [67]. In addition, the potency of the nanoparticle could be further improved with multimodality treatment options. However, one nanoparticle platform which is progressing from the benchtop to the clinical bedside is gold nanoparticles. Their inherit properties make them appealing as the material can be easily manufactured and functionalized with both imaging/therapeutic agents and targeting vectors [68]. Initial clinical studies have been completed with gold nanoparticles coated with citrate and thiolated PEG/tumor necrosis factor- α (TNF- α) [69, 70]. The dose limiting toxicity of TNF- α was significantly improved with the developed gold nanoparticle formulation.

4. Summary and Perspectives

The biggest challenge that nanomedicine faces at present is meeting all the safety guidelines required for gaining clinical acceptance, particularly those required by the FDA and other regulatory bodies. Over the past decade, various nanoparticle/nanomedicine platforms have been screened and studied in terms of their size, shape, and surface properties to meet these guidelines and market request. These include (1) "target-specificity": ideally, a nanomedicine will accumulate mainly in the diseased organs/sites, bypassing normal ones, (2) a proper size (often ultrasmall): thus they can be eliminated from the body preferably through the renal filtration system, and (3) nontoxic and biocompatible, with a surface made up of natural polymers/biomolecules. Versatility of a nanomedicine is also highly desirable, which means that multifunctional therapeutic agents and multimodality imaging capacity (i.e., optical, MRI, SPECT, PET, and/or CT) can be combined into one nanomedicine that not only will facilitate the early diagnosis of diseases, but will also have the potential to monitor in real time the progress of the therapeutic delivery.

In spite of all the challenges, nanotechnology has become closely related with cancer care today and has been applied in an evolutionary manner to improve the properties of cancer therapeutic, diagnostics, and other health care products. Biotech, pharmaceutical, and medical sciences companies have been active parts of the evolution and are dynamic collaborators with researchers, government, and educational institutions in developing and translating cancer nanomedicines. Based on the full spectrum of cancer nanomedicines in clinical trials and on the market that have been discussed in this paper, it is highly expected that the forthcoming generations of nanomedicines will

have targeting moiety, may carry multiple drugs that could potentially be released in a controlled manner, and will be equipped with an imaging capacity.

Conflict of Interests

The authors claim no financial interests with any of the companies that are mentioned in the paper.

References

- [1] National Science and Technology Council Committee on Technology, *The National Nanotechnology Initiative: Research and Development Leading to a Revolution in Technology and Industry*, Office of Sciences and Technology Policy, Washington, DC, USA, 2005.
- [2] "Drug delivery," in *The Handbook of Experimental Pharmacology*, M. Schafer-Korting, Ed., pp. 55–86, Springer, Berlin, Germany, 2010.
- [3] S. E. McNeil, "Nanoparticle therapeutics: a personal perspective," *Wiley Interdisciplinary Reviews*, vol. 1, no. 3, pp. 264–271, 2009.
- [4] S. McNeil, "Nanoparticle therapeutics: a personal perspective," in *Proceedings of the MRS Functionalized Nanobiomaterials for Medical Applications Workshop*, Denver, Colo, USA, 2010.
- [5] W. E. Bawarski, E. Chidlow, D. J. Bharali, and S. A. Mousa, "Emerging nanopharmaceuticals," *Nanomedicine*, vol. 4, no. 4, pp. 273–282, 2008.
- [6] H. S. Choi and J. V. Frangioni, "Nanoparticles for biomedical imaging: fundamentals of clinical translation," *Molecular Imaging*, vol. 9, no. 6, pp. 291–310, 2010.
- [7] M. L. Immordino, F. Dosio, and L. Cattel, "Stealth liposomes: review of the basic science, rationale, and clinical applications, existing and potential," *International Journal of Nanomedicine*, vol. 1, no. 3, pp. 297–315, 2006.
- [8] M. R. Green, G. M. Manikhas, S. Orlov et al., "Abraxane, a novel Cremophor-free, albumin-bound particle form of paclitaxel for the treatment of advanced non-small-cell lung cancer," *Annals of Oncology*, vol. 17, no. 8, pp. 1263–1268, 2006.
- [9] E. H. Chang, "Nanomedicines: improving current cancer therapies and diagnosis," *Nanomedicine*, vol. 3, no. 4, p. 339, 2007.
- [10] J. M. Stern, J. Stanfield, W. Kabbani, J. T. Hsieh, and J. A. Cadeddu, "Selective prostate cancer thermal ablation with laser activated gold nanoshells," *Journal of Urology*, vol. 179, no. 2, pp. 748–753, 2008.
- [11] Y. Barenholz, "Doxil—the first fda-approved nano-drug: lessons learned," *Journal of Control Release*, vol. 160, no. 2, pp. 117–134, 2012.
- [12] A. A. Gabizon, "Pegylated liposomal doxorubicin: metamorphosis of an old drug into a new form of chemotherapy," *Cancer Investigation*, vol. 19, no. 4, pp. 424–436, 2001.
- [13] A. Gabizon, H. Shmeeda, and Y. Barenholz, "Pharmacokinetics of pegylated liposomal doxorubicin: review of animal and human studies," *Clinical Pharmacokinetics*, vol. 42, no. 5, pp. 419–436, 2003.
- [14] B. Čeh, M. Winterhalter, P. M. Frederik, J. J. Vallner, and D. D. Lasic, "Stealth liposomes: from theory to product," *Advanced Drug Delivery Reviews*, vol. 24, no. 2-3, pp. 165–177, 1997.
- [15] A. Gabizon, R. Catane, B. Uziely et al., "Prolonged circulation time and enhanced accumulation in malignant exudates of doxorubicin encapsulated in polyethylene-glycol coated liposomes," *Cancer Research*, vol. 54, no. 4, pp. 987–992, 1994.
- [16] Y. Malam, M. Loizidou, and A. M. Seifalian, "Liposomes and nanoparticles: nanosized vehicles for drug delivery in cancer," *Trends in Pharmacological Sciences*, vol. 30, no. 11, pp. 592–599, 2009.
- [17] F. M. Muggia, J. D. Hainsworth, S. Jeffers et al., "Phase II study of liposomal doxorubicin in refractory ovarian cancer: antitumor activity and toxicity modification by liposomal encapsulation," *Journal of Clinical Oncology*, vol. 15, no. 3, pp. 987–993, 1997.
- [18] A. Gabizon, D. Goren, A. T. Horowitz, D. Tzemach, A. Lossos, and T. Siegal, "Long-circulating liposomes for drug delivery in cancer therapy: a review of biodistribution studies in tumor-bearing animals," *Advanced Drug Delivery Reviews*, vol. 24, no. 2-3, pp. 337–344, 1997.
- [19] D. N. Waterhouse, P. G. Tardi, L. D. Mayer, and M. B. Bally, "A comparison of liposomal formulations of doxorubicin with Drug Administered in free form: changing toxicity profiles," *Drug Safety*, vol. 24, no. 12, pp. 903–920, 2001.
- [20] T. Lammers, W. E. Hennink, and G. Storm, "Tumour-targeted nanomedicines: principles and practice," *British Journal of Cancer*, vol. 99, no. 3, pp. 392–397, 2008.
- [21] L. Harris, G. Batist, R. Belt et al., "Liposome-encapsulated doxorubicin compared with conventional doxorubicin in a randomized multicenter trial as first-line therapy of metastatic breast carcinoma," *Cancer*, vol. 94, no. 1, pp. 25–36, 2002.
- [22] D. S. Alberts, F. M. Muggia, J. Carmichael et al., "Efficacy and safety of liposomal anthracyclines in Phase I/II clinical trials," *Seminars in Oncology*, vol. 31, no. 13, pp. 53–90, 2004.
- [23] Sopherion Therapeutics, "Myocet: doxorubicin hydrochloride (Liposome) for injection," 2001, <http://www.sopherion.com/pdf/PIEnglishv0-2.pdf>.
- [24] E. A. Forssen, "The design and development of DaunoXome for solid tumor targeting in vivo," *Advanced Drug Delivery Reviews*, vol. 24, no. 2-3, pp. 133–150, 1997.
- [25] A. Fassas and A. Anagnostopoulos, "The use of liposomal daunorubicin (DaunoXome) in acute myeloid leukemia," *Leukemia and Lymphoma*, vol. 46, no. 6, pp. 795–802, 2005.
- [26] J. A. Sparano and E. P. Winer, "Liposomal anthracyclines for breast cancer," *Seminars in Oncology*, vol. 28, no. 4, pp. 32–40, 2001.
- [27] E. A. Forssen and M. E. Ross, "DaunoXome treatment of solid tumors preclinical and clinical investigations," *Journal of Liposome Research*, vol. 4, no. 1, pp. 481–512, 1994.
- [28] T. M. Allen and F. J. Martin, "Advantages of liposomal delivery systems for anthracyclines," *Seminars in Oncology*, vol. 31, supplement 13, pp. 5–15, 2004.
- [29] Galen US, "DaunoXome: daunorubicin citrate liposome injection," 2011, <http://daunoxome.com/downloads/DaunoXome%20PI.pdf>.
- [30] Clinicaltrials.gov, U.S. National Institutes of Health, Search for "DaunoXome" AND "Phase 3", <http://clinicaltrials.gov/>.
- [31] H. I. Chang, M. Y. Cheng, and M. K. Yeh, "Clinically-proven liposome-based drug delivery: formulation, characterization and therapeutic efficacy," vol. 1, Article ID 195, 2012.
- [32] S. Dromi, V. Frenkel, A. Luk et al., "Pulsed-high intensity focused ultrasound and low temperature—sensitive liposomes for enhanced targeted drug delivery and antitumor effect," *Clinical Cancer Research*, vol. 13, no. 9, pp. 2722–2727, 2007.
- [33] R. T. P. Poon and N. Borys, "Lyso-thermosensitive liposomal doxorubicin: a novel approach to enhance efficacy of thermal

- ablation of liver cancer," *Expert Opinion on Pharmacotherapy*, vol. 10, no. 2, pp. 333–343, 2009.
- [34] Clinicaltrials.gov, U.S. National Institutes of Health, Search for "ThermoDo" AND "Phase 3", <http://clinicaltrials.gov/>.
- [35] "Celsion Progresses with ThermoDox," 2012, <http://finance.yahoo.com/news/celsion-progresses-thermodox-211903842.html>.
- [36] "Clinicaltrials.gov," U.S. National Institutes of Health, Search for "ThermoDox", <http://clinicaltrials.gov/>.
- [37] P. B. Schiff and S. B. Horwitz, "Taxol stabilizes microtubules in mouse fibroblast cells," *Proceedings of the National Academy of Sciences of the United States of America*, vol. 77, no. 3, pp. 1561–1565, 1980.
- [38] V. Guarneri, M. V. Dieci, and P. Conte, "Enhancing intracellular taxane delivery: current role and perspectives of nanoparticle albumin-bound paclitaxel in the treatment of advanced breast cancer," *Expert Opinion in Pharmacotherapy*, vol. 13, no. 3, pp. 395–406, 2012.
- [39] M. J. Hawkins, P. Soon-Shiong, and N. Desai, "Protein nanoparticles as drug carriers in clinical medicine," *Advanced Drug Delivery Reviews*, vol. 60, no. 8, pp. 876–885, 2008.
- [40] F. Kratz, "Albumin as a drug carrier: design of prodrugs, drug conjugates and nanoparticles," *Journal of Controlled Release*, vol. 132, no. 3, pp. 171–183, 2008.
- [41] N. Desai, V. Trieu, Z. Yao et al., "Increased antitumor activity, intratumor paclitaxel concentrations, and endothelial cell transport of cremophor-free, albumin-bound paclitaxel, ABI-007, compared with cremophor-based paclitaxel," *Clinical Cancer Research*, vol. 12, no. 4, pp. 1317–1324, 2006.
- [42] Abraxis BioScience LLC, "ABRAXANE Healthcare Professional Prescribing Information," http://www.abraxane.com/hcp/download/Abraxane_Prescribing_Information.pdf.
- [43] Epeius Biotech, <http://www.epeiusbiotech.com/oncology-RexinG-factsheet.asp>.
- [44] E. M. Gordon and F. L. Hall, "Rexin-G, a targeted genetic medicine for cancer," *Expert Opinion on Biological Therapy*, vol. 10, no. 5, pp. 819–832, 2010.
- [45] S. P. Chawla, V. S. Chua, L. Fernandez et al., "Phase I/II and phase II studies of targeted gene delivery in vivo: intravenous Rexin-G for chemotherapy-resistant sarcoma and osteosarcoma," *Molecular Therapy*, vol. 17, no. 9, pp. 1651–1657, 2009.
- [46] S. P. Chawla, V. S. Chua, L. Fernandez et al., "Advanced phase I/II studies of targeted gene delivery in vivo: intravenous rexin-G for gemcitabine-resistant metastatic pancreatic cancer," *Molecular Therapy*, vol. 18, no. 2, pp. 435–441, 2010.
- [47] E. Galanis, S. K. Carlson, N. R. Foster et al., "Phase I trial of a pathotropic retroviral vector expressing a cytotoxic cyclin G1 construct (Rexin-G) in patients with advanced pancreatic cancer," *Molecular Therapy*, vol. 16, no. 5, pp. 979–984, 2008.
- [48] J. D. Broome, "Evidence that the L-asparaginase activity of guinea pig serum is responsible for its antilymphoma effects," *Nature*, vol. 191, no. 4793, pp. 1114–1115, 1961.
- [49] L. Tallal, C. Tan, H. Oettgen et al., "E. coli L-asparaginase in the treatment of leukemia and solid tumors in 131 childrens," *Cancer*, vol. 25, no. 2, pp. 306–320, 1970.
- [50] V. I. Avramis and P. N. Tiwari, "Asparaginase (native ASNase or pegylated ASNase) in the treatment of acute lymphoblastic leukemia," *International journal of nanomedicine*, vol. 1, no. 3, pp. 241–254, 2006.
- [51] P. S. Gaynon, "Childhood acute lymphoblastic leukaemia and relapse," *British Journal of Hematology*, vol. 131, no. 5, pp. 579–587, 2005.
- [52] M. Jarrar, P. S. Gaynon, A. P. Periclou et al., "Asparagine depletion after pegylated E. coli asparaginase treatment and induction outcome in children with acute lymphoblastic leukemia in first bone marrow relapse: a Children's Oncology Group Study (CCG-1941)," *Pediatric Blood and Cancer*, vol. 47, no. 2, pp. 141–146, 2006.
- [53] H. J. Lenz, "Management and preparedness for infusion and hypersensitivity reactions," *Oncologist*, vol. 12, no. 5, pp. 601–609, 2007.
- [54] P. Reimer and B. Tombach, "Hepatic MRI with SPIO: detection and characterization of focal liver lesions," *European Radiology*, vol. 8, no. 7, pp. 1198–1204, 1998.
- [55] Y. X. J. Wang, S. M. Hussain, and G. P. Krestin, "Superparamagnetic iron oxide contrast agents: physicochemical characteristics and applications in MR imaging," *European Radiology*, vol. 11, no. 11, pp. 2319–2331, 2001.
- [56] P. Reimer and T. Balzer, "Ferucarbotran (Resovist): a new clinically approved RES-specific contrast agent for contrast-enhanced MRI of the liver: properties, clinical development, and applications," *European Radiology*, vol. 13, no. 6, pp. 1266–1276, 2003.
- [57] B. Hamm, T. Staks, M. Taupitz et al., "Contrast-enhanced MR imaging of liver and spleen: first experience in humans with a new superparamagnetic iron oxide," *Journal of Magnetic Resonance Imaging*, vol. 4, no. 5, pp. 659–668, 1994.
- [58] B. Hamm, T. Staks, and M. Taupitz, "A new superparamagnetic iron oxide contrast agent for magnetic resonance imaging," *Investigative Radiology*, vol. 29, no. 2, pp. S87–S89, 1994.
- [59] R. Weissleder, D. D. Stark, B. L. Engelstad et al., "Superparamagnetic iron oxide: pharmacokinetics and toxicity," *American Journal of Roentgenology*, vol. 152, no. 1, pp. 167–173, 1989.
- [60] Y. X. Wang, "Superparamagnetic iron oxide based MRI contrast agents: current status of clinical application," *Quantitative Imaging in Medicine and Surgery*, vol. 1, no. 1, pp. 35–40, 2011.
- [61] L. Zhang, F. X. Gu, J. M. Chan, A. Z. Wang, R. S. Langer, and O. C. Farokhzad, "Nanoparticles in medicine: therapeutic applications and developments," *Clinical Pharmacology and Therapeutics*, vol. 83, no. 5, pp. 761–769, 2008.
- [62] M. Tiwari, "Nano cancer therapy strategies," *Journal of Cancer Research and Therapeutics*, vol. 8, no. 1, pp. 19–22, 2012.
- [63] S. Karve, M. E. Werner, R. Sukumar et al., "Revival of the abandoned therapeutic wortmannin by nanoparticle drug delivery," *Proceedings of the National Academy of Sciences of the United States of America*, vol. 109, no. 21, pp. 8230–8235, 2012.
- [64] G. Shim, S. Lee, H. Choi et al., "Nanomedicines for receptor-mediated tumor targeting," *Recent Patents on Nanomedicine*, vol. 1, no. 2, pp. 138–148, 2012.
- [65] A. Naveed, H. Fessi, and A. Elaissari, "Theranostic applications of nanoparticles in cancer," *Drug Discovery Today*, vol. 17, no. 17–18, pp. 928–934, 2012.
- [66] A. Z. Wang, R. Langer, and O. C. Farokhzad, "Nanoparticle delivery of cancer drugs," *Annual Review of Medicine*, vol. 63, pp. 185–198, 2012.
- [67] M. P. Melancn, R. J. Stafford, and C. Li, "Challenges to effective cancer nanotheranostics," *Journal of Controlled Release*, vol. 164, pp. 177–182, 2012.
- [68] N. Trivedi, N. Patel, U. M. Upadhyay, and S. Sha, "Gold nanoparticulate drug delivery system: a review," *Pharmacie Globale International Journal of Comprehensive Pharmacy*, vol. 3, no. 6, pp. 1–5, 2012.

- [69] S. K. Libutti, G. F. Paciotti, L. Myer, R. Haynes, W. Gannon, and M. Walker, "Results of a completed phase I clinical trial of CYT-6091: a peglated colloidal gold-TNF," *Nanomedicine*, vol. 27, no. 15, p. 3586, 2009.
- [70] S. K. Libutti, G. F. Paciotti, A. A. Byrnes et al., "Phase I and pharmacokinetic studies of CYT-6091, a novel PEGylated colloidal gold-rhTNF nanomedicine," *Clinical Cancer Research*, vol. 16, no. 24, pp. 6139–6149, 2010.

Research Article

Nanostructured Surfaces to Target and Kill Circulating Tumor Cells While Repelling Leukocytes

Michael J. Mitchell, Carlos A. Castellanos, and Michael R. King

Department of Biomedical Engineering, Cornell University, Ithaca, NY 14853, USA

Correspondence should be addressed to Michael R. King, mike.king@cornell.edu

Received 19 November 2012; Accepted 5 December 2012

Academic Editor: Haiyan Li

Copyright © 2012 Michael J. Mitchell et al. This is an open access article distributed under the Creative Commons Attribution License, which permits unrestricted use, distribution, and reproduction in any medium, provided the original work is properly cited.

Hematogenous metastasis, the process of cancer cell migration from a primary to distal location via the bloodstream, typically leads to a poor patient prognosis. Selectin proteins hold promise in delivering drug-containing nanocarriers to circulating tumor cells (CTCs) in the bloodstream, due to their rapid, force-dependent binding kinetics. However, it is challenging to deliver such nanocarriers while avoiding toxic effects on healthy blood cells, as many possess ligands that adhesively interact with selectins. Herein, we describe a nanostructured surface to capture flowing cancer cells, while preventing human neutrophil adhesion. Microtube surfaces with immobilized halloysite nanotubes (HNTs) and E-selectin functionalized liposomal doxorubicin (ES-PEG L-DXR) significantly increased the number of breast adenocarcinoma MCF7 cells captured from flow, yet also significantly reduced the number of captured neutrophils. Neutrophils firmly adhered and projected pseudopods on surfaces coated only with liposomes, while neutrophils adherent to HNT-liposome surfaces maintained a round morphology. Perfusion of both MCF7 cells and neutrophils resulted in primarily cancer cell adhesion to the HNT-liposome surface, and induced significant cancer cell death. This work demonstrates that nanostructured surfaces consisting of HNTs and ES-PEG L-DXR can increase CTC recruitment for chemotherapeutic delivery, while also preventing healthy cell adhesion and uptake of therapeutic intended for CTCs.

1. Introduction

Hematogenous metastasis typically signals a poor patient prognosis, with over 90% of cancer deaths attributed to the metastatic spread [1]. For metastasis to occur, cancer cells detach from the primary tumor, invade through the basement membrane, and intravasate into the peripheral circulation as circulating tumor cells (CTCs) [2]. CTCs that express sialylated carbohydrate ligands on their surface can adhesively interact with selectin proteins on the inflamed endothelial cell wall, leading to selectin-mediated CTC tethering and rolling on the endothelium, followed by firm adhesion and arrest [3]. CTCs can then extravasate to the tissue of a distal organ to form secondary metastases, and while the percentage of CTCs that survive this pathway is small (<0.01%), the formation of such metastases remains the primary cause of cancer-related deaths [4, 5].

Several chemotherapeutics are currently in use for the treatment of cancers, including doxorubicin, which is in use for the treatment of Kaposi's sarcoma, acute leukemia,

metastatic breast cancer, and other lymphomas and sarcomas [6]. Doxorubicin is an adriamycin anthracycline antibiotic that can induce cancer cell death via DNA intercalation, inhibition of topoisomerase II, and formation of free radicals [7, 8]. However, the nonspecific effects of doxorubicin are numerous, and include systemic toxicity, tissue necrosis, neutropenia, and cardiomyopathy [9, 10]. Nanobiotechnology has contributed to the development of novel drug delivery vehicles to both enhance the efficiency of doxorubicin while reducing its toxic effects, such as polymers, dendrimers, and liposomes [11]. Liposomal doxorubicin (L-DXR) in particular has been shown to enhance overall drug efficacy by altering pharmacokinetics, increasing circulation time, and reducing non-specific toxic effects [12–14]. Polyethylene glycol (PEG) conjugation to the liposome surface provides steric stabilization and increased circulation time of the drug and can also aid in tumor uptake due to enhanced permeability and retention effects [14, 15]. The efficacy of L-DXR has been shown clinically as evidenced by Doxil, which has been approved by the FDA

for use in treating Kaposi's sarcoma [16]. However, current L-DXR formulations lack the targeting mechanisms to treat individual CTCs in the bloodstream, due to the rarity of CTCs amongst healthy circulating blood cells. The concentration of CTCs in the bloodstream of patients is approximately one in a million leukocytes [17] or one in a billion of all healthy blood cells [18].

Cell adhesion molecules known as selectins hold promise in targeting drug delivery vehicles to CTCs under physiological shear flow, due to their rapid, force-dependent binding kinetics [19, 20]. Sialylated carbohydrate ligands are expressed on the surface of many CTCs, which have the ability to bind to selectin proteins on the inflamed endothelium during metastasis [21–23]. Targeting of CTCs in the bloodstream via selectin-mediated adhesion could reduce the probability of metastasis. However, healthy circulating leukocytes are also known to express sialylated carbohydrate ligands on their surface [24]. Thus, strategies to reduce healthy blood cell adhesion are required for selectin-mediated targeting of therapies to CTCs.

The development of nanostructured surfaces to enhance the capture of CTCs for chemotherapeutic delivery while preventing healthy cell adhesion has not been yet investigated. Here, we assessed the application of a nanostructured surface consisting of halloysite nanotubes and nanoscale L-DXR to increase cancer cell recruitment while preventing leukocyte adhesion.

2. Materials and Methods

2.1. Cell Culture. Colorectal adenocarcinoma cell line COLO 205 (ATCC #CCL-222) and breast adenocarcinoma cell line MCF7 (ATCC no. HTB-22) were purchased from American Type Culture Collection (Manassas, VA, USA). COLO 205 cells were cultured in RPMI 1640 medium supplemented with 10% (v/v) fetal bovine serum and 1% (v/v) PenStrep, all purchased from Invitrogen (Grand Island, NY, USA). MCF7 cells were cultured in Eagle's Minimum Essential Medium (EMEM) supplemented with 0.01 mg/mL bovine insulin, 10% (v/v) fetal bovine serum, and 1% (v/v) PenStrep, all purchased from Invitrogen. All cancer cell lines were incubated under humidified conditions at 37°C and 5% CO₂ and were not allowed to exceed 90% confluence.

2.2. Neutrophil Isolation. Neutrophils were isolated as previously described [25]. Briefly, human peripheral blood was obtained from healthy blood donors after informed consent via venipuncture and collected using sterile sodium heparin-containing tubes (BD Biosciences, San Jose, CA, USA). Neutrophils were isolated from blood by centrifugation at 480 ×g for 50 min at 23°C, in a Marathon 8 K centrifuge (Fisher Scientific, Pittsburgh, PA, USA) using 1-Step Polymorphs (Accurate Chemical & Scientific Corporation, Westbury, NY, USA). Neutrophils were extracted and washed in Mg²⁺ and Ca²⁺-free Hank's balanced salt solution (HBSS), and all remaining red blood cells in the suspension were lysed hypotonically. Neutrophils were resuspended at a concentration of 1.0 × 10⁶ cells/mL in HBSS containing 0.5%

HSA, 2 mM Ca²⁺ and 10 mM HEPES (Invitrogen), buffered to pH 7.4.

2.3. Liposomal Doxorubicin Synthesis. Nanoscale liposomes were synthesized as described previously [26]. Briefly, lipids were dried overnight and rehydrated using a thin lipid film hydration method [27, 28] with 125 mM ammonium sulfate (Sigma-Aldrich, St. Louis, MO, USA). Lipids were then subjected to 10 freeze-thaw cycles and extruded to prepare empty liposomes (EL). Doxorubicin hydrochloride (Sigma-Aldrich) was encapsulated within ELs using an ammonium sulfate remote loading method, at a doxorubicin-to-lipid ratio of 0.2:1 (w/w). Excess DXR was removed using gel exclusion chromatography with Sephadex G-50 (Sigma-Aldrich). Liposomal doxorubicin concentration was determined by spectrophotometry ($\lambda = 490$ nm). The loading efficiency of doxorubicin was determined to be >95%.

2.4. Targeted Liposome Preparation. E-selectin functionalized L-DXR (ES-PEG L-DXR) and E-selectin functionalized empty liposomes (ES-PEG EL) were prepared using a post-insertion technique [29]. Recombinant human E-selectin/Fc chimera (rhE/Fc) (R&D Systems, Minneapolis, MN, USA) was thiolated and conjugated to 1,2-distearoyl-sn-glycero-3-phosphoethanolamine-N-maleimide 2000 (DSPE-PEG₂₀₀₀ maleimide) (Avanti Polar Lipids, Alabaster, AL, USA). To incorporate ES-polyethylene glycol (ES-PEG) conjugates into the lipid bilayer, ES-PEG was incubated with liposomes at 50°C for 30 min. Liposomes were stored at 4°C for <1 week until usage.

The mean particle diameter and zeta potential of the liposome formulations were measured by dynamic light scattering, using a Malvern Zetasizer Nano ZS (Malvern Instruments Ltd., Worcestershire, UK) according to the manufacturer's protocols. Mean particle diameter and zeta potential measurements of the liposome formulations were similar to values previously reported [26]. To determine successful E-selectin conjugation to liposome surface, 10 μ L of fluorescently tagged liposomes were mixed with 490 μ L of MCF7 cells (10⁶ cells/mL) and exposed to shear flow in a cone and plate viscometer at 2.0 dyn/cm² for 10 min. Fluorescent liposomes adhered to the cell surface were measured using an Accuri C6 flow cytometer (Accuri Cytometers, Inc., Ann Arbor, MI, USA). To assess fluorescent liposome adhesion and internalization to MCF7 cells, sheared samples were incubated for 60 min at 37°C and then imaged using confocal microscopy.

2.5. Confocal Microscopy. Fluorescent ES-conjugated liposomes were used to verify selectin-mediated adhesion to cancer cells. Fluorescent lipids were synthesized using fluorescent BODIPY-cholesterol (Avanti Polar Lipids). Cells were incubated with 2 μ L of 10 mg/mL trihydrochloride trihydrate (Hoechst 33342) (Invitrogen, Carlsbad, CA, USA) for 15 minutes to image cell nuclei. Cells were then placed on glass coverslips and visualized with a Zeiss 710 Spectral Confocal Microscope System (Carl Zeiss MicroImaging GmbH, Jena, Germany) at 65x magnification with FITC and DAPI filters.

Images were processed using Zen 2009 light edition software (Carl Zeiss MicroImaging GmbH).

2.6. MCF7 Static Assays. MCF7 cells were cultured in complete media at a concentration of 1×10^5 cells/mL on 12-well plates (Becton Dickinson, Franklin Lakes, NJ, USA). Cells were treated with ES-PEG L-DXR, L-DXR, or EL at volumes of 0 to $5 \mu\text{L}$ for 18 hours. MCF7 cells were treated with Accutase (Sigma-Aldrich) for 5 min at 37°C , to remove adherent cells from the surface. Cells were then washed with phosphate buffered saline (PBS) at 1000 rpm in a refrigerated centrifuge (Allegra XX-22R Centrifuge; Beckman Coulter, Brea, CA, USA) and resuspended in fresh media. After 4 days, cell viability was evaluated on a hemocytometer (Hausser Scientific, Horsham, PA, USA) using a trypan blue exclusion assay (Lonza, Wilkerville, MD, USA). Cells were also treated with $0.5 \mu\text{L}$ of liposome solution and assessed for viability over a period of 1–4 days. Cell morphology and uptake of doxorubicin were imaged using brightfield and fluorescence microscopy, respectively.

2.7. Cancer Cell and Neutrophil Preparation for Capture Experiments. MCF7 and COLO 205 cells were treated with Accutase (Sigma, St. Louis, MO, USA) for 5–10 min before handling. MCF7 and COLO 205 cells were washed in PBS and resuspended at a concentration of 1.0×10^6 cells/mL, in a flow buffer of HBSS containing 0.5% HSA, 2 mM Ca^{2+} , and 10 mM HEPES (Invitrogen), buffered to pH 7.4. For neutrophil capture experiments, freshly isolated neutrophils were resuspended in flow buffer at a concentration of 1.0×10^6 cells/mL. For combined cell capture assays, MCF7 or COLO 205 cells were resuspended in flow buffer with neutrophils at a 1:1 cancer cell to neutrophil ratio, at a concentration of 1.0×10^6 cells/mL.

2.8. HNT-Liposome Surface Functionalization. Microrenatane microtubing (Braintree Scientific, Braintree, MA, USA) of inner diameter $300 \mu\text{m}$ was cut to 55 cm in length and washed with 75% ethanol. To prepare HNT-coated microtube surfaces, a 6.6% by weight HNT solution (NaturalNano, Rochester, NY, USA) was treated via sonication, followed by filtration [26]. Microtubes were washed using distilled water, followed by incubation with 2:8 poly-L-lysine (0.1% w/v, Sigma) for 5 min and then incubation with treated HNT solution for 3 min. Microtubes were washed thoroughly with distilled water to remove excess HNTs in solution and were incubated overnight at RT. Surface immobilization of liposomes was achieved by incubating E-selectin functionalized liposome solution (ES-PEG L-DXR or ES-PEG EL) for 2.5 hours within HNT-coated microtubes. Smooth microtubes were prepared by immobilizing liposomes on the surface in the absence of HNTs. All surfaces were blocked for non-specific adhesion for 1 h with 5% bovine serum albumin (BSA) (Sigma-Aldrich) in PBS (w/v). All incubation steps were preceded and followed by thorough washes with PBS. Immobilized E-selectin proteins were activated prior to cell capture experiments via perfusion of calcium-enriched flow buffer.

2.9. Capture Experiments. To visualize cell adhesion and capture, functionalized microtubes were secured onto the stage of an Olympus IX81 motorized inverted microscope (Olympus, Center Valley, PA, USA). A motorized syringe pump (KDS 230; IITC Life Science, Woodland Hills, CA, USA) was used to perfuse cell suspensions through microtubes at physiologically relevant flow rates. Cancer cells and combined cell solutions were initially perfused through microtubes at a rate of 0.008 mL/min (wall shear stress of 0.5 dynes/cm^2) for 30 min, and then 0.04 mL/min (wall shear stress of 2.5 dynes/cm^2) for another 30 min. Isolated neutrophils were perfused at 0.04 mL/min for 60 min. Microtubes were washed with calcium-enriched PBS at 1.0 dyn/cm^2 to remove all nonadherent cells. Accutase was gently perfused into the microtube and allowed to incubate for 10 min to detach adherent cells, followed by perfusion of medium for cell collection. For combined cell assays, neutrophils were separated from cancer cell by centrifugation using 1-Step Polymorphs after cell collection. Cells were cultured in 6-well plates in complete media and analyzed for cell viability at day 4 via trypan blue exclusion.

2.10. Data Acquisition. Videos of cell capture experiments were recorded using a microscope-linked Hitachi CCD camera KP-M1AN (Hitachi, Japan) and a Sony DVD Recorder DVO-1000MD (Sony Electronics Inc., San Diego, CA, USA). Video frames were utilized to determine the number of captured cells per $100,000 \mu\text{m}^2$. For combined cell experiments, cancer cell and neutrophil capture measurements were determined based on differences in cell diameter.

2.11. Shape Factor Analysis. Brightfield images of neutrophils captured in smooth and HNT-coated tubes were analyzed for morphological changes using a shape factor analysis. Outlines of neutrophils were created from thresholded brightfield images using edge-detection functions in Metamorph software (Universal Imaging Corp., West Chester, PA, USA). Neutrophil morphological changes were determined using a shape factor program in Metamorph, where shape factor is determined by:

$$\text{shape factor} = \frac{4\pi A}{P^2}, \quad (1)$$

where P is the perimeter and A is the area of the object (neutrophil). Shape factor values close to 1 correspond to a circle, while values approaching 0 represent spindly or dendritic shapes.

2.12. Statistical Analysis. Data sets were plotted and analyzed using Prism 5.0b for Mac OS X (GraphPad software, San Diego, CA, USA). All results were reported as the mean \pm standard error of the mean. A two-tailed paired t -test was used for comparisons between two groups. P -values less than 0.05 were considered significant.

3. Results and Discussion

3.1. ES-PEG L-DXR Targets and Induces Cell Death in MCF7 Breast Cancer Cells. To assess the functionality of E-selectin

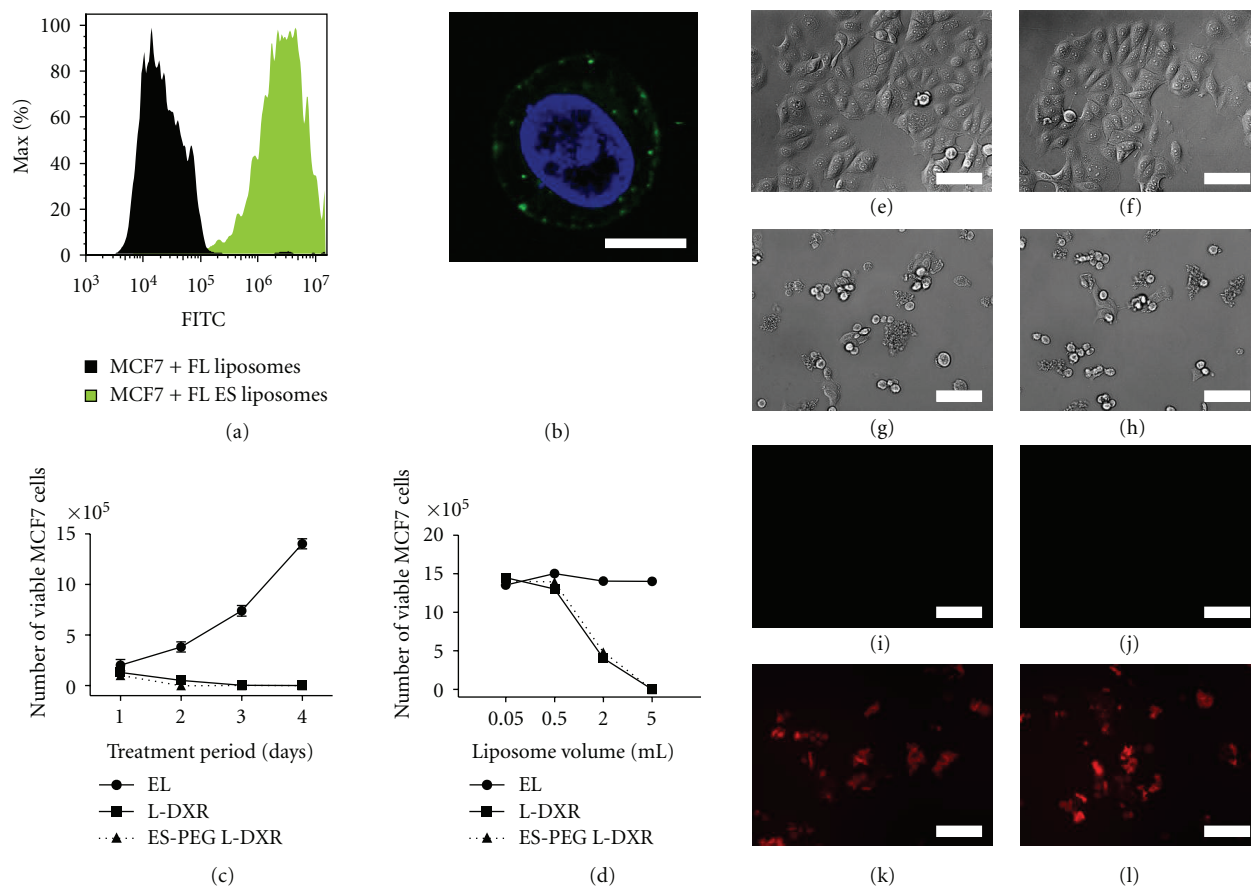


FIGURE 1: Liposomes functionalized with E-selectin (ES) adhesively bind and deliver doxorubicin to MCF7 breast cancer cells. (a) Flow cytometry fluorescence histograms of MCF7 cells adhered to fluorescently tagged (FL) liposomes and FL ES functionalized liposomes after exposure to fluid shear stress in a cone-and-plate viscometer. FITC: Fluorescein isothiocyanate. (b) Confocal microscopy image of FL ES liposomes (green) bound to MCF7 cells after fluid shear stress exposure. Cell nucleus = blue. Scale bar = 10 μm . (c) Number of viable MCF7 cells after treatment with empty liposomes (EL), liposomal doxorubicin (L-DXR) or ES functionalized L-DXR (ES-PEG L-DXR) under static conditions for a period of 1–4 days. (d) Dose response of MCF7 cells after treatment with liposomes over a 4-day period. ((e)–(h)) Bright field microscopy images of untreated MCF7 cells (e) and those treated with EL (f), L-DXR (g), and ES-PEG L-DXR (h) after a 4-day period. Scale bars = 100 μm . ((i)–(l)) Fluorescence microscopy images of doxorubicin uptake (red) of untreated MCF7 cells (i) and those treated with EL (j), L-DXR (k), and ES-PEG L-DXR (l) after a 4-day period.

conjugated to the liposome surface, fluorescently tagged ES-PEG L-DXR was incubated with human breast cancer MCF7 cells and sheared in a cone-and-plate viscometer for 10 min at 2.0 dyn/cm^2 . MCF7 cells have been previously shown to roll on ES-coated surfaces, a process that is mediated by CD24 expressed on the MCF7 cell surface [30]. MCF7 cells sheared with fluorescent ES-PEG L-DXR increased in fluorescence by >99.9%, compared to MCF7 cells sheared with fluorescent liposomes lacking E-selectin (Figure 1(a)). Confocal microscopy revealed that ES-PEG L-DXR not only binds to the cancer cell surface, but also internalizes within the cell over time (Figure 1(b)), making this targeting mechanism well suited for the internalization of ES-PEG L-DXR within cancer cells. Static assays verified cellular uptake and cytotoxicity of ES-PEG L-DXR at levels comparable to L-DXR (Figures 1(c) and 1(d)). MCF7 cells treated with either L-DXR (Figure 1(g)) or ES-PEG L-DXR (Figure 1(h)) had observable membrane blebbing and were non-adherent,

characteristic of MCF7 cell death. MCF7 cells treated with EL (Figure 1(f)) were adherent and displayed a morphology similar to healthy, untreated MCF7 cells (Figure 1(e)). Fluorescence microscopy confirmed comparable doxorubicin uptake in MCF7 cells treated with L-DXR (Figure 1(k)) and ES-PEG L-DXR (Figure 1(l)), compared to control samples in the absence of doxorubicin (Figures 1(i) and 1(j)). It is apparent from these images that E-selectin adhesion to the cell surface does not hinder internalization and cytotoxic effects of L-DXR on MCF7 cells, making this targeting mechanism suitable for MCF7 treatment under physiological flow.

3.2. Nanostructured Surfaces Enhance MCF7 and COLO 205 Cell Adhesion to ES-PEG L-DXR. Our lab has previously demonstrated that selectin proteins and selectin-coated nanoparticles can be immobilized on the inner surfaces of microtubes for the capture of circulating cells [31], as well as

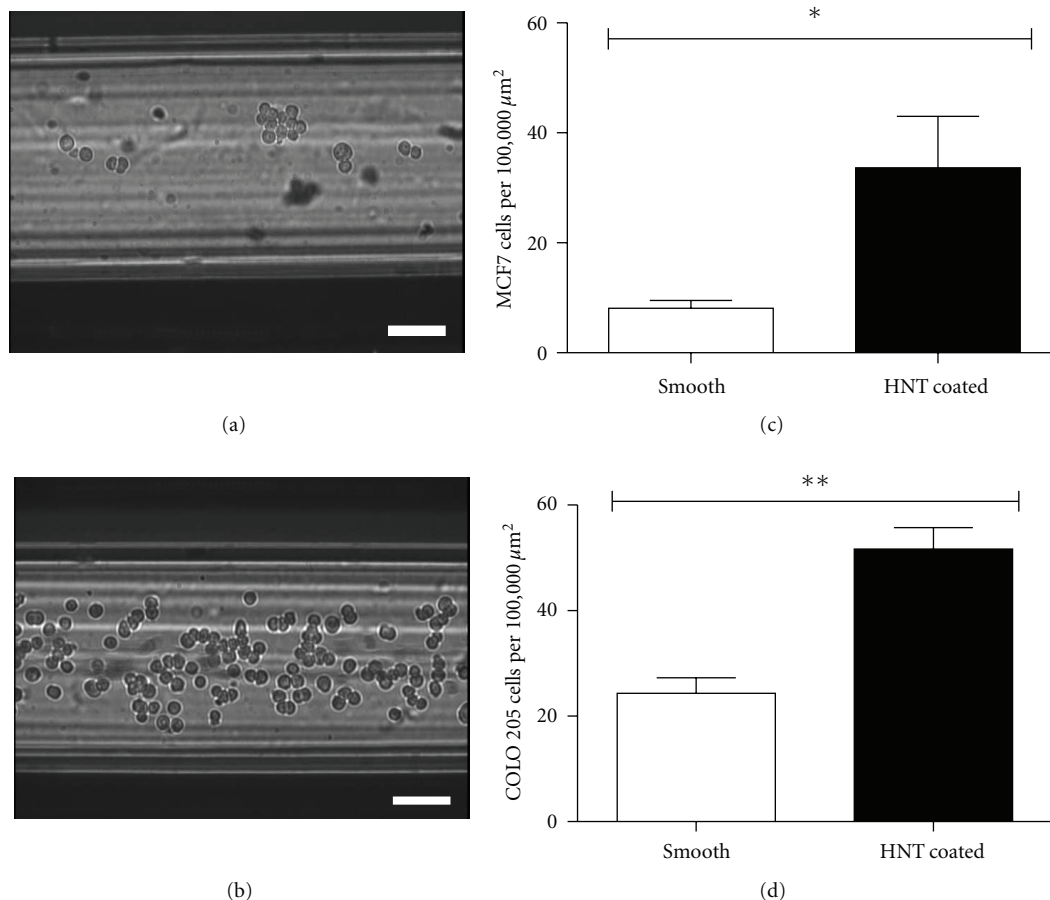


FIGURE 2: HNT-liposome-coated surfaces enhance MCF7 and COLO 205 cell capture. (a) MCF7 breast cancer cells adhered to a smooth microtube coated with ES-PEG L-DXR. Scale bar = 100 μm . (b) MCF7 cells adhered to an HNT-coated microtube with ES-PEG L-DXR. Scale bar = 100 μm . (c) Number of MCF7 cells adhered to smooth and HNT-coated microtubes per 100,000 μm^2 . (d) Number of COLO 205 cells adhered to smooth and HNT-coated microtubes per 100,000 μm^2 . * $P < 0.01$. ** $P < 0.001$.

for use as *in vitro* models of the microvasculature to examine the rolling adhesion of leukocytes [32] and cancer cells [33]. In this study, smooth microtubes were coated with only ES-PEG L-DXR. HNT-liposome-coated microtubes were coated with HNTs, followed by ES-PEG L-DXR immobilization. MCF7 or COLO 205 cells were perfused through microtubes at shear stresses (0.5–2.5 dyn/cm^2) observed in the microvasculature *in vivo* [34]. Both cell lines were chosen as model CTCs because they express sialylated carbohydrate ligands and exhibit rolling adhesion properties on immobilized E-selectin surfaces [30, 35]. MCF7 cells were captured from flow in both smooth (Figure 2(a)) and HNT-liposome-coated microtubes (Figure 2(b)). However, an increased number of MCF7 cells were captured on HNT-liposome-coated surfaces, compared to smooth surfaces. A significant three fold increase in MCF7 (Figure 2(c)) and two fold increase in COLO 205 cell capture (Figure 2(d)) per 100,000 μm^2 were observed on HNT-liposome-coated surfaces, compared to smooth surfaces coated with ES-PEG L-DXR. HNT-coated microtubes have been previously shown to increase the adsorption of selectin proteins [36], compared to the adsorption of selectins within microtubes in the absence of HNTs. It is likely that HNT coatings can also enhance

the deposition of ES-PEG L-DXR, which could increase the recruitment of flowing cancer cells.

3.3. Nanostructured Surfaces Reduce Neutrophil Adhesion to ES-PEG L-DXR. While HNT-coated surfaces can enhance the delivery of chemotherapeutics to CTCs via selectin-mediated adhesion, it is also important to examine the effects of such surface interactions with healthy blood cells. Leukocytes, which express sialylated carbohydrate ligands, outnumber CTCs by roughly one million to one in patients, on average [37]. Thus, leukocytes could potentially uptake the majority, if not all of the encapsulated chemotherapeutic being delivered. However, capture assays revealed that the number of neutrophils adhered to HNT-liposome-coated surfaces (Figure 3(b)) was largely diminished compared to smooth surfaces (Figure 3(a)), the opposite of the trend observed in cancer cell capture studies. Similar trends were also observed in the isolation of CTCs from a suspension of mononuclear cells [38]. A significant >94% reduction of neutrophils captured per 100,000 μm^2 was confirmed in HNT-liposome-coated microtubes, compared to smooth microtubes coated with ES-PEG L-DXR (Figure 3(c)).

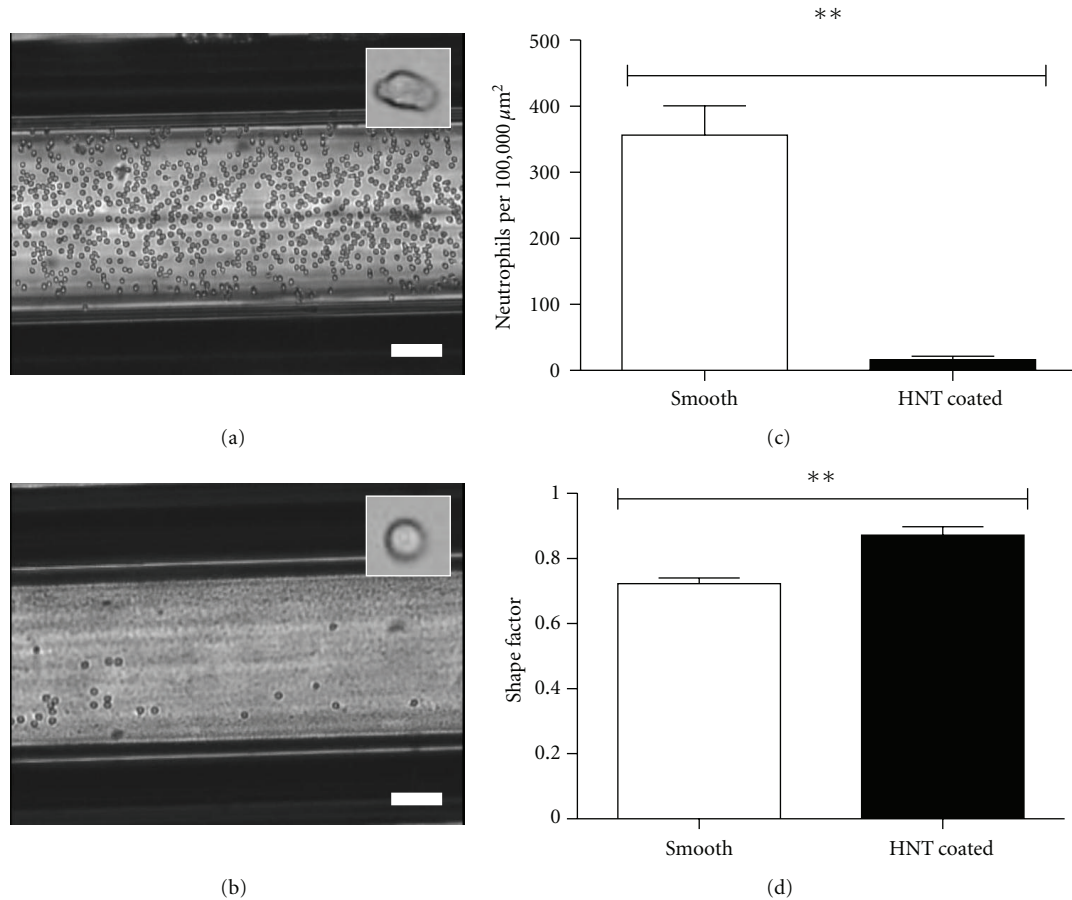


FIGURE 3: HNT-liposome-coated surfaces reduce and weaken neutrophil adhesion. (a) Neutrophils adhered to a smooth microtube coated with ES-PEG L-DXR. Scale bar = 100 μm . (b) Neutrophils adhered to an HNT-coated microtube with ES-PEG L-DXR. Scale bar = 100 μm . Insets show representative cell shapes at higher magnification (approximately $20 \times 20 \mu\text{m}$). (c) Number of neutrophils adhered to smooth and HNT-coated microtubes per 100,000 μm^2 . (d) Shape factor analysis of neutrophils adhered to smooth and HNT-coated microtubes. $**P < 0.001$.

Cytoskeletal projections known as pseudopods were observed consistently on neutrophils adhered to smooth surfaces, characteristic of firmly adhered and activated neutrophils (Figure 3(a)) [24]. Neutrophils on HNT-liposome-coated surfaces displayed a rounder morphology, characteristic of weaker adhesion of resting neutrophils (Figure 3(b)). Shape factor analysis has previously been utilized to assess neutrophil morphological changes [26] and was performed in this study to determine the effect of adhesion to HNT-liposome-coated surfaces on morphological changes. On a scale of 0 (elongated shapes) to 1 (circularity), shape factor analysis verified a significantly higher shape factor in neutrophils adhered to HNT-liposome-coated surfaces (Figure 3(d)), compared to those adhered to smooth surfaces, adding further support that neutrophils display weaker adhesion on HNT-liposome-coated surfaces.

To examine if the reduction in neutrophil adhesion is due to prevention of ES-PEG L-DXR adsorption to the surface, ES-PEG L-DXR was fluorescently tagged and immobilized on smooth and HNT-coated microtubes. However, fluorescence microscopy confirmed that ES-PEG L-DXR immobilized within both smooth (Figure 4(b)) and

HNT-coated microtubes (Figure 4(c)), compared to control microtubes in the absence of fluorescent ES-PEG L-DXR (Figure 4(a)). Thus, the reduction in neutrophil adhesion could not be caused by prevention of ES-PEG L-DXR adsorption.

3.4. HNT-Liposome Surfaces Capture Cancer Cells and Repel Neutrophils from a Mixture of Cells. The use of HNT-liposome-coated surfaces for CTC capture from a combined cell suspension was assessed via perfusion of a 1 : 1 mixture of cancer cells and neutrophils over liposome-coated surfaces. Neutrophils and MCF7 cells were identified based on size; cells 15 μm in diameter or less were identified as neutrophils, while cells greater than 15 μm were identified as MCF7 or COLO 205 cells. Upon perfusion of neutrophils and MCF7 cells, the number of neutrophils captured decreased on HNT-liposome-coated surfaces (Figure 5(b)) compared to smooth surfaces (Figure 5(a)). Simultaneously, an increase in MCF7 cell capture was observed on HNT-liposome-coated surfaces (Figure 5(b)), compared to smooth surfaces (Figure 5(a)). The number of both MCF7 (Figure 5(c)) and COLO 205 (Figure 5(d)) cells captured was significantly

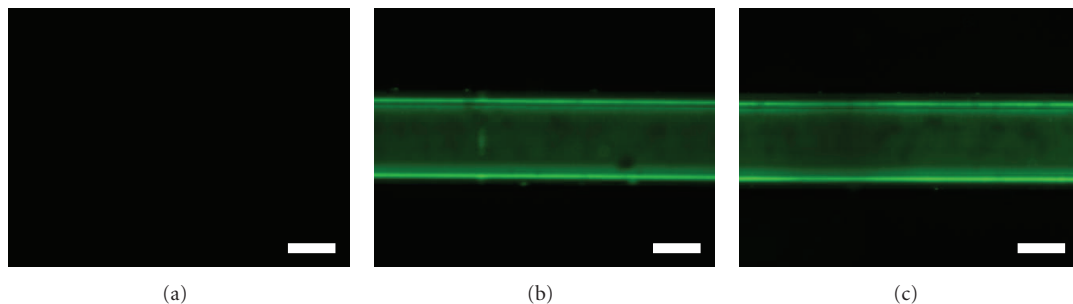
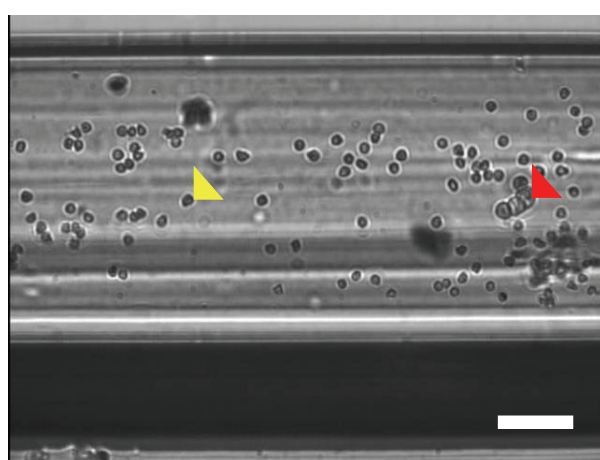
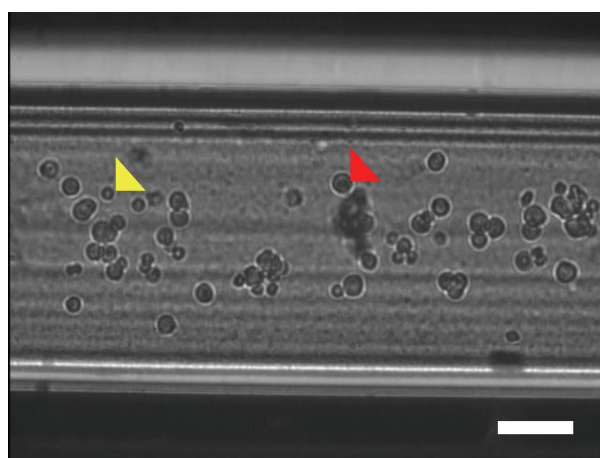


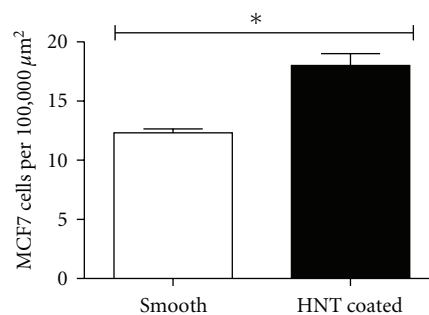
FIGURE 4: E-selectin functionalized liposomes immobilize on both smooth and HNT-coated microtube surfaces. ((a)–(c)) Fluorescence microscopy images of microtubes coated with BSA (a), smooth microtubes coated with fluorescent ES-PEG L-DXR (b), and HNT-coated microtubes with immobilized fluorescent ES-PEG L-DXR (c). Scale bar = 100 μm .



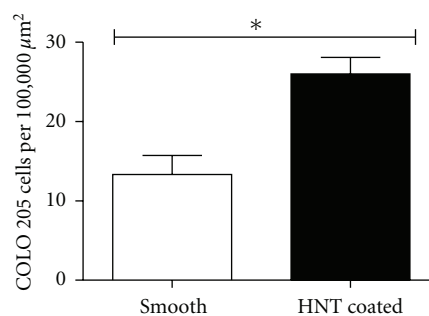
(a)



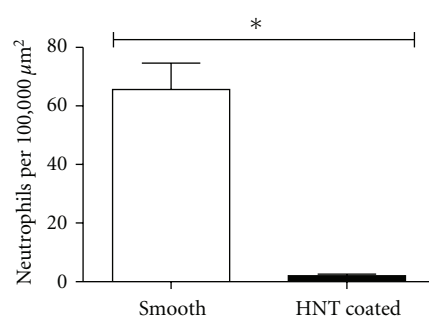
(b)



(c)



(d)



(e)

FIGURE 5: HNT-liposome surfaces simultaneously enhance MCF7 and COLO 205 cell adhesion and reduce neutrophil adhesion from a combined suspension of cancer cells and neutrophils. (a) MCF7 cells (red arrow) and neutrophils (yellow arrow) adhered to a smooth microtube coated with ES-PEG L-DXR. Scale bar = 100 μm . (b) MCF7 cells (red arrow) and neutrophils (yellow arrow) adhered to an HNT-coated microtube with immobilized ES-PEG L-DXR. Scale bar = 100 μm . (c) Number of MCF7 cells adhered to smooth and HNT-coated microtubes per 100,000 μm^2 . (d) Number of COLO 205 cells adhered to smooth and HNT-coated microtubes per 100,000 μm^2 . (e) Number of neutrophils adhered to smooth and HNT-coated microtubes per 100,000 μm^2 . * $P < 0.01$.

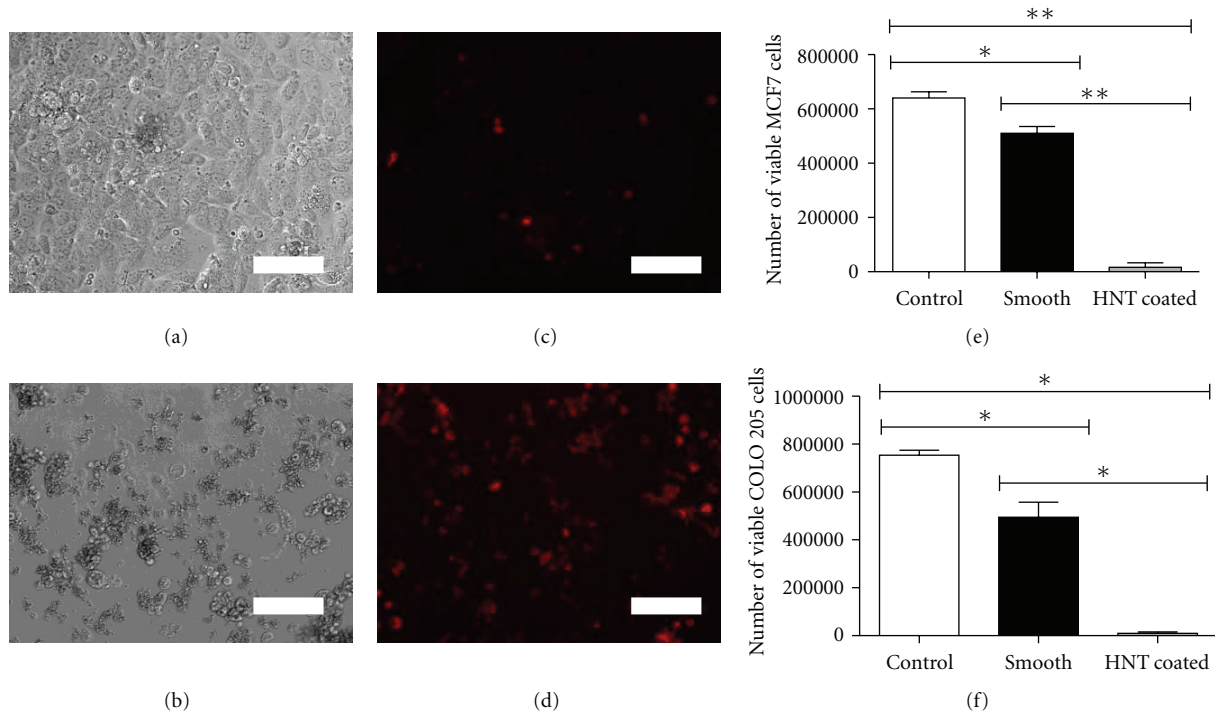


FIGURE 6: HNT-liposome-coated surfaces successfully deliver doxorubicin to cancer cells from a combined solution of cancer cells and neutrophils. Brightfield images of MCF7 cells captured on a smooth surface (a) and an HNT-liposome-coated surface (b), from a combined solution of cancer cells and neutrophils. Internalization of doxorubicin (red) in MCF7 cells captured on a smooth surface (c) and an HNT-liposome-coated surface (d), from a combined solution of cancer cells and neutrophils. All images were taken after 4-day incubation at 37°C. Scale bar = 100 μm . Number of viable MCF7 (e) and COLO 205 (f) cells after capture on smooth and HNT-liposome-coated surfaces. Control samples represent viable cells captured by ES-PEG EL. * $P < 0.01$. ** $P < 0.001$.

increased on HNT-liposome-coated surfaces, with significant reductions in neutrophil capture (Figure 5(e)).

3.5. HNT-Liposome Surfaces Induce Cancer Cell Death within a Mixture of Cancer Cells and Neutrophils. The ability to successfully deliver doxorubicin to cancer cells within a combined cell suspension was assessed by the removal and collection of captured cells from surfaces, separation of cancer cells from neutrophils, and placement into culture for viability tests. Neutrophils, which have a short lifespan *in vivo* and typically undergo cell death *in vitro* within 18–28 hours after isolation [39], showed negligible differences in viability whether captured within microtubes or placed directly into culture upon isolation (not shown). After a 4-day incubation, brightfield microscopy confirmed that while MCF7 cells captured on smooth surfaces were adherent and displayed healthy morphology (Figure 6(a)). However, MCF7 cells captured on HNT-liposome-coated surfaces were non-adherent and displayed significant membrane blebbing characteristic of apoptosis (Figure 6(b)). MCF7 cells captured on smooth surfaces exhibited minimal doxorubicin uptake based on fluorescence images (Figure 6(c)), while MCF7 cells captured on HNT-liposome-coated surfaces displayed increased doxorubicin uptake (Figure 6(d)). Cell viability assays confirmed doxorubicin-induced cell death, with a significant decrease in MCF7 (Figure 6(e)) and COLO 205 cell viability (Figure 6(f)) when captured on

smooth tubes coated with ES-PEG L-DXR, compared to control smooth surfaces coated with ES-PEG EL. However, the number of viable MCF7 and COLO 205 cells captured on HNT-liposome-coated surfaces was significantly reduced, compared to the number of viable cells captured on smooth surfaces. Similar trends were observed previously in KG-1a and COLO 205 cells captured from a solution consisting only of cancer cells [26]. These results demonstrate that a combined surface of HNTs and ES-PEG L-DXR can serve a dual role in: (1) delivering chemotherapeutics to CTCs and (2) reducing leukocyte adhesion and interaction with chemotherapeutics and thus reducing toxic side effects on healthy blood cells.

4. Conclusion

Here, we have demonstrated a technique utilizing cell adhesion molecules to deliver therapeutics to CTCs while actively preventing blood cell adhesion. ES-PEG L-DXR was shown to adhesively interact with MCF7 breast cancer cells and induce cell death. Under physiological flow rates, HNT-liposome-coated surfaces significantly increased the number of captured MCF7 and COLO 205 cancer cells, compared to smooth surfaces coated with ES-PEG L-DXR. The opposite trend occurred with healthy blood cells, as perfusion of neutrophils over HNT-liposome coated surfaces significantly reduced the number of captured cells. In a combined

solution of cancer cells and neutrophils, HNT-liposome-coated surfaces simultaneously increased the number of MCF7 and COLO 205 cells captured, while significantly reducing neutrophil capture to minimum levels. Liposomal doxorubicin was successfully delivered to MCF7 and COLO 205 cells in flow assays with a combined solution of cancer cells and neutrophils. The application of HNT-liposome surfaces can enhance chemotherapeutic delivery to CTCs and reduce the probability of metastasis. Additionally, the unique ability of such surfaces to prevent normal blood cell interactions can reduce toxic non-specific effects and dramatically reduce chemotherapeutic dosages required for CTC treatment.

Acknowledgments

This work was supported by the National Institutes of Health, Grant no. CA143876. The authors acknowledge Jeff Mattison for work with blood sample collection and donor recruitment.

References

- [1] C. L. Chaffer and R. A. Weinberg, "A perspective on cancer cell metastasis," *Science*, vol. 331, no. 6024, pp. 1559–1564, 2011.
- [2] A. D. Hughes and M. R. King, "Nanobiotechnology for the capture and manipulation of circulating tumor cells," *WIREs Nanomedicine and Nanobiotechnology*, vol. 4, no. 3, pp. 291–309, 2011.
- [3] L. M. Coussens and Z. Werb, "Inflammation and cancer," *Nature*, vol. 420, no. 6917, pp. 860–867, 2002.
- [4] A. F. Chambers, G. N. Naumov, S. A. Vantyghem, and A. B. Tuck, "Molecular biology of breast cancer metastasis. Clinical implications of experimental studies on metastatic inefficiency," *Breast Cancer Research*, vol. 2, no. 6, pp. 400–407, 2000.
- [5] I. C. MacDonald, A. C. Groom, and A. F. Chambers, "Cancer spread and micrometastasis development: quantitative approaches for in vivo models," *BioEssays*, vol. 24, no. 10, pp. 885–893, 2002.
- [6] R. C. Young, R. F. Ozols, and C. E. Myers, "The anthracycline antineoplastic drugs," *The New England Journal of Medicine*, vol. 305, no. 3, pp. 139–153, 1981.
- [7] J. Bouma, J. H. Beijnen, A. Bult, and W. J. M. Underberg, "Anthracycline antitumour agents. A review of physico-chemical, analytical and stability properties," *Pharmaceutisch Weekblad*, vol. 8, no. 3, pp. 109–133, 1986.
- [8] N. Osheroff, A. H. Corbett, and M. J. Robinson, "Mechanism of action of topoisomerase II-targeted antineoplastic drugs," *Advances in Pharmacology*, vol. 29, pp. 105–126, 1994.
- [9] L. H. Reddy, "Drug delivery to tumours: recent strategies," *Journal of Pharmacy and Pharmacology*, vol. 57, no. 10, pp. 1231–1242, 2005.
- [10] A. Fritze, F. Hens, A. Kimpfler, R. Schubert, and R. Peschka-Süss, "Remote loading of doxorubicin into liposomes driven by a transmembrane phosphate gradient," *Biochimica et Biophysica Acta*, vol. 1758, no. 10, pp. 1633–1640, 2006.
- [11] M. Saad, O. B. Garbuzenko, E. Ber et al., "Receptor targeted polymers, dendrimers, liposomes: which nanocarrier is the most efficient for tumor-specific treatment and imaging?" *Journal of Controlled Release*, vol. 130, no. 2, pp. 107–114, 2008.
- [12] E. H. Herman, A. Rahman, and V. J. Ferrans, "Prevention of chronic doxorubicin cardiotoxicity in beagles by liposomal encapsulation," *Cancer Research*, vol. 43, no. 11, pp. 5427–5432, 1983.
- [13] R. Krishna, N. McIntosh, K. W. Riggs, and L. D. Mayer, "Doxorubicin encapsulated in sterically stabilized liposomes exhibits renal and biliary clearance properties that are independent of valspodar (PSC 833) under conditions that significantly inhibit nonencapsulated drug excretion," *Clinical Cancer Research*, vol. 5, no. 10, pp. 2939–2947, 1999.
- [14] A. Gabizon, H. Shmeeda, and Y. Barenholz, "Pharmacokinetics of pegylated liposomal doxorubicin: review of animal and human studies," *Clinical Pharmacokinetics*, vol. 42, no. 5, pp. 419–436, 2003.
- [15] H. D. Han, A. Lee, T. Hwang et al., "Enhanced circulation time and antitumor activity of doxorubicin by comblike polymer-incorporated liposomes," *Journal of Controlled Release*, vol. 120, no. 3, pp. 161–168, 2007.
- [16] B. Čeh, M. Winterhalter, P. M. Frederik, J. J. Vallner, and D. D. Lasic, "Stealth liposomes: from theory to product," *Advanced Drug Delivery Reviews*, vol. 24, no. 2–3, pp. 165–177, 1997.
- [17] W. J. Allard, J. Matera, M. C. Miller et al., "Tumor cells circulate in the peripheral blood of all major carcinomas but not in healthy subjects or patients with nonmalignant diseases," *Clinical Cancer Research*, vol. 10, no. 20, pp. 6897–6904, 2004.
- [18] S. Maheswaran and D. A. Haber, "Circulating tumor cells: a window into cancer biology and metastasis," *Current Opinion in Genetics and Development*, vol. 20, no. 1, pp. 96–99, 2010.
- [19] G. S. Kansas, "Selectins and their ligands: current concepts and controversies," *Blood*, vol. 88, no. 9, pp. 3259–3287, 1996.
- [20] J. Li and M. R. King, "Adhesion receptors as therapeutic targets for circulating tumor cells," *Frontiers in Oncology*, vol. 2, article 79, 2012.
- [21] H. Läubli and L. Borsig, "Selectins promote tumor metastasis," *Seminars in Cancer Biology*, vol. 20, no. 3, pp. 169–177, 2010.
- [22] T. Krause and G. A. Turner, "Are selectins involved in metastasis?" *Clinical and Experimental Metastasis*, vol. 17, no. 3, pp. 183–192, 1999.
- [23] S. Gout, P. L. Tremblay, and J. Huot, "Selectins and selectin ligands in extravasation of cancer cells and organ selectivity of metastasis," *Clinical and Experimental Metastasis*, vol. 25, no. 4, pp. 335–344, 2008.
- [24] T. A. Springer, "Traffic signals for lymphocyte recirculation and leukocyte emigration: the multistep paradigm," *Cell*, vol. 76, no. 2, pp. 301–314, 1994.
- [25] M. J. Mitchell and M. R. King, "Shear-induced resistance to neutrophil activation via the formyl peptide receptor," *Biophysical Journal*, vol. 102, no. 8, pp. 1804–1814, 2012.
- [26] M. J. Mitchell, C. S. Chen, V. Ponnudi, A. D. Hughes, and M. R. King, "E-selectin liposomal and nanotube-targeted delivery of doxorubicin to circulating tumor cells," *Journal of Controlled Release*, vol. 160, no. 3, pp. 609–617, 2012.
- [27] S. Amselem, R. Cohen, S. Druckmann et al., "Preparation and characterization of liposomal doxorubicin for human use," *Journal of Liposome Research*, vol. 2, no. 1, pp. 93–123, 1992.
- [28] G. Haran, R. Cohen, L. K. Bar, and Y. Barenholz, "Transmembrane ammonium sulfate gradients in liposomes produce efficient and stable entrapment of amphipathic weak bases," *Biochimica et Biophysica Acta*, vol. 1151, no. 2, pp. 201–215, 1993.
- [29] A. N. Lukyanov, T. A. Elbayoumi, A. R. Chakilam, and V. P. Torchilin, "Tumor-targeted liposomes: doxorubicin-loaded long-circulating liposomes modified with anti-cancer

- antibody," *Journal of Controlled Release*, vol. 100, no. 1, pp. 135–144, 2004.
- [30] J. H. Myung, K. A. Gajjar, R. M. Pearson, C. A. Launier, D. T. Eddington, and S. Hong, "Direct measurements on CD24-mediated rolling of human breast cancer MCF-7 cells on E-selectin," *Analytical Chemistry*, vol. 83, no. 3, pp. 1078–1083, 2011.
- [31] Z. Huang and M. R. King, "An immobilized nanoparticle-based platform for efficient gene knockdown of targeted cells in the circulation," *Gene Therapy*, vol. 16, no. 10, pp. 1271–1282, 2009.
- [32] D. Lee, J. B. Schultz, P. A. Knauf, and M. R. King, "Mechanical shedding of L-selectin from the neutrophil surface during rolling on sialyl lewis x under flow," *The Journal of Biological Chemistry*, vol. 282, no. 7, pp. 4812–4820, 2007.
- [33] X. Yin, K. Rana, V. Ponmudi, and M. R. King, "Knockdown of fucosyltransferase III disrupts the adhesion of circulating cancer cells to E-selectin without affecting hematopoietic cell adhesion," *Carbohydrate Research*, vol. 345, no. 16, pp. 2334–2342, 2010.
- [34] M. B. Kim and I. H. Sarelius, "Distributions of wall shear stress in venular convergences of mouse cremaster muscle," *Microcirculation*, vol. 10, no. 2, pp. 167–178, 2003.
- [35] K. Rana, C. A. Reinhart-King, and M. R. King, "Inducing apoptosis in rolling cancer cells: a combined therapy with aspirin and immobilized TRAIL and E-selectin," *Molecular Pharmaceutics*, vol. 9, Article ID 120702, 2012.
- [36] A. D. Hughes and M. R. King, "Use of naturally occurring halloysite nanotubes for enhanced capture of flowing cells," *Langmuir*, vol. 26, no. 14, pp. 12155–12164, 2010.
- [37] B. T. Greene, A. D. Hughes, and M. R. King, "Circulating tumor cells: the substrate of personalized medicine?" *Frontiers in Oncology*, vol. 2, article 69, 2012.
- [38] A. D. Hughes, J. Mattison, L. T. Western, J. D. Powderly, B. T. Greene, and M. R. King, "Microtube device for selectin-mediated capture of viable circulating tumor cells from blood," *Clinical Chemistry*, vol. 58, no. 5, pp. 846–853, 2012.
- [39] C. G. Begley, A. F. Lopez, N. A. Nicola et al., "Purified colony-stimulating factors enhance the survival of human neutrophils and eosinophils in vitro: a rapid and sensitive microassay for colony-stimulating factors," *Blood*, vol. 68, no. 1, pp. 162–166, 1986.

Research Article

Formulation of LDL Targeted Nanostructured Lipid Carriers Loaded with Paclitaxel: A Detailed Study of Preparation, Freeze Drying Condition, and *In Vitro* Cytotoxicity

Jaber Emami, Mahboubeh Rezazadeh, Jaleh Varshosaz,
Majid Tabbakhian, and Abolfazl Aslani

Department of Pharmaceutics, School of Pharmacy and Pharmaceutical Sciences and Isfahan Pharmaceutical Research Center, Isfahan University of Medical Sciences, Isfahan 73461-8174, Iran

Correspondence should be addressed to Mahboubeh Rezazadeh, rezazade@pharm.mui.ac.ir

Received 11 October 2012; Accepted 13 November 2012

Academic Editor: Li-Hong Liu

Copyright © 2012 Jaber Emami et al. This is an open access article distributed under the Creative Commons Attribution License, which permits unrestricted use, distribution, and reproduction in any medium, provided the original work is properly cited.

In the present study, cholesterol nanostructured lipid carriers with various oleic acid content loaded with paclitaxel (PTX) were prepared by solvent emulsification-diffusion method using a Taguchi design. Size, zeta potential, entrapment efficiency, drug loading, and release percent of NLCs were measured. The results indicated that the most effective factors on the size were oleic acid content and surfactant percent. Zeta potential was more affected by the drug content. Drug to- lipid weight ratio was the most effective factor on entrapment efficiency and drug release from NLC. In the present work, the effect of lyophilization on the particle size and release properties of NLCs was also evaluated. The results revealed no differences between the characteristics of NLCs before and after freeze drying by using 25% w/w sorbitol as cryoprotectant. Cytotoxicity studies indicate that PTX associated with the NLC is also effective in HT-29 cell lines and enters the cancer cells selectively through the LDL receptor endocytic pathway. The IC_{50} values of free PTX solubilized in Cremophor EL and NLC-born PTX after 72 h exposure were 8.32 ± 1.35 ng/mL and 5.24 ± 0.96 ng/mL, respectively.

1. Introduction

Paclitaxel (PTX) is one of the most broadly active compounds prescribed to treat aggressive human malignancy such as cancers of ovary, breast, lung, head and neck, esophagus, bladder, endometrium, hematological and pediatric malignancies [1]. Low water solubility of PTX ($0.3 \mu\text{g/mL}$) and high toxicity have limited its clinical application. Currently, PTX is commercially available as Taxol in a vehicle composed of 1:1 of Cremophor EL (CrEL) and ethanol to enhance water solubility of the drug. Some serious effects associated with CrEL include hypersensitivity reactions, nephrotoxicity, and neurotoxicity. In addition, Taxol has short-term physical stability upon dilution due to the precipitation of PTX in the aqueous media. Other problems with ethanol and CrEL include leaching of plasticizer from polyvinyl chloride infusion bags and sets during injection of the drug [2]. Due to the above-mentioned

limitations, there is a need for new alternative formulations that can overcome poor aqueous solubility of PTX, deliver the drug more specifically to the target organs, and produce fewer side effects. Several approaches such as parenteral emulsions [3], liposomes [4], nanoparticles [5–7] complex with cyclodextrin [8], water soluble prodrugs [9], and polymeric micelles [10–15] have been employed to deliver PTX into the body or targeted tissue. Solid lipid nanoparticles (SLNs) are one of the carrier systems having more advantages over other colloidal delivery systems. These include biocompatibility, sterility, scale up, and protection of incorporated active ingredients against chemical degradation [16]. However, SLNs are associated with some potential limitations, namely, limited drug loading and drug expulsion during storage due to the crystallization of lipid matrix or lipid polymorphism. To overcome these limitations, nanostructured lipid carriers (NLCs) by mixing solid lipids with chemically very different liquid lipids (oils) have been

developed to improve drug loading and release properties of conventional SLNs. By using special mixtures of solid lipids and liquid lipids the particles become solid after cooling but do not crystallize which leads to more imperfections in the crystal and higher drug loading [17]. The objective of the present study was to prepare LDL targeted NLCs for delivery of PTX to the cancer cells. In this work for preparation of NLCs, oleic acid (OA) has been used as liquid lipid and cholesterol as solid lipid base. Based on previous published reports, cholesterol-rich nanoemulsion was taken-up by the low-density lipoprotein (LDL) receptors after injection into the bloodstream. Since most cancer cells show LDL receptors upregulation, cholesterol-fabricated nanoparticles can be used as carrier system to target antineoplastic drugs to cancerous cells [18]. Indeed, it was shown *in vitro* that cholesterol nanoemulsion internalizes drugs such as carmustine, etoposide, and paclitaxel into cultured neoplastic cells [19–21]. Therefore, it is postulated that our NLCs containing cholesterol may concentrate in cancerous cells with LDL receptor overexpression. After injection of the NLCs to the systemic circulation, cholesterol as the lipid base of the nanoparticles acquires apo E and other apolipoproteins from native lipoproteins. Apo E that is recognized by LDL receptors allows binding of the artificial NLCs to the receptors and internalize the carrier inside the cancer cells. Nanoemulsions are in liquid form and undergo instabilities such as flocculation, drug release, creaming, gelling, and aggregation of particles; whereas NLCs combine the advantages of polymeric nanoparticles, fat emulsions, and liposome [22]. Lipid nanoparticles that encapsulated paclitaxel have been studied by several groups [23–27]. In most of these studies carriers only achieved passive targeting due to the enhance permeation and retention (EPR) effect. In some of these published reports synergistic combination of passive and active targeting has been provided by chemical functionalizing the surface of nanocarriers with legends such as antibodies, peptides, or small molecules that recognize tumor-specific antigens which is complicated and expensive [23, 24]. But in our study, using cholesterol simply allows binding of the NLCs to the LDL receptors. This binding mediates internalization of the drug to the neoplastic cells. In this circumstance, the drug is largely released inside the cancer cells resulting enhanced efficiency.

Taguchi design L8 was used to optimize and evaluate the effect of different processing variables on characteristics of the NLCs.

In aqueous dispersed form, NLCs show an increase in particle size after a short period of time. So in subsequent study we aimed to increase the stability of NLCs using freeze-drying technique.

The prepared NLCs of PTX could not be lyophilized directly, and use of cryoprotectants was essential to prevent aggregation of the particles after reconstitution. In the current study, the freeze drying of the optimized formulation with or without cryoprotectants was also studied. Furthermore, effects of different variables such as the type and percentage of cryoprotectants and freezing temperature on the characteristics of the particles after freeze drying were also investigated. Moreover, we evaluated the cytotoxic effect

TABLE 1: Definition and trial levels of factors in Taguchi L8 orthogonal array experiment used in production of NLCs loaded with PTX.

Studied variable	Level 1	Level 2
Oleic acid content (w/w%)	15	30
Surfactant type	Poloxamer188	Tween80
Drug/lipid ratio %	5	10
Surfactant concentration %	1	2
Sonication time (min)	2	4
Homogenization rate (rpm)	800	1300

of the drug incorporated in NLCs and compared with those of free drug solutions on the human colorectal cancer cell line, HT-29.

2. Materials and Methods

2.1. Materials. Cholesterol, oleic acid, tween80, ethanol, and acetone were obtained from Merck (Germany). Poloxamer 188 and paclitaxel were from Sigma-Aldrich, (US). Avicel RC591 from (FMC, Brussels, Belgium), aerosol from (Evonik, Frankfurt Germany), mannitol from (Merk chemical company, Frankfurt Germany), dextrose from (Luzhou Bio-Chem, Shandong China), sorbitol, PEG4000 from (Frankfurt, Germany), HPLC grade acetonitrile, and methanol from Caledon (Canada). RPMI 1640 medium, sera, and antibiotics for cell culture were purchased from Sigma-Aldrich (US). Human colorectal cancer cells (HT-29) were obtained from Pasteur institute (Iran). 3-(4, 5-Dimethylthiazol-2-yl)-2, 5-diphenyl tetrazolium bromide (MTT) from Sigma- Aldrich (US).

2.2. Preparation of PTX-Loaded NLC. Different variables along with an overview of the formulations investigated in the present work are listed in Table 2. Different formulations are shown with different codes. The blank-and-drug loaded NLCs were prepared by an emulsion solvent diffusion and evaporation method followed by ultrasonication. Six variables were investigated in two levels. Briefly, 60 mg mixture of cholesterol and oleic acid (OA) at 15 or 30 wt% OA content and different amount of drug defined according to drug/lipid weight ratio (5 and 10 wt% PTX) were completely dissolved into the mixture of acetone (3 mL) and ethanol (3 mL) in water bath at 60°C. In the second step, the oily phase was dispersed in an aqueous phase containing a surfactant (poloxamer 188 or tween80) in different concentrations (1% or 2%) at 60°C and premixed by magnetic stirrer for 5 min at 800 rpm. The resulting preemulsion was then ultrasonicated (either at 2 or 4 min) using a probe sonicator (Baldelin, Germany) by probe TT13 in amplitude 40% to produce an o/w nanoemulsion. Finally, the obtained nanoemulsion (o/w) was cooled down at room temperature while stirring on magnetic stirrer at 800 or 1300 rpm for about 1 h [27].

2.3. Experimental Design and Analysis. Table 1 displays the six independent variables and their levels studied in a L8 orthogonal array using Taguchi design. L and subscript 8

TABLE 2: Formulations of NLCs produced by a Taguchi design in a standard orthogonal array (L8).

Code	Wt% OA	Surfactant type	Drug/lipid ratio	Surfactant conc.	Sonication time (min)	Homogenization rate (rpm)
O ₁₅ P ₁	15	Poloxamer188	5	1	2	800
O ₃₀ T ₂	30	Tween80	5	2	2	800
O ₃₀ P ₁	30	Poloxamer188	10	1	4	800
O ₁₅ P ₂	15	Poloxamer188	5	2	4	1300
O ₁₅ T ₁	15	Tween80	10	1	2	1300
O ₃₀ T ₁	30	Tween80	5	1	4	1300
O ₃₀ P ₂	30	Poloxamer188	10	2	2	1300
O ₁₅ T ₂	15	Tween80	10	2	4	800

denote the Latin square and the number of the experimental runs, respectively. A run involved the corresponding combination of levels to which the factors in the experiment were set. All experiments were performed in triplicate. Four studied responses were included: particle size, zeta potential, entrapment efficiency (EE), and drug release percent. The experimental results were then analyzed by the Design Expert software version 7 (Stat-Ease, Inc., Minneapolis, Minnesota, USA) to extract independently the main effects of these factors, followed by the analysis of variance (ANOVA) to determine which factors were statistically significant. Identifying controlling factors and qualifying the magnitude of the effects were also emphasized.

2.4. Determination of Particle Size and Zeta Potential of the Nanoparticles. Size and zeta potential of NLCs were measured by photon correlation spectroscopy (PCS, Zetasizer 3000, Malvern, UK). All samples were diluted appropriately with the aqueous phase of the formulation for the measurements. Z-Average particle size, polydispersity index, and zeta potential were measured in triplicate.

2.5. Analytical Method of PTX Detection. PTX concentration in release medium and its entrapment efficiency in nanoparticles were measured using a reversed-phase HPLC method developed and validated in our laboratory according to a previously published method with a minor modification [27]. The method was validated for linearity, accuracy, and precision. A C₁₈-Bondapak column (3.9 mm × 250 mm) was used. The mobile phase consisted of potassium dihydrogen phosphate (0.01 M)/acetonitrile (45:55) with final pH adjusted to 3.5 ± 0.1 with orthophosphoric acid. The mobile phase eluted at the flow rate of 1.5 mL/min, and the effluent was monitored at 227 nm using a UV detector. Column temperature was kept at 40°C, and 40 μL of sample was injected into the HPLC column. Data analysis and processing were performed by millennium software.

2.6. Determination of Entrapment Efficiency and Drug Loading in NLC. Following precipitation of NLCs by centrifugation, the drug content in supernatant was determined in triplicate by HPLC. The separated drug-loaded NLCs were redispersed in 0.1 wt% tween80 and surged vertically for 3 min to dissolve the adsorbed drugs on the surface of NLCs.

Then the dispersions were centrifuged at 20000 rpm for another 15 min. The drug content in the supernatant after centrifugation was measured by HPLC method. The drug entrapment efficiency (EE) and drug loading (DL) in the nanoparticles were calculated from (1)

$$EE = \left(\frac{Wa - Ws1 - Ws2}{Wa} \right) \times 100, \quad (1)$$

$$DL = \left(\frac{Wa - Ws1 - Ws2}{Wa - Ws1 - WS2 + WL} \right) \times 100,$$

where Wa is the weight of drug added in system, $Ws1$ is the analyzed weight of drug in supernatant after the first centrifugation, $Ws2$ is the analyzed weight of drug in supernatant after the second centrifugation, and WL is the weight of lipid added in system [27].

2.7. In Vitro Release of PTX from NLCs. To determine the release rate of PTX from nanoparticles, 3 mL of aqueous dispersion of each formulation was added to the dialysis bags with molecular weight cutoff of 12000 Da and the sealed bags were placed in the glass beaker in 150 mL of the phosphate buffer solution (PBS) 0.1 M, PH 7.4 containing 0.1% tween80 to provide sink condition with agitation of 200 rpm. Samples were withdrawn at predetermined time intervals up to 72 h and replaced with fresh PBS maintained at the same temperature [28]. The content of PTX in the samples was determined by the described HPLC method.

2.8. Freeze Drying of NLCs. In the preliminary trials the particles were lyophilized by using different types of cryoprotectants: PEG4000, AvicelRC591, aerosil, mannitol, sorbitol, and dextrose. Freezing temperature was -70°C for about 24 hours, and 25% (w/w) concentrations of cryoprotectants in mass were used. Operating conditions of the freeze dryer (Christ Alpha 4.2LD over, Germany) were a temperature of -40°C and a pressure of 0.4 bar. After choosing the best cryoprotectant which caused the lowest growth in particle size, subsequently optimization of various effective factors in lyophilization process of NLC of PTX was carried out and the physicochemical properties of the NLCs before and after freeze drying were checked. Redispersion of lyophilized nanoparticles is carried out using 0.01% PVA in distilled water using a sonicator bath for 10 minutes.

2.9. Atomic Force Microscopy (AFM). Observation of the morphology and particle size of the optimized NLCs before and after freeze drying was performed by an atomic force microscope (Nanosurf AG, Liestal, Switzerland). AFM images were obtained by measurement of the interaction forces between the tip and the sample surface. The experiments were done in air at room temperature (25°C) operating in contact mode. Droplets of the final suspension (20 µL) were deposited onto a small mica disk. After the drop was dried, the contact mode was used at room temperature.

2.10. Cell Culture. HT-29, the human colorectal adenocarcinoma cell lines, were obtained from Pasteur institute (Iran). Cells were grown at 37°C in humidified atmosphere containing 5% CO₂ in RPMI 1640 medium supplemented with 10% fetal bovine serum (FBS), 100 units/mL penicillin, and 100 units/mL streptomycin. For the experiments, the cells were detached by trypsin treatment, seeded at a density 4×10^4 cells/mL into 96-well culture plate (SPL Lifescience, Korea), and incubated for 24 h at 37°C in 5% CO₂ and 100% humidity before cell viability test.

2.11. In Vitro Cytotoxicity Assay. After seeding the cells on 96 well plate, each row was treated with 20 µL of different concentrations of paclitaxel solution (a 50:50 mixture of Cremophor EL and ethanol), 20 µL of PTX-loaded NLC formulation in different concentrations, 20 µL of blank NLC, 20 µL of different concentrations of PTX in DMSO, and 20 µL of culture medium (as negative control), respectively. The concentration of paclitaxel varied from 0.1 to 100 ng/mL for commercial vehicle, NLCs, and DMSO. Then the plate was incubated for 72 h, after that 20 µL MTT was added to each well, and cells were incubated for another 4 h. After removing the unreduced MTT and medium, each well was washed with 100 µL of PBS, and 180 µL of DMSO was then added to each well to dissolve the MTT formazan crystals. Immediately after pipetting, each row was separately analyzed by ELISA method. Cell viability for each sample was calculated using (2)

$$\text{Cell survival} = \frac{\text{mean of each group} - \text{mean of blank}}{\text{mean of negative control} - \text{mean of blank}} \quad (2)$$

Another experiment was performed to confirm that cytotoxicity of loaded NLC is mediated by internalization of the drug through LDL receptors. Considering that cholesterol is fitted to the LDL receptors via Apo-E protein, the cellular viability tests were carried out in the absence of Apo-E. In this experiment HT-29 viable cells were grown in RPMI 1640 medium supplemented with 100 units/mL penicillin, 100 units/mL streptomycin and without serum. After that, the cells were detached by trypsin treatment, seeded at a density 4×10^4 cells/mL into 96-well culture plate, and incubated for 24 h at 37°C in 5% CO₂ and 100% humidity. After this period, 10 ng/mL PTX, free or associated with NLC, was added to the plate in triplicate and incubated for 24 h at 37°C. The cell cytotoxicity and survival percent were evaluated by MTT assay.

3. Results and Discussion

3.1. Particle Size and Zeta Potential of NLCs. Solvent diffusion method was used for preparation of PTX-loaded NLC. The organic phase was added to the aqueous phase in the same temperature at 60°C. Hu et al. have shown that the lower temperature of dispersion medium led to the lower diffusion rate of organic dispersion phase and consequently formed the relatively large particles with wide size distribution [29]. The properties of PTX-loaded NLCs such as particle size, polydispersity index (PI), zeta potential, entrapment efficiency, and release percent are listed in Table 3.

It was found that the size of drug-loaded particles was higher than that of drug-free ones due to the incorporation of drug in NLC matrix. On the other hand, the most effective factor on particle size relates to the drug content. Changing the drug content from 5 to 10 increased the size of nanoparticles effectively.

As shown in Figure 1, the OA content and surfactant concentration had also rather high contribution to the particle size. The higher oleic acid content reduced the viscosity inside NLC, and consequently, reduced the surface tension to form smaller particles. The polydispersity index was also decreased by increasing the OA content. These results suggested that the addition of OA to the formulations was in favor of forming nanoparticles with more homogeneous size distributions due to the size reduction. In the study conducted by Hu et al., stearic acid nanostructured lipid carriers with various oleic acid content loaded by clobetasol were prepared by solvent diffusion method. In their study as OA content was increased up to 30%, the particle sizes were decreased with more regular morphology which is in agreement with our results [30]. Increasing the concentration of surfactant decreased the particle sizes of nanoparticles. Muller has shown that increasing the poloxamer concentration to 1% was effective in producing smaller size SLN composed of tripalmitin, cetyl palmitate, and glycerylmonostearate [31]. In present study, it seems that 1% poloxamer is sufficient to cover the surface of nanoparticles effectively and prevents agglomeration during the process.

Zeta potential is often a key factor to understand the stability of colloidal dispersion. As shown in Table 3 the absolute value of zeta potential in most formulation was above 10. This demonstrates that the nanoparticles dispersion obtained by solvent diffusion method in an aqueous system in this study is a physically stable system [32]. The data shown in Figure 1 reveals that the drug content is the most effective variable on zeta potential of nanoparticles. Changing drug/lipid weight ratio from level 1 to level 2 (increasing the drug percent from 5% to 10%) decreased the absolute value of zeta potential. Freitas and Muller have shown that the increased drug content could reduce the charge density and absolute values of zeta potential [33]. Our results revealed that changing the surfactant type from tween80 to poloxamer188 elevated the absolute value of the zeta potential. In the study conducted by Lim and Kim the zeta potential was decreased in the corporation of tween80

TABLE 3: Physical properties of different NLCs.

Code	Particle size (nm)	Pd index	Zeta potential (mV)	EE* %	DL** %	Drug released after 72 h
O ₁₅ P ₁	158.1 ± 17.1	0.1 ± 0.009	-20.8 ± 0.26	63 ± 13.2	3.3 ± 0.5	43.39 ± 6.8
O ₃₀ T ₂	80.68 ± 15.9	0.2 ± 0.01	-9.1 ± 0.12	72 ± 11.6	2.8 ± 0.3	53.9 ± 7.6
O ₃₀ P ₁	173.6 ± 19.8	0.3 ± 0.02	-12.7 ± 0.19	60 ± 10.3	2.8 ± 0.5	59.3 ± 5.6
O ₁₅ P ₂	132.9 ± 21.3	0.2 ± 0.04	-19.7 ± 0.23	63 ± 9.8	2.3 ± 0.4	52.23 ± 4.3
O ₁₅ T ₁	189.4 ± 15.6	0.6 ± 0.02	-9.17 ± 0.15	46 ± 10.2	2.1 ± 0.2	50.5 ± 8.5
O ₃₀ T ₁	100.9 ± 12.3	0.3 ± 0.01	-12.9 ± 0.15	62 ± 11.6	3.5 ± 0.2	50.23 ± 6.3
O ₃₀ P ₂	137.3 ± 13.4	0.1 ± 0.03	-8.8 ± 0.13	53 ± 8.6	2.9 ± 0.5	70.3 ± 5.4
O ₁₅ T ₂	169.8 ± 10.8	0.4 ± 0.04	-10.7 ± 0.09	53 ± 7.3	3.1 ± 0.6	63.78 ± 8.1

*EE: entrapment efficiency. **DL: drug loading.

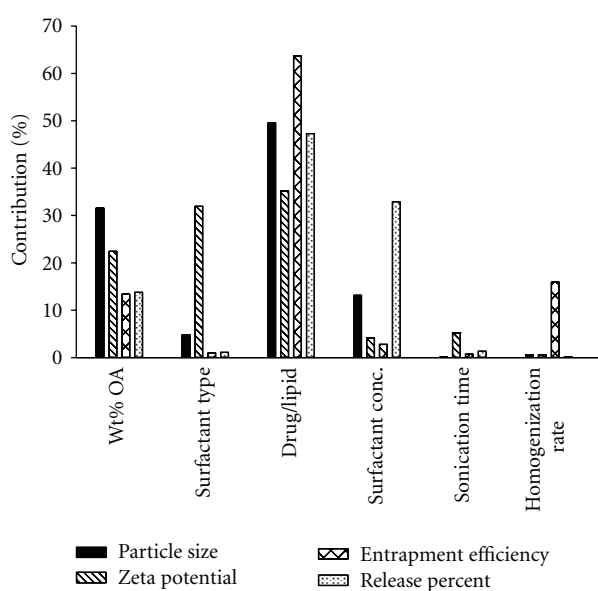


FIGURE 1: Contribution percent of different effective factors on the particle size, zeta potential, entrapment efficiency, and release percent of NLCs loaded with PTX.

as surfactant [34]. The results of Table 3 and data analysis showed that absolute zeta potential decreased as emulsifier concentration increased to 2% which was in accordance with the results of other researchers [35]. Data analysis showed that increasing the amount of OA could decrease the absolute value of zeta potential. In preparation of clobetasol NLCs with various amount of oleic acid, no trend was found for zeta potential changes by increasing the OA content of nanoparticles [30]. In fact crystalline reorientation or recrystallization of lipid can result in changes on the particle surface and subsequently change the zeta potential unpredictably.

3.2. Entrapment Efficiency in NLC. The calibration curve of HPLC method used for determination of drug content and drug release studies was linear in the concentration range 0.05–2 µg/mL ($r^2 = 0.999$). The inter- and intraday precision and accuracy were less than 10.27% with the

detection limit 20 ng/mL. As Figure 1 shows, drug to lipid weight ratio is the most effective factor on entrapment efficiency in NLC. Changing the drug/lipid weight ratio from 10% to 5%, decreasing the amount of drug to lipid, accompanied good entrapment of drug in the lipids. The OA content were also influenced loading and entrapment efficiency. The drug entrapment efficiency was increased, by increasing the percentage of OA. Previous studies have illustrated that incorporation of liquid lipids to solid lipids can lead to massive crystal order disturbances. This results in great imperfections in the crystal lattice, which in turn leaves enough space to accommodate drug molecules, which ultimately improves drug loading capacity and drug entrapment efficiency [36]. As shown in Figure 1, other factors were not effective on the drug loading.

3.3. In Vitro Release of PTX from NLC. Figure 1 shows that the drug release from NLCs is more affected by drug/lipid ratio and the surfactant concentration. The release rate became faster when the amount of OA was increased. Surfactant type, sonication time, and homogenization rate did not significantly affect the release rate. The drug release profiles from NLCs are shown in Figure 2. Drug-to-lipid weight ratio could influence the release of PTX from nanoparticles. When the drug increased from 5 to 10%, most of the drug located at the outer shell of nanoparticles which led to faster drug release. For all formulations, a biphasic drug release pattern was observed, which is due to the burst release at the initial stage and is followed by sustained release in the later times. The release rate in initial stage became faster with increasing the OA content. On the other hand, when the OA content increased from 15 to 30%, the particle size decreased; consequently, the specific surface area was increased, and the faster release rate was observed. Changing the surfactant concentration from level1 to 2 also increased the drug release rate.

3.4. Optimization of PTX-NLCs. Computer optimization process and a desirability function determined the effect of the levels of independent variables on the responses. All responses were fitted to the linear model. The constraints of particle size were 80.68 to 189.4 nm with targeting the particle size in the range of 100–189, for zeta potential was

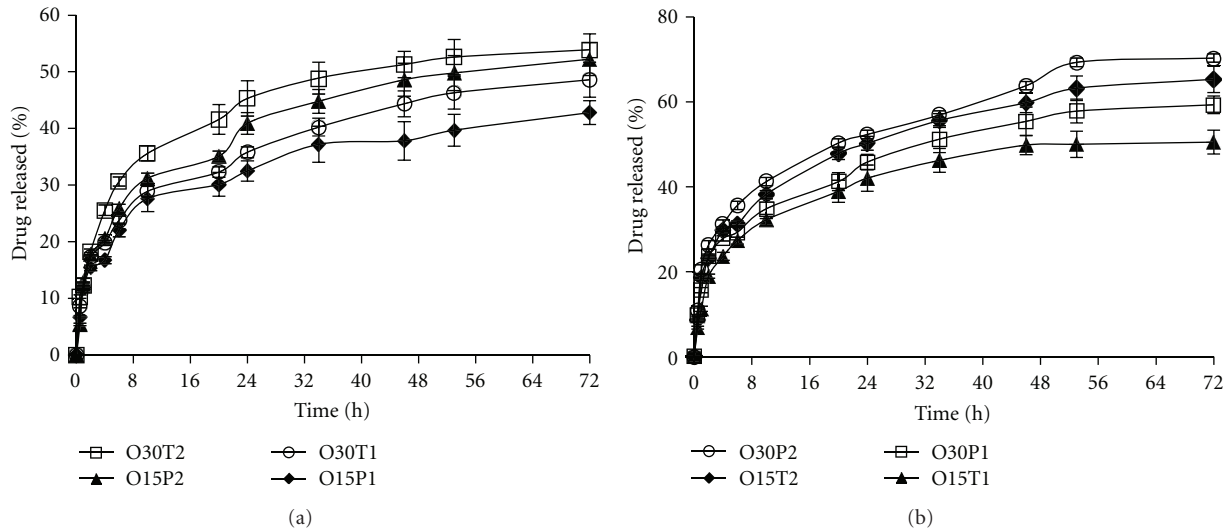


FIGURE 2: *In vitro* release profile of paclitaxel from cholesterol NLCs ($n = 3$): (a) drug/lipid 5% w/w, (b) drug/lipid 10% w/w.

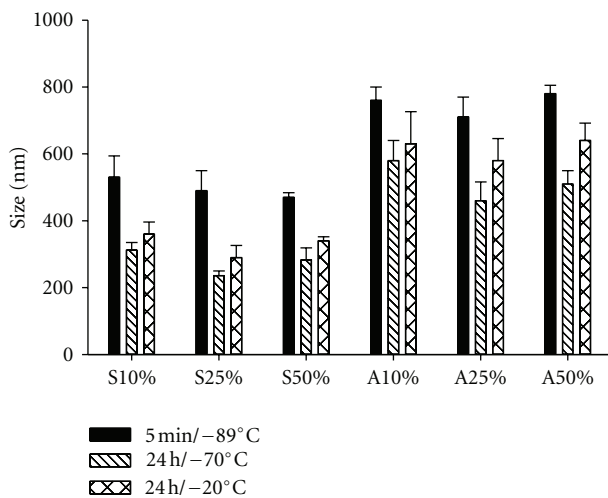


FIGURE 3: Effect of different cryoprotectants, concentration, and freezing rate on particle size. Sublimation time did not have significant effect on particle size. S: Sorbitol, A: Aerosil.

−8.8 to −20.8 mV, while the target was maximum absolute value of zeta potential, for the EE the constraint was 46 to 72% with the goal of maximum value, and for release percent the target was considered in the range of the measured value.

Accordingly, the predicted optimized formulation by the software would contain 5% PTX, 30% OA, 1% poloxamer188, 2 minute sonication, and 800 rpm homogenization rate. To confirm the predicted model, the optimized formulation was prepared, and the observed responses were measured and listed in Table 4. The acceptable agreement between the observed values and the values predicted by the software and the negligible error percent confirm the validation and reliability of our method as well as its adequate

TABLE 4: Predicted versus actual responses obtained for the optimized formulation.

Responses	Particle size (nm)	Zeta potential (mV)	Release after 72 h	EE (h)
Actual values	181.6 ± 14.8	−12.9 ± 0.2	42.3 ± 3.6	53 ± 4.2
Predicted values	142.33	−12.33	50	59
Error (%)	21.54	4.41	18.77	11.32

TABLE 5: Results of a preliminary screening of different cryoprotectants.

Cryoprotectant	Particle size (nm)	Zeta potential (mV)
PEG4000	1550 ± 296.3	−4.5 ± 0.3
Avicel RC591	956 ± 120.6	−6.9 ± 0.9
Mannitol	1056 ± 213.6	−2.8 ± 0.1
Dextrose	857 ± 87.6	−4.3 ± 0.4
Sorbitol	216 ± 21.2	−10.6 ± 0.7
Aerosil	480 ± 83.2	−15.6 ± 0.3

precision for the prediction of optimized conditions in the domain of levels chosen for the independent variables.

3.5. Freeze Drying of NLCs. As mentioned, lyophilization is an approach to improve the physical and chemical stability of colloidal system. The results of the preliminary screening study of different cryoprotectants listed in Table 5 show that PEG4000, Avicel, and dextrose cause an increase in size to about 1 microns and zeta potential to about −5 μm suggesting an aggregation of particles, leading to poor redispersibility. In a work conducted by varshosaz et al., PEG as cryoprotectant caused a significant increase in size and zeta potential [32].

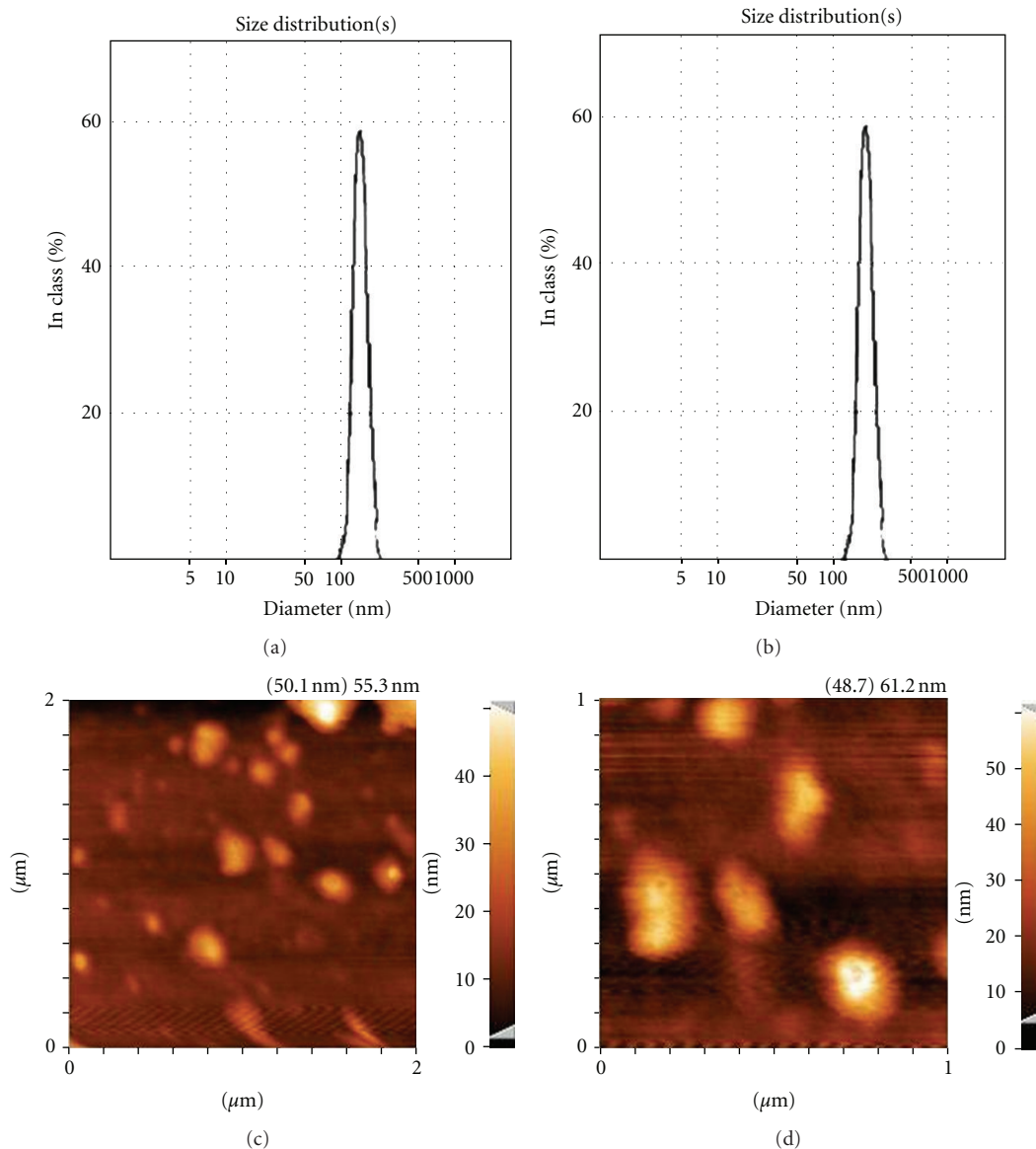


FIGURE 4: size distribution and AFM images of NLCs of PTX (a) size distribution of NLCs before freeze drying, (b) size distribution of NLCs after freeze drying, (c) AFM image of NLCs before freeze drying, and (d) AFM image of NLCs after freeze drying.

Mannitol also showed poor redispersibility with particle size greater than 1 micron which may be related to crystallization of mannitol in low temperature. Moreover, the growing crystals of water and mannitol may exert mechanical forces on the nanoparticles leading to their fusion. Table 5 shows that sorbitol and aerosil cause less increase in particle size and zeta potential after redispersion of dried nanoparticles in distilled water. However, to optimize the lyophilization process the effect of concentration and freezing rate should be considered. In the literature, different freezing methods have been used to freeze nanoparticle suspensions. In this study we used liquid nitrogen freezing ($-89^{\circ}\text{C}/5\text{ min}$) and loading vials onto precooled shelves ($-70^{\circ}\text{C}/24\text{ h}$, $-20^{\circ}\text{C}/24\text{ h}$).

The results showed an increase in the particle size of NLCs using rapid freezing rate for all the tested formulations.

However, some studies have shown that high super cooling leads to the formation of small ice crystals and may decrease the mechanical stress on nanoparticles avoiding their aggregations. Our results may be explained by the fact that quick freezing in liquid nitrogen destabilized the nanoparticles leading to a greater formation of aggregates after redispersion, so slower freezing at -70°C in deep freezer proved to be better method for this formulation. In the study conducted by Saez et al., sorbitol was found to be an effective cryoprotectant when PLGA nanoparticles were frozen at -70°C [37]. We also investigated the effect of cryoprotectant concentrations in three levels (10, 25, and 50% w/w). As shown in Figure 3, it seems that sorbitol was better than aerosil in reducing particle size. Sorbitol in 25% w/w concentration may arise from the formation

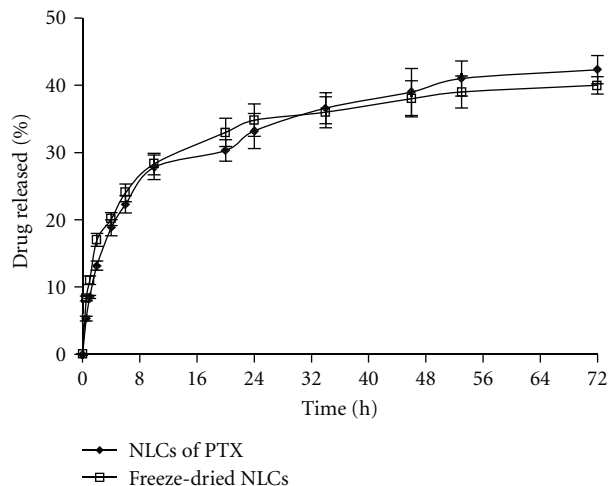


FIGURE 5: Release profiles of PTX from NLCs before and after freeze drying.

of a protective capping layer around the NLCs. The zeta potential range for all preparation was low, with the range -9.8 up to -15.5 mv. This may be related to the effect of PVA. PVA is a polymer with long-chain alkyl which causes a negative charge. Redispersion of lyophilized formulations in 0.01% PVA reduces the zeta potential and improves dispersion. Our results also revealed that aerosil causes more decrease in zeta potential than sorbitol. Perhaps because the suspension of aerosil has negative zeta potential and increases the absolute zeta potential of nanoparticles, while sorbitol is a natural compound that dissolves in water.

Based on our results, the optimum condition is obtained using sorbitol 25% w/w concentration, freezing rate of $-70^{\circ}\text{C}/24$ h, and 48 h sublimation time. To confirm the data of particle size, the AFM photographs and size distributions of the nanoparticles prior and after freeze drying by using 25% sorbitol were also shown in Figure 4. Optimized freeze drying condition maintained the particle size of NLCs of PTX after redispersion. The AFM images of the nanoparticles revealed spherical and round shape of approximately 150–200 nm in diameter, which was similar to the results obtained by photon correlation spectroscopy. The results of loading percent and 3 days drug release study on optimized formulation after redispersion showed 42% drug loading and 40% drug release from nanoparticles. As shown in Figure 5 there is no significant change in the burst effect and drug release content from NLCs before and after lyophilization.

3.6. *In Vitro* Cytotoxicity. Figure 6 shows the cytotoxic activity curves of the optimized NLC-PTX formulation, PTX solubilized in DMSO, PTX in Cremophor EL, and blank NLC. The blank NLCs did not show significant cytotoxicity with more than 80% of HT-29 cells survived after 72 h exposure to the highest concentration of blank NLCs.

At low concentration (0.1 ng/mL), only free PTX in DMSO and Cr EL was effective to suppress the cell growth, while PTX loaded-NLCs displayed no cytotoxicity, which may be attributed to the relatively low amount of drug

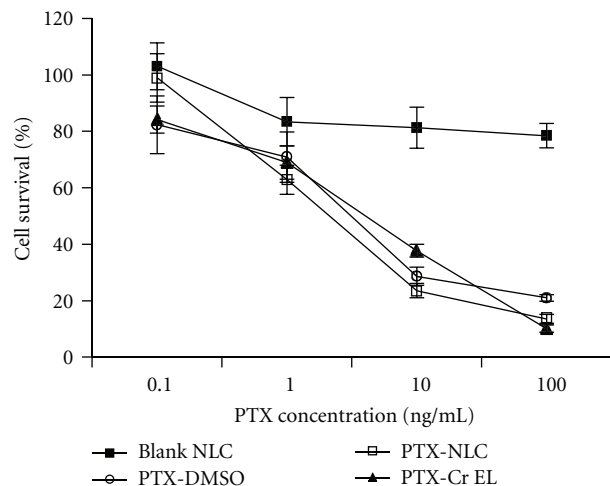


FIGURE 6: *In vitro* cytotoxicity of various PTX formulations and blank NLC against HT-29 cell line after 72 h incubation. Data were plotted as the mean \pm SD of three measurements.

TABLE 6: IC_{50} values of PTX solutions and the drug-loaded NLC against HT-29 cell lines.

Drug formulation	IC_{50} (mean \pm SD)		
	24 h	48 h	72 h
PTX in cremophor EL	15.81 \pm 3.12	10.23 \pm 1.56	8.32 \pm 1.35
PTX-NLC	18.93 \pm 2.56	11.24 \pm 2.34	5.24 \pm 0.96
PTX in DMSO	13.31 \pm 4.12	8.93 \pm 3.56	6.91 \pm 0.85

released from the carriers. At high concentrations (1–100 ng/mL) PTX-loaded NLCs also showed decrease in cell growth, which was comparable to free PTX. Thus our finding demonstrated that PTX-NLC developed in this study had the potency similar to that of Cremophor-EL-based formulation and could be a safe drug carrier. The amount of PTX required to achieve the IC_{50} values were evaluated after 24, 48, and 72 h exposure of cells to the free PTX and PTX-loaded NLCs. As shown in Table 6 the cytotoxicity of PTX was time dependent.

Survival of HT-29 cultured in the absence of Apo E was considerably increased by incubation with NLC-PTX. On the other hand, free drug cytotoxicity was much less affected by the change in growth medium (Figure 7). It is concluded that the drug associated with cholesterol lipid base is uptook into the cancer cells by endocytosis via LDL receptors, and when Apo E is removed from the serum in the medium of cell culture the targeting to the LDL receptors is blocked and cell viability is increased. The unassociated drug could freely cross the cellular membrane and exert its cytotoxicity. As expected the cytotoxicity of free drug was unaffected by the absence of Apo E from culture medium. Hence, the optimized NLCs developed in our study could be an efficient vehicle for delivery of PTX to the intended site without provoking any side effect associated with cremophor EL containing formulations. The drug content from these lipidic nanoparticles is largely released inside the cancer

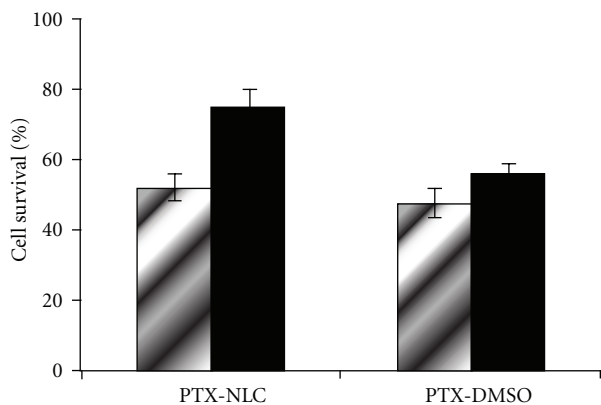


FIGURE 7: Cytotoxicity of PTX-loaded NLC and free PTX in the presence (grey columns) or absence (black columns) of Apo E after 24 h incubation.

cells resulting in an enhanced efficiency and reducing side effects.

4. Conclusion

In the present study the PTX-loaded NLCs were prepared using solvent diffusion method following probe sonication and finally freeze dried under certain conditions which were evaluated by different factors. Optimized formulation containing 5% PTX, 30% OA, 1% poloxamer188, 2 minute sonication, and 800 rpm homogenization rate gave nanoparticles with about 181.6 nm with 0.1 polydispersity, -12.9 Mv zeta potential, 43% drug release after 3 days and 53% entrapment efficiency. The optimum condition in freeze drying was achieved by using sorbitol in 25% w/w, freezing rate of $-70/24$, and sublimation time 48 h. Freeze-dried NLCs suspended in PVA 0.01% solution still were spherical with the mean diameter about 200 nm and entrapment efficiency 42%. cytotoxicity results showed that PTX associated with NLCs is also effective and exerts the pharmacologic effect by entering the cell through the LDL receptor endocytic pathway. Thus, the optimized NLCs developed in our study could deliver PTX selectively to the cancer cells without any side effect associated with cremophor EL containing formulations. These nanoparticles are, therefore, anticipated to be a promising PTX carrier for their targeted and intracellular delivery.

References

- [1] A. W. G. Alani, Y. Bae, D. A. Rao, and G. S. Kwon, "Polymeric micelles for the pH-dependent controlled, continuous low dose release of paclitaxel," *Biomaterials*, vol. 31, no. 7, pp. 1765–1772, 2010.
- [2] J. H. Kim, Y. S. Kim, S. Kim et al., "Hydrophobically modified glycol chitosan nanoparticles as carriers for paclitaxel," *Journal of Controlled Release*, vol. 111, no. 1-2, pp. 228–234, 2006.
- [3] A. O. Nornoo, D. W. Osborne, and D. S. L. Chow, "Cremophor-free intravenous microemulsions for paclitaxel. I: formulation, cytotoxicity and hemolysis," *International Journal of Pharmaceutics*, vol. 349, no. 1-2, pp. 108–116, 2008.
- [4] G. J. Fetterly and R. M. Straubinger, "Pharmacokinetics of paclitaxel-containing liposomes in rats," *AAPS PharmSci*, vol. 5, no. 4, pp. 90–100, 2003.
- [5] M. J. Hawkins, P. Soon-Shiong, and N. Desai, "Protein nanoparticles as drug carriers in clinical medicine," *Advanced Drug Delivery Reviews*, vol. 60, no. 8, pp. 876–885, 2008.
- [6] F. Danhier, N. Lecouturier, B. Vroman et al., "Paclitaxel-loaded PEGylated PLGA-based nanoparticles: in vitro and in vivo evaluation," *Journal of Controlled Release*, vol. 133, no. 1, pp. 11–17, 2009.
- [7] F. Lacoëuille, F. Hindre, F. Moal et al., "In vivo evaluation of lipid nanocapsules as a promising colloidal carrier for paclitaxel," *International Journal of Pharmaceutics*, vol. 344, no. 1-2, pp. 143–149, 2007.
- [8] U. S. Sharma, S. V. Balasubbanian, and R. M. Straubinger, "Pharmaceutical and physical properties of paclitaxel (Taxol) complexes with cyclodextrins," *Journal of Pharmaceutical Sciences*, vol. 84, no. 10, pp. 1223–1230, 1995.
- [9] B. Elsadek, R. Graeser, N. Esser et al., "Development of a novel prodrug of paclitaxel that is cleaved by prostate-specific antigen: an in vitro and in vivo evaluation study," *European Journal of Cancer*, vol. 46, no. 18, pp. 3434–3444, 2010.
- [10] X. Zhang, J. K. Jackson, and H. M. Burt, "Development of amphiphilic diblock copolymers as micellar carriers of taxol," *International Journal of Pharmaceutics*, vol. 132, no. 1-2, pp. 195–206, 1996.
- [11] S. C. Kim, D. W. Kim, Y. H. Shim et al., "In vivo evaluation of polymeric micellar paclitaxel formulation: toxicity and efficacy," *Journal of Controlled Release*, vol. 72, no. 1-3, pp. 191–202, 2001.
- [12] T. Hamaguchi, Y. Matsumura, M. Suzuki et al., "NK105, a paclitaxel-incorporating micellar nanoparticle formulation, can extend in vivo antitumor activity and reduce the neurotoxicity of paclitaxel," *British Journal of Cancer*, vol. 92, no. 7, pp. 1240–1246, 2005.
- [13] C. Zhang, P. Qineng, and H. Zhang, "Self-assembly and characterization of paclitaxel-loaded N-octyl-O-sulfate chitosan micellar system," *Colloids and Surfaces B*, vol. 39, no. 1-2, pp. 69–75, 2004.
- [14] F. Q. Hu, G. F. Ren, H. Yuan, Y. Z. Du, and S. Zeng, "Shell cross-linked stearic acid grafted chitosan oligosaccharide self-aggregated micelles for controlled release of paclitaxel," *Colloids and Surfaces B*, vol. 50, no. 2, pp. 97–103, 2006.
- [15] M. Huo, Y. Zhang, J. Zhou, A. Zou, and J. Li, "Formation, microstructure, biodistribution and absence of toxicity of polymeric micelles formed by N-octyl-N,O-carboxymethyl chitosan," *Carbohydrate Polymers*, vol. 83, no. 4, pp. 1959–1969, 2011.
- [16] R. H. Müller, K. Mäder, and S. Gohla, "Solid lipid nanoparticles (SLN) for controlled drug delivery—a review of the state of the art," *European Journal of Pharmaceutics and Biopharmaceutics*, vol. 50, no. 1, pp. 161–177, 2000.
- [17] R. H. Müller, M. Radtke, and S. A. Wissing, "Nanostructured lipid matrices for improved microencapsulation of drugs," *International Journal of Pharmaceutics*, vol. 242, no. 1-2, pp. 121–128, 2002.
- [18] K. V. Pinheiro, V. T. M. Hungria, E. S. Ficker, C. J. Valduga, C. H. Mesquita, and R. C. Maranhão, "Plasma kinetics of a cholesterol-rich microemulsion (LDE) in patients with Hodgkin's and non-Hodgkin's lymphoma and a preliminary study on the toxicity of etoposide associated with LDE," *Cancer Chemotherapy and Pharmacology*, vol. 57, no. 5, pp. 624–630, 2006.

- [19] R. C. Maranh, S. R. Graziani, and N. Yamaguchi, "Association of carmustine with a lipid emulsion: in vitro, in vivo and preliminary studies in cancer patients," *Cancer Chemotherapy and Pharmacology*, vol. 49, pp. 487–498, 2002.
- [20] C. J. Valduga, D. C. Fernandes, A. C. Lo Prete, C. H. M. Azevedo, D. G. Rodrigues, and R. C. Maranhão, "Use of a cholesterol-rich microemulsion that binds to low-density lipoproteins receptors as vehicle for etoposide," *Journal of Pharmacy and Pharmacology*, vol. 55, no. 12, pp. 1615–1622, 2003.
- [21] D. G. Rodrigues, D. A. Maria, D. C. Fernandes et al., "Improvement of paclitaxel therapeutic index by derivatization and association to a cholesterol-rich microemulsion: in vitro and in vivo studies," *Cancer Chemotherapy and Pharmacology*, vol. 55, no. 6, pp. 565–576, 2005.
- [22] N. Nishiyama and K. Kataoka, "Current state, achievements, and future prospects of polymeric micelles as nanocarriers for drug and gene delivery," *Pharmacology and Therapeutics*, vol. 112, no. 3, pp. 630–648, 2006.
- [23] L. Serpe, M. G. Catalano, R. Cavalli et al., "Cytotoxicity of anticancer drugs incorporated in solid lipid nanoparticles on HT-29 colorectal cancer cell line," *European Journal of Pharmaceutics and Biopharmaceutics*, vol. 58, no. 3, pp. 673–680, 2004.
- [24] X. G. Zhang, J. Miao, Y. Q. Dai, Y. Z. Du, H. Yuan, and F. Q. Hu, "Reversal activity of nanostructured lipid carriers loading cytotoxic drug in multi-drug resistant cancer cells," *International Journal of Pharmaceutics*, vol. 361, no. 1–2, pp. 239–244, 2008.
- [25] M. K. Lee, S. J. Lim, and C. K. Kim, "Preparation, characterization and in vitro cytotoxicity of paclitaxel-loaded sterically stabilized solid lipid nanoparticles," *Biomaterials*, vol. 28, no. 12, pp. 2137–2146, 2007.
- [26] R. Li, J. S. Eun, and M. K. Lee, "Pharmacokinetics and biodistribution of paclitaxel loaded in pegylated solid lipid nanoparticles after intravenous administration," *Archives of Pharmacol Research*, vol. 34, no. 2, pp. 331–337, 2011.
- [27] H. Yuan, J. Miao, Y. Z. Du, J. You, F. Q. Hu, and S. Zeng, "Cellular uptake of solid lipid nanoparticles and cytotoxicity of encapsulated paclitaxel in A549 cancer cells," *International Journal of Pharmaceutics*, vol. 348, no. 1–2, pp. 137–145, 2008.
- [28] D. Liu, Z. Liu, L. Wang, C. Zhang, and N. Zhang, "Nanostructured lipid carriers as novel carrier for parenteral delivery of docetaxel," *Colloids and Surfaces B*, vol. 85, no. 2, pp. 262–269, 2011.
- [29] F. Q. Hu, Y. Zhang, Y. Z. Du, and H. Yuan, "Nimodipine loaded lipid nanospheres prepared by solvent diffusion method in a drug saturated aqueous system," *International Journal of Pharmaceutics*, vol. 348, no. 1–2, pp. 146–152, 2008.
- [30] F. Q. Hu, S. P. Jiang, Y. Z. Du, H. Yuan, Y. Q. Ye, and S. Zeng, "Preparation and characterization of stearic acid nanostructured lipid carriers by solvent diffusion method in an aqueous system," *Colloids and Surfaces B*, vol. 45, no. 3–4, pp. 167–173, 2005.
- [31] R. H. Müller, M. Radtke, and S. A. Wissing, "Solid lipid nanoparticles (SLN) and nanostructured lipid carriers (NLC) in cosmetic and dermatological preparations," *Advanced Drug Delivery Reviews*, vol. 54, pp. S131–S155, 2002.
- [32] J. Varshosaz, S. Eskandari, and M. Tabbakhian, "Freeze-drying of nanostructure lipid carriers by different carbohydrate polymers used as cryoprotectants," *Carbohydrate Polymer*, vol. 88, pp. 1157–1163, 2012.
- [33] C. Freitas and R. H. Müller, "Effect of light and temperature on zeta potential and physical stability in solid lipid nanoparticle (SLN) dispersions," *International Journal of Pharmaceutics*, vol. 168, no. 2, pp. 221–229, 1998.
- [34] S. J. Lim and C. K. Kim, "Formulation parameters determining the physicochemical characteristics of solid lipid nanoparticles loaded with all-trans retinoic acid," *International Journal of Pharmaceutics*, vol. 243, no. 1–2, pp. 135–146, 2002.
- [35] V. C. F. Mosqueira, P. Legrand, J. L. Morgat et al., "Biodistribution of long-circulating PEG-grafted nanocapsules in mice: effects of PEG chain length and density," *Pharmaceutical Research*, vol. 18, no. 10, pp. 1411–1419, 2001.
- [36] E. B. Souto, S. A. Wissing, C. M. Barbosa, and R. H. Müller, "Development of a controlled release formulation based on SLN and NLC for topical clotrimazole delivery," *International Journal of Pharmaceutics*, vol. 278, no. 1, pp. 71–77, 2004.
- [37] A. Saez, M. Guzmán, J. Molpeceres, and M. R. Aberturas, "Freeze-drying of polycaprolactone and poly(D,L-lactiglycolic) nanoparticles induce minor particle size changes affecting the oral pharmacokinetics of loaded drugs," *European Journal of Pharmaceutics and Biopharmaceutics*, vol. 50, no. 3, pp. 379–387, 2000.

Research Article

Single-Molecule Sandwich Immunoassay for Quantification of Alpha-Fetoprotein Based on Evanescent Field-Enhanced Fluorescence Imaging

Seungah Lee and Seong Ho Kang

Department of Applied Chemistry, College of Applied Science, Kyung Hee University, Gyeonggi-do, Yongin-si 446-701, Republic of Korea

Correspondence should be addressed to Seong Ho Kang, shkang@khu.ac.kr

Received 2 October 2012; Accepted 7 November 2012

Academic Editor: Haiyan Li

Copyright © 2012 S. Lee and S. H. Kang. This is an open access article distributed under the Creative Commons Attribution License, which permits unrestricted use, distribution, and reproduction in any medium, provided the original work is properly cited.

A highly sensitive immunosensor based on a gold nanopatterned chip was developed for accurate determination of alpha-fetoprotein (AFP) *via* total internal reflection fluorescence microscopy (TIRFM). The surface of the gold nanopatterned chips was modified with dithiobis(succinimidyl propionate) and protein A/G for immobilization of the AFP antibody. The immunoassay created a sandwich of antigen between the AFP antibody on the chip that was modified with protein A/G, and the secondary antibody, a monoclonal anti-human-AFP labeled with biotin (biotin-labeled anti-AFP). AFP concentration was determined based on evanescent field fluorescence signal, which was generated by interaction between biotin-labeled anti-AFP and a streptavidin-labeled fluorescence dye. AFP concentration could be measured in a wide dynamic linear range of 720 zM–10 nM with a detection limit of 720 zM. A significant enhanced sensitivity (~40,000-fold) was achieved with the AFP-nanoarray chip compared to conventional chemiluminescence immunosensors. The immunoassay exhibited a wide detection range and high sensitivity and accuracy, qualities valuable for clinical assay of AFP.

1. Introduction

Since the introduction of sandwich assays using monoclonal antibodies, various immunoassays have been introduced with automated analysis and increased specificity [1]. However, many immunoassay methods such as enzyme-linked immunosorbent assay (ELISA), radioimmunoassay (RIA), and single radial immunodiffusion have disadvantages such as being time-consuming procedures using expensive instrumentation with complicated separation and labeling steps, and potential dangers (e.g., radiation hazards) or expensive materials [2]. New techniques such as electrochemistry [3], chemiluminescence [4], piezoelectricity [5], surface plasmon resonance (SPR) [6], and sandwich immunoassays based on nanoarray protein chips [7, 8] have attracted interests because of their characteristics. Specifically, nanoarray protein chips offer a sensitive, accurate, quantitative, and

simple alternative methodology for determination of tumor markers.

Alpha-fetoprotein (AFP) is a 70 kDa oncofetal glycoprotein of 591 amino acids. It contains a single asparagine-linked (Asn233) carbohydrate chain that is a known biomarker for hepatocellular carcinoma (HCC) [9–12]. The association between serum AFP and HCC has been extensively described [13–16]. AFP has been a diagnostic test for HCC since the 1970s, when most patients with HCC were diagnosed at an advanced stage with clinical symptoms [17]. AFP is suggested to function as a transport molecule for several different ligands and various drugs [18, 19] and to have immunosuppressive activity and a role in regulation of cell proliferation [20]. The first conditionally quantitative serum assays for AFP were introduced in 1971 [21]. Several approaches have attempted to enhance the techniques of SPR detection [22] such as bioluminescent sandwich

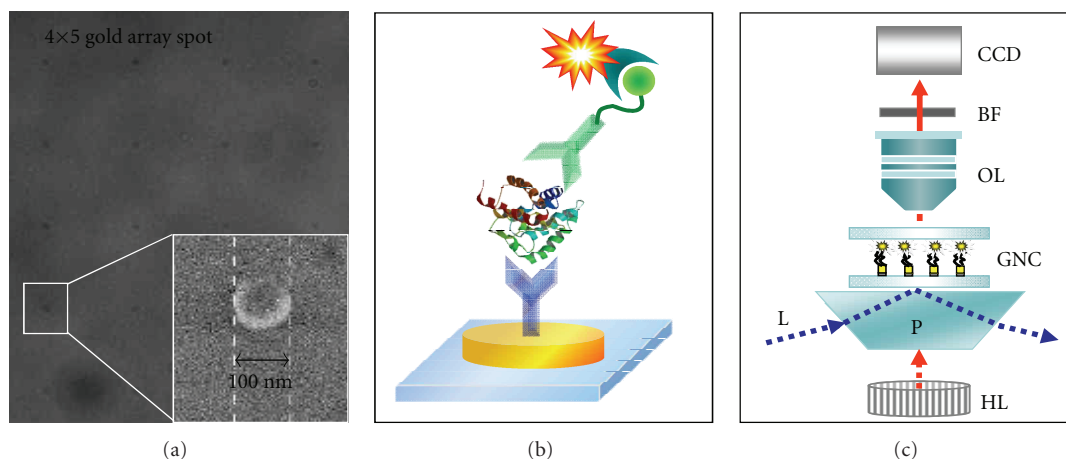


FIGURE 1: (a) DIC image of gold nanopatterned AFP chip with a spot diameter of 100 nm and (inner) SEM image of individual gold spots. (b) Schematic diagram of the AFP sandwich fluorescence immunoassay. (c) Schematic diagram showing the TIRFM detection system. L: laser; HL: halogen lamp; P: transmitted all-side polished dove-type prism; GNC: gold nanopatterned chip; OL: objective lens; BF: band-pass filter; C: charge-coupled device.

immunoassays [23], electrochemical immunoassays [24], and chemiluminescence resonance energy transfer [25]. However, the sensitivities for these assays are still poor [26].

In this study, a sandwich immunoassay using gold nanopatterned protein chips was developed for quantitative detection of tumor markers such as AFP in serum. A total internal reflection fluorescence microscopy (TIRFM) technique based on evanescent field fluorescence imaging was applied for trace analysis of AFP with a wide dynamic linear range to use in clinical diagnosis. The relationship between evanescent field-fluorescence signal and AFP concentration showed excellent and extensive linearity. The method was successfully applied to determine AFP in human serum.

2. Experimental Details

2.1. Reagent Preparation. Dimethyl sulfoxide (DMSO) and glycine were from Sigma-Aldrich Inc. (St. Louis, MO, USA). Dithiobis(succinimidyl propionate) (DSP) and protein A/G were from Pierce (Rockford, IL, USA). Tris (base) was from Mallinckrodt Baker, Inc. (Phillipsburg, NJ, USA). StabilGuard was from SurModics (Eden Prairie, MN, USA). Alexa Fluor 488 streptavidin was obtained from Molecular Probes (Eugene, OR, USA). Human AFP antigen, monoclonal antibody to human AFP (5H7), and monoclonal antibody to human AFP labeled with biotin (biotin-labeled anti-AFP, 4A3), were from BiotDesign International (ME, USA). Normal human serum samples were isolated from blood by centrifugation at 2,000 rpm for 15 min at 2°C. To mimic clinical conditions, a standard AFP sample of 20 fM was spiked into $1:10^4$ diluted normal human serum at a three-to-one ratio. Before use, $1\times$ PBS buffer solution (pH 7.4; 137 mM NaCl, 2.7 mM KCl, 4.3 mM Na_2HPO_4 , 1.4 mM KH_2PO_4) was filtered through a 0.2- μm membrane filter and photobleached overnight using a UV-B lamp (G15TE, 280–315 nm, Philips, The Netherlands).

2.2. Gold Nanopatterned Chips. A gold nanopatterned substrate was designed as shown in Figure 1(a) and fabricated by the National Nanofab Center (Daejeon, Republic of Korea). Four-inch soda-lime glass wafers from Winwin Tech (Bucheon, Republic of Korea) were used to make 4×5 nanoarrays with 100 nm diameter spots (SEM in Figure 1(a)) with a $10\ \mu\text{m}$ pitch. Gold spots were deposited on the glass substrate by an electron beam evaporator. Substrates were coated with a 5 nm adhesive layer of chromium (99.997% purity) at a rate of 0.1 nm/s, followed by deposition of a 20 nm layer of gold (99.997% purity) at a rate of 0.1 nm/s. Before linker deposition, chips were immersed in acetone (99.5% purity) for 30 s, followed by isopropyl alcohol (99.9% purity) for 30 s. Gold nanopatterned chips were exposed to piranha solution (1:1 = H_2SO_4 :30% H_2O_2) for 30 min, rinsed with deionized water, and dried under a stream of nitrogen. Before use, chips were stored in a desiccator.

2.3. AFP Single-Molecule Sandwich Immunoassay on Gold Nanopatterned Chips. The analytical procedure for sandwich immunoassay of AFP on a gold substrate is schematically depicted in Figure 1(b). Gold patterned chips were immersed in 4 mg/mL DSP in DMSO for 30 min, then rinsed with DMSO and deionized water. Addition of 0.1 mg/mL of protein A/G, which binds to the heavy chains of the antibody Fc region, was used to uniformly orient the antibodies for 1 h. Unreacted succinimide groups were blocked with 10 mM Tris (pH 7.5) and 1 M glycine for 30 min. Chips were incubated with StabilGuard for 30 min to stabilize bound proteins, then rinsed briefly with a few drops of deionized water. Chips were incubated with 20 μL of 2 $\mu\text{g}/\text{mL}$ monoclonal antibody to human AFP (5H7) in PBS (pH 7.4) for 1 h. After washing, AFP standard protein that was diluted to various concentrations, or normal or spiked clinical samples were incubated on chips for 1 h. The incubation time of the sample with 720 zM AFP was increased to 5 h to allow sufficient time for Brownian motion. Reaction with

TABLE 1: Comparison of detection limits between AFP-nanoarray chips and other methods.

Method	Dynamic range (ng/mL)	LOD (ng/mL)	References
SPR	1.0–200 (14 pM–2.8 nM)	0.65 (9.1 pM)	[22]
BL immunoassay I	0.01–100 (140 fM–1.4 nM)	0.01 (140 fM)	[23]
BL immunoassay II	0.02–200 (280 fM–2.8 nM)	0.02 (280 fM)	[28, 29]
CRET	5–70 (70 pM–980 pM)	2.50 (35 pM)	[25]
FRET inhibition assay	0.8–45 (11.2 pM–0.63 nM)	0.41 (5.74 pM)	[30]
Pz immunoassay	20–640 (280 pM–8.96 nM)	20 (280 pM)	[31]
EC immunoassay I	0.5–80 (7 pM–1.12 nM)	0.25 (3.5 pM)	[32]
EC immunoassay II	0.1–30 (1.4 pM–420 pM)	0.018 (252 fM)	[33]
EC immunoassay III	0.01–200 (140 fM–2.8 nM)	0.004 (56 fM)	[34]
EC immunoassay IV	1.0–10 (14 pM–140 pM)	0.70 (9.8 pM)	[35]
ECL immunoassay	0.002–32 (28 fM–448 pM)	0.002 (28 fM)	[36]
CL immunoassay	0.01–0.5 (140 fM–7 pM)	0.005 (70 fM)	[37]
AFP-nanoarray chip	50×10^{-9} –714.3 (720 zM–10 nM)	50×10^{-9} (720 zM)	This work

Indication: SPR: surface plasmon resonance; BL: bioluminescent; CRET: chemiluminescence resonance energy transfer; FRET: fluorescence resonance energy transfer; Pz: piezoelectric; EC: electrochemical; ECL: electrogenerated chemiluminescence; CL: chemiluminescence; LOD: limit of detection.

20 μ L of 2 μ g/mL biotin-labeled anti-AFP (4A3) was for 1 h. To detect biotin-labeled anti-AFP, 20 μ L of Alexa Fluor 488 streptavidin (2 μ g/mL) was added to chips and incubated for 30 min. Chips were washed in 100 mL $1 \times$ PBS for 2 min and rinsed briefly with deionized water at each step. All reactions were carried out at room temperature with agitation.

2.4. Total Internal Reflection Microscopic System. A schematic diagram of the TIRFM system is in Figure 1(c). An upright Olympus BX51 microscope (Olympus Optical Co., Ltd., Tokyo, Japan) with an Olympus 100 \times UPLFL objective lens (oil type, 1.3 N.A., W.D. 0.1 mm) was used. A 520/10 nm band-pass filter from Semrock (Rochester, NY, USA) was coordinated with the use of 473 nm laser excitation during imaging. Fluorescence images were captured by an electron-multiplying, cooled charge-coupled device (EM-CCD) camera (QuantEM 512SC, Photometrics, AZ, USA) equipped with a Uniblitz mechanical shutter (Vincent Associates, Rochester, NY, USA) with an exposure time of 100 ms. All quantitative analysis of data and image acquisition used MetaMorph 7.1 software (Universal Imaging Co., Downing Town, PA, USA).

3. Results and Discussion

A single-molecule sandwich immunoassay for sensitive detection of AFP by evanescent field-enhanced fluorescence was designed. The sensitivity of the AFP assay could calculate the detection limit of 720 zM using 100 nm gold nano-patterned chips. Size reduction and site-specific labeling of antibodies to create a surface with high functional capacity increases the sensitivity of an immunoassay [27]. Furthermore, the 100 nm gold array chips showed no quenching of fluorescence dyes and had increased sensitivity. Under optimal conditions, the sandwich immunoassay had high sensitivity and a wide dynamic range for monitoring on a single-molecule level.

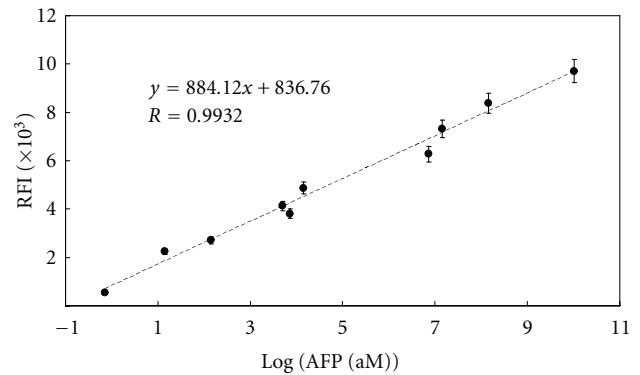


FIGURE 2: Calibration curve with linear range of standard AFP concentrations produced by serial dilutions from 720 zM to 10 nM. Relative fluorescence intensity (RFI) was corrected by background subtraction.

The increase in relative fluorescence intensity (RFI) was proportional to AFP concentration (Figure 2), and the linear response range was 720 zM to 10 nM (linear regression equation, $y = 884.12x + 836.76$, $R = 0.9932$) with a low detection limit of 720 zM and a signal-to-noise ratio (S/N) of 3 (Table 1). The AFP-nanoarray chip method showed 40,000 times higher sensitivity than other methods (i.e., surface plasmon resonance, bioluminescent immunoassay, electrochemical immunoassay, and chemiluminescence immunoassay). These results showed that the proposed method was highly sensitive, especially for ultralow levels of AFP.

In addition, the wide quantification range (720 zM to 10 nM) would be useful for healthy human serum, which has unestablished normal ranges for AFP. The normal range of AFP for adults and children is variously reported as under 50 ng/mL [38], under 10 ng/mL [39], and under 5 ng/mL [40]. Bader et al., Wang and Xu reported that the average concentration of AFP is about 25 ng/mL in healthy human

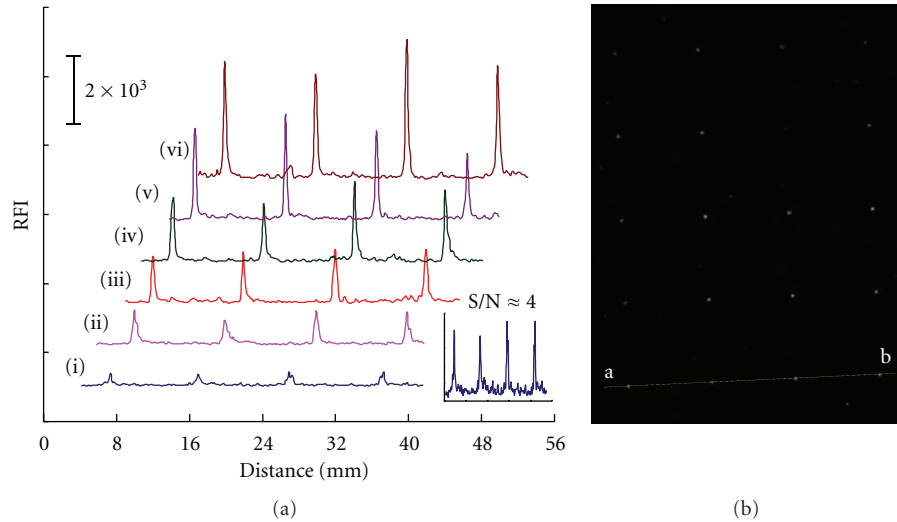


FIGURE 3: (a) Peak of fluorescence intensity of serially diluted AFP standard antigen reacted with a chip as “a” to “b” horizontal line in (b). (i) 14.3 aM; (ii) 7.2 fM; (iii) 14.3 fM; (iv) 7.2 pM; (v) 14.3 pM; (vi) 143 pM. RFI: relative fluorescence intensity.

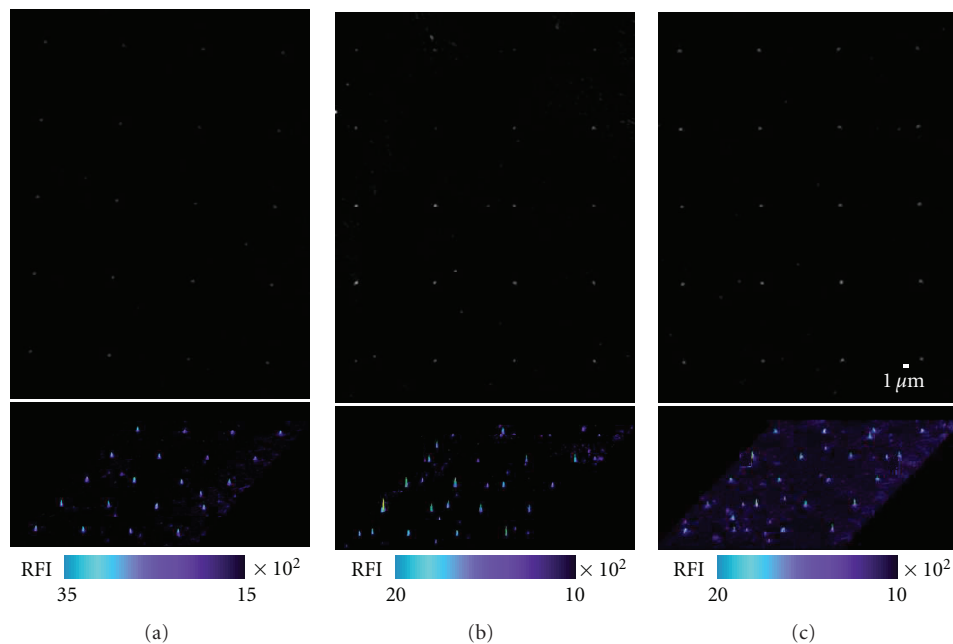


FIGURE 4: Evanescent field-enhanced fluorescence images *via* prism-type TIRFM of (a) standard AFP (AFP-positive sample), (b) normal (nonpathologic) human serum, and (c) AFP-spiked human serum on gold nanopatterned chip.

serum [41, 42]. Ju et al. also reported a low average value of 3.4 ng/mL [43]. However, a level above 500 ng/mL of AFP in adults can be indicative of HCC, germ cell tumors, and metastatic liver cancer.

The assay method for quantitative analysis was based on evanescent field-enhanced fluorescence imaging *via* prism-type TIRFM. First, we selected signal regions and background regions with the same area. The sum of TIRF intensities of occupied pixels per single spot was corrected by background subtraction and RFI was calculated. Figure 3(a) shows the peak of fluorescence intensity of serial diluted AFP

standard antigen reacted on chip. The peak width was greater than the spot diameter of 100 nm because of fluorescence imaging. The peak shows a moderate increase with increasing AFP concentration from 14.3 aM to 143 pM.

In this study, samples including standard AFP antigen, normal human serum, and human serum with added standard AFP antigen were evaluated using TIRFM and single-molecule sandwich immunoassay chips. The AFP standard (AFP, positive sample) (Figure 4(a), 1.42 pg/mL = 20 fM), normal (nonpathologic) human serum (Figure 4(b), 0.13 pg/mL = 1.8 fM), and the sample of human serum

spiked with AFP (Figure 4(c), 1.16 pg/mL = 16.3 fM; theoretical, 1.1 pg/mL = 15.4 fM) were analyzed using gold nanopatterned chips. The results indicated that the sandwich immunoassay using the gold nanopatterned chips gave the high accuracy and sensitivity required for the quantification of biomarkers in human serum samples.

Specificity is an important factor in practical use of immunoassays. AFP is closely related to albumin, both genetically and structurally. The amino acid sequences of AFP and albumin have extensive homology, and the genes coding for the proteins are localized to the same area of human chromosome 4 (4q11–q13) [44]. Since the 1980s, research on monoclonal antibodies with unique specificity for individual binding sites on antigens has been used to improve the sensitivity and specificity of AFP determination [45]. Ding et al. evaluated the selectivity of an immunosensor with four kinds of potential interferents, including L-glutamic acid, bovine serum albumin, hemoglobin, and D-glucose [32]. Chan et al. showed specificity satisfactory with paired monoclonal antibodies for AFP [46]. The monoclonal antibodies against human AFP from Biodesign International (5H7 and 4A3) that we used for the AFP sandwich assay specifically recognized the human AFP molecule [47]. This allowed us to ignore the negligible effects of interfering antigens in the AFP sandwich immunoassay.

4. Conclusions

We developed a single-molecule sandwich immunoassay on gold nanopatterned chips that was highly sensitive for AFP detection in human serum. The method has a wide range of quantitation and could be applied for testing healthy human serum with the normal range of AFP that has been reported as 47.6 pM–700 pM. The method could be used to diagnose AFP-negative or AFP-positive human serum from pathological clinical samples.

The linear response range of the assay for AFP concentration was 720 zM to 10 nM with a correlation coefficient of 0.9932. The detection limit of 50×10^{-9} ng/mL (720 zM) with a *S/N* of 3 was in linear range of the calibration curve, and much lower than LODs from 0.004 ng/mL to 20 ng/mL reported for other methods [28–31, 33–35]. For the AutoDELFIA hAFP immunoassay for the quantitative determination of hAFP, Mannings et al. established that falsely low AFP concentrations occur in 2.8% of samples with AFP concentrations <15 kU/L (13.8 ng/mL = 193 pM) due to immunoassay interference [48]. Our results showed that a sandwich immunoassay chip for quantitative analysis of AFP by evanescent field-enhanced fluorescence imaging was simple and sufficiently sensitive for determination of AFP in human serum samples. The assay had good precision and accuracy at the single-molecule level. The new immunoassay is expected to be widely useful for highly sensitive clinical analysis and other biotechnology applications.

Conflict of Interests

The authors have declared no conflict of interests.

Acknowledgment

This research was supported by a postdoctoral fellowship Grant from Kyung Hee University in 2011 (KHU-20110212).

References

- [1] D. W. Chan and S. Sell, "Tumor markers," in *Tietz Text Book of Clinical Chemistry*, C. A. Burtis and E. R. Ashwood, Eds., pp. 897–927, WB Saunders Company, Philadelphia, Pa, USA, 2nd edition, 1994.
- [2] C. M. Sturgeon, "Tumor markers in the laboratory: closing the guideline-practice gap," *Clinical Biochemistry*, vol. 34, no. 5, pp. 353–359, 2001.
- [3] M. S. Wilson, "Electrochemical immunosensors for the simultaneous detection of two tumor markers," *Analytical Chemistry*, vol. 77, no. 5, pp. 1496–1502, 2005.
- [4] T. Konry, A. Novoa, Y. Shemer-Avni et al., "Optical fiber immunosensor based on a poly(pyrrole-benzophenone) film for the detection of antibodies to viral antigen," *Analytical Chemistry*, vol. 77, no. 6, pp. 1771–1779, 2005.
- [5] B. Zuo, S. Li, Z. Guo, J. Zhang, and C. Chen, "Piezoelectric immunosensor for SARS-associated coronavirus in sputum," *Analytical Chemistry*, vol. 76, no. 13, pp. 3536–3540, 2004.
- [6] R. Kurita, Y. Yokota, Y. Sato, F. Mizutani, and O. Niwa, "On-chip enzyme immunoassay of a cardiac marker using a microfluidic device combined with a portable surface plasmon resonance system," *Analytical Chemistry*, vol. 78, no. 15, pp. 5525–5531, 2006.
- [7] S. Lee, N. P. Cho, J. D. Kim, H. Jung, and S. H. Kang, "An ultra-sensitive nanoarray chip based on single-molecule sandwich immunoassay and TIRFM for protein detection in biologic fluids," *Analyst*, vol. 134, no. 5, pp. 933–938, 2009.
- [8] S. Lee, S. Lee, Y. H. Ko et al., "Quantitative analysis of human serum leptin using a nanoarray protein chip based on single-molecule sandwich immunoassay," *Talanta*, vol. 78, no. 2, pp. 608–612, 2009.
- [9] H. Yoshima, T. Mizuochi, M. Ishii, and A. Kobata, "Structure of the asparagine-linked sugar chains of α -fetoprotein purified from human ascites fluid," *Cancer Research*, vol. 40, no. 11, pp. 4276–4281, 1980.
- [10] G. J. Mizejewski, " α -fetoprotein as a biologic response modifier: relevance to domain and subdomain structure," *Proceedings of the Society for Experimental Biology and Medicine*, vol. 215, no. 4, pp. 333–362, 1997.
- [11] E. Alpert, R. Hershberg, P. H. Schur, and K. J. Isselbacher, "Alpha-fetoprotein in human hepatoma: improved detection in serum, and quantitative studies using a new sensitive technique," *Gastroenterology*, vol. 61, no. 2, pp. 137–143, 1971.
- [12] X. W. Wang and H. Xie, "Alpha-fetoprotein enhances the proliferation of human hepatoma cells in vitro," *Life Sciences*, vol. 64, no. 1, pp. 17–23, 1998.
- [13] G. I. Abelev, S. D. Perova, N. I. Khramkova, Z. A. Postnikova, and I. S. Irlin, "Production of embryonal alpha-globulin by transplantable mouse hepatomas," *Transplantation*, vol. 1, pp. 174–180, 1963.
- [14] M. E. Alpert, J. Uriel, and B. de Nechaud, "Alpha-1 fetoglobulin in the diagnosis of human hepatoma," *The New England Journal of Medicine*, vol. 278, no. 18, pp. 984–986, 1968.
- [15] L. R. Purves, M. MacNab, E. W. Geddes, and I. Bersohn, "Serum-alpha-foetoprotein and primary hepatic cancer," *The Lancet*, vol. 1, no. 7548, pp. 921–922, 1968.

- [16] J. B. Smith and D. Todd, "Foetoglobulin and primary liver cancer," *The Lancet*, vol. 2, no. 7572, p. 833, 1968.
- [17] M. C. Kew, "Alpha-fetoprotein," in *Modern Trends in Gastroenterology*, A. E. Read, Ed., vol. 5, p. 91, Butterworths, London, UK, 1975.
- [18] H. F. Deutsch, "Chemistry and biology of α -fetoprotein," *Advances in Cancer Research*, vol. 56, pp. 253–312, 1991.
- [19] G. J. Mizejewski, "Alpha-fetoprotein structure and function: relevance to isoforms, epitopes, and conformational variants," *Experimental Biology and Medicine*, vol. 226, no. 5, pp. 377–408, 2001.
- [20] A. A. Terentiev and N. T. Moldogazieva, "Structural and functional mapping of α -fetoprotein," *Biochemistry*, vol. 71, no. 2, pp. 120–132, 2006.
- [21] E. Ruoslahti and M. Seppälä, "Studies of carcino-fetal proteins. 3. Development of a radioimmunoassay for -fetoprotein. Demonstration of -fetoprotein in serum of healthy human adults," *International Journal of Cancer*, vol. 8, no. 3, pp. 374–383, 1971.
- [22] R. P. Liang, G. H. Yao, L. X. Fan, and J. D. Qiu, "Magnetic Fe₃O₄@Au composite-enhanced surface plasmon resonance for ultrasensitive detection of magnetic nanoparticle-enriched α -fetoprotein," *Analytica Chimica Acta*, vol. 737, no. 6, pp. 22–28, 2012.
- [23] S. Inouye and J. Sato, "Purification of histidine-tagged aequorin with a reactive cysteine residue for chemical conjugations and its application for bioluminescent sandwich immunoassays," *Protein Expression and Purification*, vol. 83, no. 2, pp. 205–210, 2012.
- [24] B. Zhang, D. Tang, B. Liu, H. Chen, Y. Cui, and G. Chen, "GoldMag nanocomposite-functionalized graphene sensing platform for one-step electrochemical immunoassay of alpha-fetoprotein," *Biosensors and Bioelectronics*, vol. 28, no. 1, pp. 174–180, 2011.
- [25] X. Huang and J. Ren, "Gold nanoparticles based chemiluminescent resonance energy transfer for immunoassay of alpha fetoprotein cancer marker," *Analytica Chimica Acta*, vol. 686, no. 1–2, pp. 115–120, 2011.
- [26] J. Bruix, M. Sherman, J. M. Llovet et al., "Clinical management of hepatocellular carcinoma. Conclusions of the barcelona-2000 EASL conference," *Journal of Hepatology*, vol. 35, no. 3, pp. 421–430, 2001.
- [27] J. Ylikotila, L. Välimaa, M. Vehniäinen, H. Takalo, T. Lövgren, and K. Pettersson, "A sensitive TSH assay in spot-coated microwells utilizing recombinant antibody fragments," *Journal of Immunological Methods*, vol. 306, no. 1–2, pp. 104–114, 2005.
- [28] S. Inouye and J. I. Sato, "Comparison of luminescent immunoassays using biotinylated proteins of aequorin, alkaline phosphatase and horseradish peroxidase as reporters," *Bioscience, Biotechnology and Biochemistry*, vol. 72, no. 12, pp. 3310–3313, 2008.
- [29] S. Inouye and J. I. Sato, "Recombinant aequorin with a reactive cysteine residue for conjugation with maleimide-activated antibody," *Analytical Biochemistry*, vol. 378, no. 1, pp. 105–107, 2008.
- [30] B. Y. Wu, H. F. Wang, J. T. Chen, and X. P. Yan, "Fluorescence resonance energy transfer inhibition assay for α -fetoprotein excreted during cancer cell growth using functionalized persistent luminescence nanoparticles," *Journal of the American Chemical Society*, vol. 133, no. 4, pp. 686–688, 2011.
- [31] B. Zhang, X. Zhang, H. H. Yan, S. J. Xu, D. H. Tang, and W. L. Fu, "A novel multi-array immunoassay device for tumor markers based on insert-plug model of piezoelectric immunosensor," *Biosensors and Bioelectronics*, vol. 23, no. 1, pp. 19–25, 2007.
- [32] C. Ding, F. Zhao, R. Ren, and J. M. Lin, "An electrochemical biosensor for α -fetoprotein based on carbon paste electrode constructed of room temperature ionic liquid and gold nanoparticles," *Talanta*, vol. 78, no. 3, pp. 1148–1154, 2009.
- [33] R. P. Liang, Z. X. Wang, L. Zhang, and J. D. Qiu, "A label-free amperometric immunosensor for alpha-fetoprotein determination based on highly ordered porous multi-walled carbon nanotubes/silica nanoparticles array platform," *Sensors and Actuators B*, vol. 166–167, pp. 569–575, 2012.
- [34] N. Gan, L. Jia, and L. Zheng, "A novel sandwich electrochemical immunosensor based on the DNA-derived magnetic nanochain probes for alpha-fetoprotein," *Journal of Automated Methods and Management in Chemistry*, vol. 2011, Article ID 957805, 7 pages, 2011.
- [35] B. Su, J. Tang, J. Huang et al., "Graphene and nanogold-functionalized immunosensing interface with enhanced sensitivity for one-step electrochemical immunoassay of alpha-fetoprotein in human serum," *Electroanalysis*, vol. 22, no. 22, pp. 2720–2728, 2010.
- [36] Q. Liu, M. Han, J. Bao, X. Jiang, and Z. Dai, "CdSe quantum dots as labels for sensitive immunoassay of cancer biomarker proteins by electrogenerated chemiluminescence," *Analyst*, vol. 136, no. 24, pp. 5197–5203, 2011.
- [37] J. Lin, Y. Zhao, Z. Wei, and W. Wang, "Chemiluminescence immunoassay based on dual signal amplification strategy of Au/mesoporous silica and multienzyme functionalized mesoporous silica," *Materials Science and Engineering B*, vol. 176, no. 18, pp. 1474–1478, 2011.
- [38] Y. S. Kim, S. H. Kim, J. K. Seong, B. S. Lee, H. Y. Jeong, and K. S. Song, "Gastric yolk sac tumor: a case report and review of the literature," *Korean Journal of Internal Medicine*, vol. 24, no. 2, pp. 143–146, 2009.
- [39] D. Ball, E. Rose, and E. Alpert, "Alpha-fetoprotein levels in normal adults," *American Journal of the Medical Sciences*, vol. 303, no. 3, pp. 157–159, 1992.
- [40] P. Sizaret, N. Martel, A. Tuyns, and S. Reynaud, "Mean α fetoprotein values of 1,333 males over 15 years by age groups," *Digestion*, vol. 15, no. 2, pp. 97–103, 1977.
- [41] D. Bader, A. Riskin, O. Vafsi et al., "Alpha-fetoprotein in the early neonatal period—a large study and review of the literature," *Clinica Chimica Acta*, vol. 349, no. 1–2, pp. 15–23, 2004.
- [42] X. W. Wang and B. Xu, "Stimulation of tumor-cell growth by alpha-fetoprotein," *International Journal of Cancer*, vol. 75, no. 4, pp. 596–599, 1998.
- [43] H. Ju, G. Yan, F. Chen, and H. Chen, "Enzyme-linked immunoassay of α -1-fetoprotein in serum by differential pulse voltammetry," *Electroanalysis*, vol. 11, no. 2, pp. 124–128, 1999.
- [44] P. P. Minghetti, M. E. Harper, E. Alpert, and A. Dugaiczky, "Chromosomal structure and localization of the human α -fetoprotein gene," *Annals of the New York Academy of Sciences*, vol. 417, pp. 1–12, 1983.
- [45] D. H. Bellet, J. R. Wands, K. J. Isselbacher, and C. Bohuon, "Serum α -fetoprotein levels in human disease: perspective from a highly specific monoclonal radioimmunoassay," *Proceedings of the National Academy of Sciences of the United States of America*, vol. 81, no. 12, pp. 3869–3873, 1984.
- [46] D. W. Chan, M. Kelsten, R. Rock, and D. Bruzek, "Evaluation of a monoclonal immunoenzymometric assay for alpha-fetoprotein," *Clinical Chemistry*, vol. 32, no. 7, pp. 1318–1322, 1986.

[47] <https://meridianlifescience.com/>.

[48] L. Mannings, S. Trow, J. Newman, B. Nix, and C. Evans, "Interference in the autoDELFIa hAFP immunoassay and effect on second-trimester Down's syndrome screening," *Annals of Clinical Biochemistry*, vol. 48, no. 5, pp. 438–440, 2011.

Review Article

Semiconductor Quantum Dots Surface Modification for Potential Cancer Diagnostic and Therapeutic Applications

Jidong Wang,¹ Shumin Han,^{1,2} Dandan Ke,¹ and Ruibing Wang³

¹ College of Environmental and Chemical Engineering, Yanshan University, Qinhuangdao 066004, China

² State Key Laboratory of Metastable Materials Science and Technology, Yanshan University, Qinhuangdao 066004, China

³ Targeted Therapy Unit, Nordion Inc., 447 March Road, Ottawa, ON, Canada K2K 1X8

Correspondence should be addressed to Shumin Han, hanshm@ysu.edu.cn and Ruibing Wang, ruibing.wang@nordion.com

Received 4 September 2012; Accepted 20 September 2012

Academic Editor: Haiyan Li

Copyright © 2012 Jidong Wang et al. This is an open access article distributed under the Creative Commons Attribution License, which permits unrestricted use, distribution, and reproduction in any medium, provided the original work is properly cited.

Semiconductor Quantum dots (QDs) have generated extensive interest for biological and clinical applications. These applications arise from their unique properties, such as high brightness, long-term stability, simultaneous detection of multiple signals, tunable emission spectra. However, high-quality QDs, whether single or core-shell QDs, are most commonly synthesized in organic solution and surface-stabilized with hydrophobic organic ligands and thus lack intrinsic aqueous solubility. For biological applications, very often it is necessary to make the QDs dispersible in water and therefore to modify the QD surfaces with various bifunctional surface ligands or caps to promote solubility in aqueous media. Well-defined methods have been developed for QD surface modification to impart biocompatibility to these systems. In this review, we summarize the recent progress and strategies of QDs surface modification for potential cancer diagnostic and therapeutic applications. In addition, the question that arose from QD surface modification, such as impact of size increase of QD bioconjugates after surface-functionalization or surface modification on photophysical properties of QDs, are also discussed.

1. Introduction

Cancer is one of the most serious health threats worldwide, with an estimated 12.7 million new cases and 7.6 million cancer deaths in 2008 [1]. Cancer is greatly feared due to the widespread occurrence of this disease, its high death rate, and recurrence after treatment. The application of nanotechnology in medicine has provided an unprecedented opportunity for addressing many of the current challenges in the diagnosis and treatment of cancer [2, 3].

Semiconductor quantum dots (QDs) have great potential in biomedical fields, due to their excellent optical properties. QDs exhibit discrete size-dependent energy levels. As the size of the nanocrystal increases, the energy gap decreases, yielding a size-dependent rainbow of colors. By varying the size and the composition of the QDs, light wavelengths from the ultraviolet to the infrared range can be achieved, so that they enable simultaneous examination of multiple molecules and events [4]. QDs have unique optical spectra compared to organic fluorophores. Organic dyes typically have narrow

absorption spectra, which mean that they can only be excited within a narrow window of wavelengths. Furthermore, organic dyes have asymmetric emission spectra broadened by a red tail. In contrast, QDs have broad absorption spectra, enabling excitation by a wide range of wavelengths, and their emission spectra are symmetric and narrow. Consequently, multicolor nanocrystals of different sizes can be excited by a single wavelength shorter than their emission wavelengths, with minimum signal overlap. QDs are also relatively stable light emitters owing to their inorganic composition, making them less susceptible to photobleaching than organic dye molecules [5, 6]. The unique optical properties of QDs make them appealing as *in vivo* and *in vitro* fluorophores in various biological and medical applications, such as diagnosis and therapy of cancer [7–11].

QDs are usually utilized as either core-only or core-shell structures [12]. Core-shell nanoparticles are more desirable for biological applications as the core being passivated by the shell (usually a wider band-gap material), which improves fluorescent properties and prevents leaching. Core-shell

QDs are typically synthesized from various semiconductor materials which can provide access to a full range of potential emission wavelengths. High-quality QDs, whether single or core-shell structures, are most commonly synthesized in organic solution and surface-stabilized with hydrophobic organic ligands and thus lack intrinsic aqueous solubility. For biological applications, it is necessary to alter the QDs so that they become dispersible in water, and therefore to modify the QDs surface with various bifunctional surface ligands or caps to promote solubility in aqueous media [4, 13–16]. Also, the attachment of biological molecules to the QD surface needs to provide the desired specific biorecognition and/or targeting properties. In some cases, the QD surface ligands must accomplish this mission by providing unique functional groups, such as carboxyls or amines, for the multistep covalent chemical coupling of biomolecules. Therefore, surface modification is vital for QDs in biological applications. In this paper, we summarize the recent progress and strategies in QDs surface modification for cancer diagnostics and therapeutics related applications: (1) the growth of additional layer, for instance a silica shell, around the nanoparticles, through surface silanization; (2) the exchange of hydrophobic surfactant molecules with bifunctional molecules; (3) coating of QD surfaces with amphiphilic polymers, phospholipid micelles, or microspheres. Moreover, the questions that arose from QD surface modification, such as the impact size increase of QD bioconjugates after surface functionalization or surface modification on photophysical properties of QDs, are also discussed.

2. Silanization

In order to render QDs more effective and also more biocompatible for potential cancer diagnostics and therapeutic-related biomedical applications, one of the most preferred approaches is to introduce a silica shell covering the QDs [17, 18]. This approach is also called surface silanization [6, 19]. The first step of this process involves exchanging the surface ligand with a thiol-derived silane, such as mercaptopropyltris(methoxy)silane (MPS). The trimethoxysilane groups can be cross-linked by the formation of siloxane bonds. During further silica shell growth, other types of silicon can be added to render a different charge and provide functional groups on the surface (Figure 1) [4]. Those most frequently used are aminopropylsilanes (APS), phosphosilanes, and polyethylene glycol (PEG)-silane [19, 20]. Because the silica shells are highly cross-linked, silanized QDs are extremely stable. Silanization is preferred also because it is less toxic in comparison with other ligands [21, 22]. Most reports of silica coated systems are limited up to the cytotoxicity evaluation [23–25]. For example, for *in vivo* applications, these materials have to travel through body fluids such as like blood. In that sense, the materials have to satisfy the mandatory criteria such as basic haemocompatibility [26].

A number of reports have been devoted to silica coating of colloidal nanoparticles by aqueous classical methods such as Stöber synthesis methodology [27–29], silicate water-glass methodology [30, 31], and the methodology using sodium of silane coupling agents [32]. Recently, many new approaches

have been explored. Based on classical methods, Guerrero-Martínez et al. [30] developed three different synthetic strategies, including: (i) the use of water-in-oil (W/O) microemulsions to coat nanoparticles such as metal colloids, magnetic nanoparticles, and semiconductor nanocrystals, (ii) silica coating of polymeric aggregates, surfactant vesicles, and polymer/surfactant stabilized inorganic nanoparticles, and (iii) assembly of silica colloids on nano- and microparticles by various physisorption strategies (Figure 2). Although many groups have also successfully prepared silica-coated core-shell QDs, the various types of surface-silanized QDs still could be divided into three classes, such as single QDs, core-shell QDs, and multiple-layered QDs being coated by silica shell.

Firstly, Chen et al. [33] synthesized CdTe QDs coated with silica particles and the particles surface was further functionalized covalently with α -fetoprotein antibody, anti-AFP (secondary antibodies denoted Ab₂). This work presents a novel strategy for ultrasensitive detection of biomarkers based on CdTe quantum dot. The enhanced detection of biomarkers based on single QD-functionalized silica nanosphere labels was achieved by an increase in CdTe QDs loading per sandwiched immunoreaction. Tan et al. [34] utilized silica functionalized PbSe QDs on two different cell lines for cytotoxic studies and found that the silica-coated PbSe QDs were much less cytotoxic than the polymer coated PbSe QDs, which were used for comparison.

More interestingly, Selvan et al. [35] employed Igepal as a nonionic surfactant and synthesized 20–30 nm silica-coated CdSe/ZnS/SiO₂ QDs via a reverse microemulsion. The QDs displayed comparable quantum yields to CdSe/ZnS QDs, but were much less toxic than organic-coated water-soluble QDs. Also, Bruchez et al. [6] extended the CdSe/CdS/SiO₂ core-shell systems by adding a third layer of silica to labeled 3T3 mouse fibroblast cells. Furthermore, Durgadas et al. [26] reported CuSe/ZnS/Silica QDs, which were conjugated with an anticancer drug and labeled HepG2 and C6 glioma cancer cells. They also pointed out that the improvement of the core/shell/shell QD synthesis would expand the applications of QDs in disease site targeting and cellular labeling.

Finally, Yi et al. [36] and Selvan et al. [37] encapsulated QDs and magnetic nanoparticles (MPs) in a silica shell using a reverse microemulsion synthesis. The resulting MPs (γ -Fe₂O₃)-QDs (CdSe)/SiO₂ nanocomposite particles present a unique combination of magnetic and optical properties. Their nonporous silica shell facilitated their surface modification for bioconjugation in various biomedical applications. For example, the synthesis of multifunctional nanoparticles, in which both QDs and magnetic particles were coated with silica, was used for live cell imaging of human liver cancer cells (HepG2), mouse fibroblast cells (NIH-3T3), and the protein detection.

In general, these silica-coated core-shell nanostructured architectures are fascinating hybrid materials that combine various types of cores with silica that possess superior stability and little toxicity. In addition, the careful control over the thickness of the silica shell can provide sensitive tuning of the response to light and magnetic information. Silica-coated

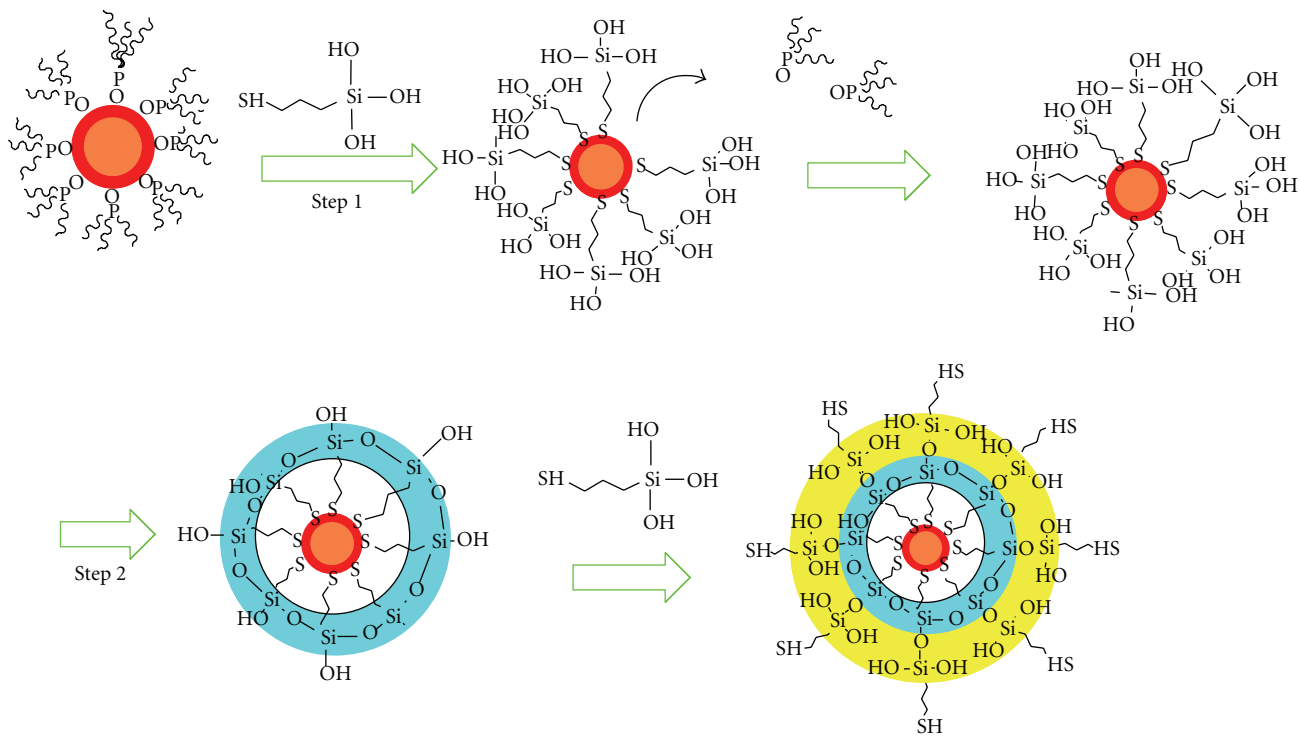


FIGURE 1: Surface silanization sketch of TOPO-capped CdSeZnS core/shell particles by mercaptopropyltris(methoxy)silane (MPS). The diagram was adapted from [4].

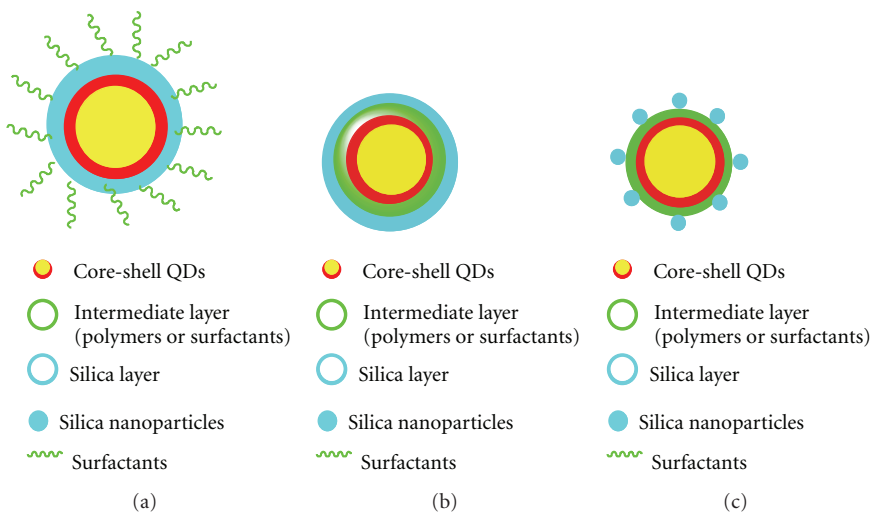


FIGURE 2: Three synthetic approaches of silica coated nanomaterials. (a) W/O microemulsion method, (b) silica coating the polymers or surfactants, (c) silica nanoparticles self-assembled onto nanomaterials.

systems also could be beneficial for electronic and biosensing applications.

3. Ligand Exchange

Among the strategies that have been used to stabilize core or core-shell nanocrystals in aqueous solutions, the most common approach is to exchange the hydrophobic

surfactant molecules with bifunctional molecules, which are hydrophilic on one end and hydrophobic on the other end. Because these bifunctional molecules replace the hydrophobic surfactants, this process is called ligand exchange [19]. Among the bifunctional molecules, thiols (-SH) are used as anchoring groups to bind to the QDs surface, while carboxyl (-COOH) groups are used as the hydrophilic ends. Numerous examples of QD surface ligand exchange with using bifunctional biorelevant molecules such as cysteine,

mercaptosuccinic acid, and glutathione have provided finished materials with opportunities for biomedical applications [38].

3.1. Cysteine. Liu et al. [39] developed a compact cysteine coating on a highly robust CdSe/ZnCdS QD to form water-soluble QDs via ligand exchange. These QDs were biologically compatible, extraordinarily compact, highly fluorescent, and easily functionalized nanocrystals for *in vivo* targeted imaging. Choi et al. [40] also coated CdSe/ZnS QDs with cysteine by ligand exchange and precisely defined the requirements for renal filtration and urinary excretion of inorganic, metal-containing nanoparticles. They reported that the hydrodynamic diameter (HD) was smaller than 5.5 nm, which was beneficial for rapid and efficient urinary excretion and elimination of QDs from the body. This study provided a foundation for the design and development of biotargeting nanoparticles for biomedical applications [41, 42].

3.2. Mercaptosuccinic Acid. Yong et al. [43] functionalized the InP/ZnS QDs with mercaptosuccinic acid to render them highly dispersible in aqueous media and allowed specific *in vitro* targeting of pancreatic cancer cell lines. This work has suggested the immense potential of InP/ZnS QDs as safe and efficient non-cadmium-based optical imaging nanoprobe for the early detection of cancer.

3.3. Polyethylene Glycol. Choi et al. [44] coated InAs/ZnS QDs with various chain length of polyethylene glycol (PEG). They found that increasing the PEG chain length from 2 to 22 units not only resulted in changes in hydrodynamic diameter, but also resulted in better targeting to the liver, kidney, pancreas, and lymph nodes.

3.4. Mercaptoacetic Acid. Yu et al. [45] synthesized mercaptoacetic acid (MAA) coated CdSe/ZnS QDs via ligand exchange and linked QDs to alpha-fetoprotein (AFP) antibodies for specific binding with AFP. They achieved specific fluorescence detection with the QD-anti-AFP in nude mice xenografted with cancer. The fluorescence results demonstrated that QD-Anti-AFP fluorescent spectral and lifetimes had not varied much from that of the original QDs. Moreover, QD-Anti-AFP had exhibited higher fluorescence efficiencies than QDs under two-photon excitation.

3.5. Glutathione. Tiwari et al. [46] used glutathione to coat CdSe/CdZnS QDs (GSH-QDs) and anti-HER2 antibodies to conjugate QDs (HER2Ab-QDs) using different coupling agents (EDC(1-ethyl-3-(3-dimethyl-aminopropyl)carbodiimide)/sulfo-NHS(3-sulfo-N-hydroxy-succinimide sodium salt), iminothiolane/sulfo-SMCC(sulfosuccinimidyl-*trans*-4-(*N*-maleimidomethyl)cyclohexane-1-carboxylate), and sulfo-SMCC). These fluorescent probes have great potential for the precise determination of HER2 status among breast cancer patients at the cellular levels.

3.6. Ligand Exchange with Other Molecules. QDs functionalized with polyamidoamine (PAMAM) [47–49] and polyisoprene [38] have shown great potential for applications

in cancer targeting and molecular imaging, such as gastric cancer cells. The resulting water-soluble QDs have shown fluorescence quantum efficiencies in the 40 to 50% range and extraordinary fluorescence stability in biological environments after cross-linking of the ligand shell.

Although many biological applications of QDs have been achieved by using bifunctional molecules to render QDs water soluble, this approach can often negatively alter the chemical and physical states of the QDs surface and cause a dramatic decrease in the quantum efficiency. For example, Jin et al. [50] modified the surfaces of hydrophobic CdSeTe/CdS QDs with GSH in a tetrahydrofuran-water solution and these QDs exhibited quantum yields of only 22%. Moreover, the stability of the QDs has not been well understood under *in vivo* conditions. The long-term stability of the QDs depends on the bond between the thiol group and the QD surface, which can be weak with oxidation. Consequently, the thiol-based molecules can become cleaved from the QD surface, causing the QDs to aggregate and precipitate from solution.

4. Amphiphilic Polymer Coatings

Instead of exchanging the hydrophobic surfactant, the QDs in this case are coated with a cross-linked amphiphilic polymer. The hydrophobic part of the amphiphile is designed to interact with the hydrophobic chains of the surface ligands, and the hydrophilic component (most commonly in the form of carboxyl groups or polyethylene glycol chains) provides water solubility and chemical functionality.

The CdSe/ZnS QDs [58, 59], after being coated by PEG(poly(ethylene glycol)), were conjugated with monoclonal anti-EGFR (epidermal growth factor receptor) antibodies (cetuximab) through two long-chain heterobifunctional linkers, sulfo-LC-SPDP(sulfosuccinimidyl 6-[3'-(2-pyridyldithio)propionamido]hexanoate) and sulfo-SMCC(sulfosuccinimidyl-*trans*-4-(*N*-maleimidomethyl)cyclohexane-1-carboxylate). The cellular imaging experiments using the QD-cetuximab conjugates showed a clear endocytosis pathway, which was evidenced by the colocalization of the QD-cetuximab conjugates with dye-labeled transferrin. These results suggest that the QD-cetuximab conjugates as an imaging modality for tumor EGFR overexpression can be expected to provide important information on the expression levels of EGFR among cancer cells. Such applications include *in vitro* assays, cellular imaging, and *in vivo* imaging applications.

During amphiphilic polymerization coating process, a cross-linking treatment is often performed. Although not always necessary, the cross-linking reactions are thought to increase the stability of the polymeric shell of the QDs. Hydrolysis of the remaining anhydride groups transfers the polymer-coated QDs to the water phase. This treatment also provides a large number of carboxylic units, which can be used for further derivatization. Although there are relatively few literature examples of QDs coated with amphiphilic polymers, the methods based on hydrophobic interactions between the QD ligands and polymer functionalities have

TABLE 1: QD/microbead hybrid material preparation methods and their characteristics and biomedical applications.

Approaches	QDs	Characteristics or applications
QDs are absorbed into the subsurface region of microbeads, as the solvent is removed	(a) CdSe/ZnS [51]	(1) Bead identification accuracies as high as 99.99%
	(b) CdSeTe [52]	(2) The coding and target signals of DNA hybridization at the single-bead level (1) Both single- and dual-color codes were also obtained (2) Good detection sensitivity and low cytotoxicity on suspension immunoassay for goat antimouse IgG on the xMAP platform
QDs are electrostatically bound to the surfaces of the microspheres, using layer-by-layer strategy	(a) CdTe [53]	More flexibility for creating QD-beads in biomedicine applications (sensing, immunoassay, encoding, and diagnostic)
	(b) CdTe [54]	Cytotoxicity reductions
QDs grow around preformed silica spheres	CdSe, CdSe/ZnS, or CdSe/ZnSe/ZnS [55]	A comparatively stable and noncytotoxic intracellular delivery
QDs are incorporated into polymer microbeads through emulsion and suspension polymerization	(a) CdSe/ZnS [56]	Good detection sensitivity of rabbit IgG molecules onto the surfaces of the microbeads-QDs
	(b) Cd _{1-x} Zn _x Se _{1-y} S _y [57]	High-throughput multiplexed biomolecular immunoassay for human IgG detection

already addressed many problems related to undesired ligand exchange reactions.

5. Micellar Phospholipid Coatings

The encapsulation of QDs within phospholipid micelles is attractive for several reasons [60–62]: firstly, the encapsulation step does not alter the surface, secondly, the optical properties of the QDs are retained, and thirdly, the micelles have highly dense surfaces, which prevents nonspecific adsorption so that the supramolecular architecture is maintained by local hydrophobic interactions.

Dubertret et al. [63] encapsulated individual CdSe/ZnS QDs in phospholipid block copolymer micelles and demonstrated both *in vitro* and *in vivo* imaging. When conjugated to DNA, the nanocrystal-micelles acted as *in vitro* fluorescent probes to hybridize to specific complementary sequences. In comparison with other systems, they simultaneously provided efficient fluorescence, a great reduction in photobleaching, colloidal stability in various biological environments, and low nonspecific adsorption. Hu et al. [64] also reported alloyed CdTe_{1-x}Se_x/CdS QDs encapsulated within PEG-grafted phospholipid micelles. For tumor-specific delivery *in vivo*, the micelle-encapsulated QDs were conjugated with a cyclic arginine-glycine-aspartic acid (cRGD) peptide, which targeted the $\alpha_v\beta_3$ integrins that are overexpressed in angiogenic tumor vasculatures. Their work had demonstrated that these QDs provide a promising theranostic, nanosized platform for both cancer imaging and therapy. Erogbogbo et al. [65] reported that silicon QDs and iron oxide nanoparticles were coencapsulated by phospholipid-polyethylene glycol (DSPE-PEG) micelles. Their luminescence stability in a prostate cancer microenvironment was demonstrated *in vivo*. Many groups also have synthesized lipid-coated nanoparticles and used them in cellular and *in vivo* imaging [66–70]. The encapsulation of QDs by phospholipid micelles provides more opportunities for utilizing QDs in biological applications.

6. Microsphere/Microbead Coatings

Incorporating QDs in microspheres is of interest for both fundamental studies on light-matter interactions [71] and practical applications, such as semiconductor microlasing [72] and biological tags [6]. This dot-in-a-dot structure confines electrons and photons in all three dimensions. The spontaneous emission was enhanced from that of regular QDs because the QDs were embedded within the microcavities [73].

Methods to incorporate QDs into microbeads include the following approaches [74]. The first approach involves the dispersion of commercially available or synthesized microbeads and QDs in a solvent/nonsolvent mixture is chosen to cause the partial swelling of microbeads. QDs that are dispersed in the solution penetrate into the microbeads and, as the solvent is removed, are captured in the subsurface region of the microbeads. The second method utilizes a layer-by-layer strategy to adsorb QDs consecutively onto oppositely charged microbeads. In this scheme, QDs are electrostatically bound to the surfaces of the microspheres. The third approach involves the growth of a silica/QD shell around preformed silica spheres. Finally, the fourth approach involves loading QDs into polymer microbeads through emulsion and suspension polymerization. With these methods described above, various QDs can be incorporated into microspheres/microbeads and are further directed to more biomedical applications such as diagnostics (Table 1).

7. Summary and Future Challenges

The rapid development of nanotechnology has given the new hope in the early detection and potentially treatment of cancer. Much basic work on the engineering of QD surfaces and creating QD bioconjugates with control over all relevant properties has been accomplished. In spite of this, there are still many questions that remain unanswered. For example, size of a conjugate is also one crucial aspect. Although the sizes of QDs are comparable to those of

large proteins, it is important to note that the surface-functionalization and further conjugation of biomolecules can increase the sizes of QD bioconjugates. Such large sizes may limit access to intracellular organelles and alter the intrinsic activity of any attached proteins. Therefore, developing surface functionalization techniques that maintain a small overall size is highly desirable. Additionally, during exchange between hydrophobic surfactant molecules and bifunctional molecules, the long-term stability of the QDs become more dependent on thiol- and metal bonds, which are relatively weak. The real-world applications of thiol-capped core-shell QDs are therefore rather limited. All of these considerations would hinder the application of QDs in biomedical applications. Therefore, the development of an effective approach for QD surface functionalization still remains a challenge for this technology.

References

- [1] A. Jemal, F. Bray, M. M. Center, J. Ferlay, E. Ward, and D. Forman, "Global cancer statistics," *CA Cancer Journal for Clinicians*, vol. 61, no. 2, pp. 69–90, 2011.
- [2] S. M. Hanash, C. S. Baik, and O. Kallioniemi, "Emerging molecular biomarkers-blood-based strategies to detect and monitor cancer," *Nature Reviews Clinical Oncology*, vol. 8, no. 3, pp. 142–150, 2011.
- [3] J. A. Ludwig and J. N. Weinstein, "Biomarkers in cancer staging, prognosis and treatment selection," *Nature Reviews Cancer*, vol. 5, no. 11, pp. 845–856, 2005.
- [4] A. P. Alivisatos, W. Gu, and C. Larabell, "Quantum dots as cellular probes," *Annual Review of Biomedical Engineering*, vol. 7, pp. 55–76, 2005.
- [5] X. Michalet, F. Pinaud, T. D. Lacoste et al., "Properties of fluorescent semiconductor nanocrystals and their applications to biological labeling," *Single Molecules*, vol. 2, no. 4, pp. 261–276, 2001.
- [6] M. Bruchez, M. Moronne, P. Gin, S. Weiss, and A. P. Alivisatos, "Semiconductor nanocrystals as fluorescent biological labels," *Science*, vol. 281, no. 5385, pp. 2013–2016, 1998.
- [7] A. P. Alivisatos, "Semiconductor clusters, nanocrystals, and quantum dots," *Science*, vol. 271, no. 5251, pp. 933–937, 1996.
- [8] W. C. W. Chan and S. Nie, "Quantum dot bioconjugates for ultrasensitive nonisotopic detection," *Science*, vol. 281, no. 5385, pp. 2016–2018, 1998.
- [9] P. Mitchell, "Turning the spotlight on cellular imaging," *Nature Biotechnology*, vol. 19, no. 11, pp. 1013–1017, 2001.
- [10] W. C. W. Chan, D. J. Maxwell, X. Gao, R. E. Bailey, M. Han, and S. Nie, "Luminescent quantum dots for multiplexed biological detection and imaging," *Current Opinion in Biotechnology*, vol. 13, no. 1, pp. 40–46, 2002.
- [11] X. Michalet, F. F. Pinaud, L. A. Bentolila et al., "Quantum dots for live cells, in vivo imaging, and diagnostics," *Science*, vol. 307, no. 5709, pp. 538–544, 2005.
- [12] J. B. Delehanty, H. Mattoussi, and I. L. Medintz, "Delivering quantum dots into cells: strategies, progress and remaining issues," *Analytical and Bioanalytical Chemistry*, vol. 393, no. 4, pp. 1091–1105, 2009.
- [13] I. L. Medintz, H. T. Uyeda, E. R. Goldman, and H. Mattoussi, "Quantum dot bioconjugates for imaging, labelling and sensing," *Nature Materials*, vol. 4, no. 6, pp. 435–446, 2005.
- [14] F. Dubois, B. Mahler, B. Dubertret, E. Doris, and C. Mioskowski, "A versatile strategy for quantum dot ligand exchange," *Journal of the American Chemical Society*, vol. 129, no. 3, pp. 482–483, 2007.
- [15] P. Alivisatos, "The use of nanocrystals in biological detection," *Nature Biotechnology*, vol. 22, no. 1, pp. 47–52, 2004.
- [16] J. M. Klostranec and W. C. W. Chan, "Quantum dots in biological and biomedical research: recent progress and present challenges," *Advanced Materials*, vol. 18, no. 15, pp. 1953–1964, 2006.
- [17] P. Mulvaney, L. M. Liz-Marzán, M. Giersig, and T. Ung, "Silica encapsulation of quantum dots and metal clusters," *Journal of Materials Chemistry*, vol. 10, no. 6, pp. 1259–1270, 2000.
- [18] Y. Yang and M. Gao, "Preparation of fluorescent SiO₂ particles with single CdTe nanocrystal cores by the reverse microemulsion method," *Advanced Materials*, vol. 17, no. 19, pp. 2354–2357, 2005.
- [19] D. Gerion, F. Pinaud, S. C. Williams et al., "Synthesis and properties of biocompatible water-soluble silica-coated CdSe/ZnS semiconductor quantum dots," *Journal of Physical Chemistry B*, vol. 105, no. 37, pp. 8861–8871, 2001.
- [20] W. J. Parak, D. Gerion, T. Pellegrino et al., "Biological applications of colloidal nanocrystals," *Nanotechnology*, vol. 14, no. 7, pp. R15–R27, 2003.
- [21] F. Tamanoi, J. Lu, M. Liang, Z. Li, and J. I. Zink, "Biocompatibility, biodistribution, and drug-delivery efficiency of mesoporous silica nanoparticles for cancer therapy in animals," *Small*, vol. 6, no. 16, pp. 1794–1805, 2010.
- [22] C. Chang, S. H. Wu, Y. S. Lin et al., "Multifunctional mesoporous silica nanoparticles for intracellular labeling and animal magnetic resonance imaging studies," *ChemBioChem*, vol. 9, no. 1, pp. 53–57, 2008.
- [23] D. Wang, J. Qian, F. Cai, S. He, S. Han, and Y. Mu, "'Green'-synthesized near-infrared PbS quantum dots with silica-PEG dual-layer coating: ultrastable and biocompatible optical probes for in vivo animal imaging," *Nanotechnology*, vol. 23, no. 24, pp. 245701–245702, 2012.
- [24] P. Pericleous, M. Gazouli, A. Lyberopoulou, S. Rizos, N. Nikiteas, and E. P. Efstathopoulos, "Quantum dots hold promise for early cancer imaging and detection," *International Journal of Cancer*, vol. 131, no. 3, pp. 519–528, 2012.
- [25] D. Richards and A. Ivanisevic, "Inorganic material coatings and their effect on cytotoxicity," *Chemical Society Reviews*, vol. 41, no. 6, pp. 2052–2060, 2012.
- [26] C. V. Durgadas, K. Sreenivasan, and C. P. Sharma, "Bright blue emitting CuSe/ZnS/silica core/shell/shell quantum dots and their biocompatibility," *Biomaterials*, vol. 33, no. 27, pp. 6420–6429, 2012.
- [27] S. T. Selvanb, "Silica-coated quantum dots and magnetic nanoparticles for bioimaging applications (Mini-Review)," *Biointerphases*, vol. 5, no. 3, pp. FA110–FA115, 2010.
- [28] M. Ohmori and E. Matijević, "Preparation and properties of uniform coated inorganic colloidal particles. 8. Silica on iron," *Journal of Colloid And Interface Science*, vol. 160, no. 2, pp. 288–292, 1993.
- [29] L. M. Liz-Marzán and A. P. Philipse, "Synthesis and optical properties of gold-labeled silica particles," *Journal of Colloid And Interface Science*, vol. 176, no. 2, pp. 459–466, 1995.
- [30] A. Guerrero-Martínez, J. Pérez-Juste, and L. M. Liz-Marzán, "Recent progress on silica coating of nanoparticles and related nanomaterials," *Advanced Materials*, vol. 22, no. 11, pp. 1182–1195, 2010.
- [31] L. M. Liz-Marzán, M. Giersig, and P. Mulvaney, "Homogeneous silica coating of vitreophobic colloids," *Chemical Communications*, no. 6, pp. 731–732, 1996.

- [32] L. M. Liz-Marzán, M. Giersig, and P. Mulvaney, "Synthesis of nanosized gold-silica core-shell particles," *Langmuir*, vol. 12, no. 18, pp. 4329–4335, 1996.
- [33] L. Chen, C. Chen, R. Li, Y. Li, and S. Liu, "CdTe quantum dot functionalized silica nanosphere labels for ultrasensitive detection of biomarker," *Chemical Communications*, no. 19, pp. 2670–2672, 2009.
- [34] T. T. Tan, S. T. Selvan, L. Zhao, S. Gao, and J. Y. Ying, "Size control, shape evolution, and silica coating of near-infrared-emitting PbSe quantum dots," *Chemistry of Materials*, vol. 19, no. 13, pp. 3112–3117, 2007.
- [35] S. T. Selvan, T. T. Tan, and J. Y. Ying, "Robust, non-cytotoxic, silica-coated CdSe quantum dots with efficient photoluminescence," *Advanced Materials*, vol. 17, no. 13, pp. 1620–1625, 2005.
- [36] D. K. Yi, S. T. Selvan, S. S. Lee, G. C. Papaefthymiou, D. Kundaliya, and J. Y. Ying, "Silica-coated nanocomposites of magnetic nanoparticles and quantum dots," *Journal of the American Chemical Society*, vol. 127, no. 14, pp. 4990–4991, 2005.
- [37] S. T. Selvan, T. T. Y. Tan, D. K. Yi, and N. R. Jana, "Functional and multifunctional nanoparticles for bioimaging and biosensing," *Langmuir*, vol. 26, no. 14, pp. 11631–11641, 2010.
- [38] E. Pösel, C. Schmidtke, S. Fischer et al., "Tailor-made quantum dot and iron oxide based contrast agents for in vitro and in vivo tumor," *ACS Nano*, vol. 6, no. 4, pp. 3346–3353, 2012.
- [39] W. Liu, H. S. Choi, J. P. Zimmer, E. Tanaka, J. V. Frangioni, and M. Bawendi, "Compact cysteine-coated CdSe(ZnCdS) quantum dots for in vivo applications," *Journal of the American Chemical Society*, vol. 129, no. 47, pp. 14530–14531, 2007.
- [40] H. S. Choi, W. Liu, P. Misra et al., "Renal clearance of quantum dots," *Nature Biotechnology*, vol. 25, no. 10, pp. 1165–1170, 2007.
- [41] B. Tian, W. T. Al-Jamal, J. V. Bossche, and K. Kostarelos, "Design and engineering of multifunctional quantum dot-based nanoparticles for simultaneous therapeutic-diagnostic applications," *Nanostructure Science and Technology*, part 4, pp. 345–365, 2012.
- [42] S. B. Lowe, J. A. G. Dick, B. E. Cohen, and M. M. Stevens, "Multiplex sensing of protease and kinase enzyme activity via orthogonal coupling of quantum dot-peptide conjugates," *ACS Nano*, vol. 6, no. 1, pp. 851–857, 2012.
- [43] K. T. Yong, H. Ding, I. Roy et al., "Imaging pancreatic cancer using bioconjugated inq quantum dots," *ACS Nano*, vol. 3, no. 3, pp. 502–510, 2009.
- [44] H. S. Choi, B. I. Ipe, P. Misra, J. H. Lee, M. G. Bawendi, and J. V. Frangioni, "Tissue- and organ-selective biodistribution of NIR fluorescent quantum dots," *Nano Letters*, vol. 9, no. 6, pp. 2354–2359, 2009.
- [45] X. Yu, L. Chen, Y. Deng et al., "Fluorescence analysis with quantum dot probes for hepatoma under one- and two-photon excitation," *Journal of Fluorescence*, vol. 17, no. 2, pp. 243–247, 2007.
- [46] D. K. Tiwari, S. I. Tanaka, Y. Inouye, K. Yoshizawa, T. M. Watanabe, and T. Jin, "Synthesis and characterization of anti-HER2 antibody conjugated CdSe/CdZnS quantum dots for fluorescence imaging of breast cancer cells," *Sensors*, vol. 9, no. 11, pp. 9332–9354, 2009.
- [47] Z. Li, P. Huang, R. He et al., "Aptamer-conjugated dendrimer-modified quantum dots for cancer cell targeting and imaging," *Materials Letters*, vol. 64, no. 3, pp. 375–378, 2010.
- [48] D. A. Geraldo, E. F. Duran-Lara, D. Aguayo et al., "Supramolecular complexes of quantum dots and a polyamidoamine (PAMAM)-folate derivative for molecular imaging of cancer cells," *Analytical and Bioanalytical Chemistry*, vol. 400, no. 2, pp. 483–492, 2011.
- [49] M. Akin, R. Bongartz, J. G. Walter et al., "PAMAM-functionalized water soluble quantum dots for cancer cell targeting," *Journal of Materials Chemistry*, vol. 22, no. 23, pp. 11529–11536, 2012.
- [50] T. Jin, F. Fujii, Y. Komai, J. Seki, A. Seiyama, and Y. Yoshioka, "Preparation and characterization of highly fluorescent, glutathione-coated near infrared quantum dots for in vivo fluorescence imaging," *International Journal of Molecular Sciences*, vol. 9, no. 10, pp. 2044–2061, 2008.
- [51] M. Han, X. Gao, J. Z. Su, and S. Nie, "Quantum-dot-tagged microbeads for multiplexed optical coding of biomolecules," *Nature Biotechnology*, vol. 19, no. 7, pp. 631–635, 2001.
- [52] G. Wang, P. Zhang, H. Dou et al., "Efficient incorporation of quantum dots into porous microspheres through a solvent-evaporation approach," *Langmuir*, vol. 28, no. 14, pp. 6141–6150, 2012.
- [53] D. Wang, A. L. Rogach, and F. Caruso, "Semiconductor quantum dot-labeled microsphere bioconjugates prepared by stepwise self-assembly," *Nano Letters*, vol. 2, no. 8, pp. 857–861, 2002.
- [54] M. Adamczaka, H. J. Hoelb, G. Gaudernackb, J. Barbasza, K. Szczepanowicz, and P. Warszyńska, "Polyelectrolyte multilayer capsules with quantum dots for biomedical applications," *Colloids and Surfaces B*, vol. 90, no. 1, pp. 211–216, 2012.
- [55] Z. Zhelev, H. Ohba, and R. Bakalova, "Single quantum dot-micelles coated with silica shell as potentially non-cytotoxic fluorescent cell tracers," *Journal of the American Chemical Society*, vol. 128, no. 19, pp. 6324–6325, 2006.
- [56] P. Zhang, Y. He, Z. Ruan, F. F. Chen, and J. Yang, "Fabrication of quantum dots-encoded microbeads with a simple capillary fluidic device and their application for biomolecule detection," *Journal of Colloid and Interface Science*, vol. 385, no. 1, pp. 8–14, 2012.
- [57] Q. Yang, Y. Li, T. Song, and J. Chang, "Facile single step preparation of high-performance quantum dot barcodes," *Journal of Materials Chemistry*, vol. 22, no. 14, pp. 7043–7049, 2012.
- [58] J. Lee, Y. Choi, K. Kim et al., "Characterization and cancer cell specific binding properties of anti-EGFR antibody conjugated quantum dots," *Bioconjugate Chemistry*, vol. 21, no. 5, pp. 940–946, 2010.
- [59] T. Pellegrino, L. Manna, S. Kudera et al., "Hydrophobic nanocrystals coated with an amphiphilic polymer shell: a general route to water soluble nanocrystals," *Nano Letters*, vol. 4, no. 4, pp. 703–707, 2004.
- [60] N. Travert-Branger, F. Dubois, O. Carion et al., "Oligomeric PEG-phospholipids for solubilization and stabilization of fluorescent nanocrystals in water," *Langmuir*, vol. 24, no. 7, pp. 3016–3019, 2008.
- [61] J. Liu, X. Yang, K. Wang et al., "Single nanoparticle imaging and characterization of different phospholipid-encapsulated quantum dot micelles," *Langmuir*, vol. 28, no. 28, pp. 10602–10609, 2012.
- [62] N. Travert-Branger, F. Dubois, J. P. Renault et al., "In situ electron-beam polymerization stabilized quantum dot micelles," *Langmuir*, vol. 27, no. 8, pp. 4358–4361, 2011.
- [63] B. Dubertret, P. Skourides, D. J. Norris, V. Noireaux, A. H. Brivanlou, and A. Libchaber, "In vivo imaging of quantum dots encapsulated in phospholipid micelles," *Science*, vol. 298, no. 5599, pp. 1759–1762, 2002.

- [64] R. Hu, K. T. Yong, I. Roy et al., "Functionalized near-infrared quantum dots for in vivo tumor vasculature imaging," *Nanotechnology*, vol. 21, no. 14, Article ID 145105, 2010.
- [65] F. Erogbogbo, K. T. Yong, R. Hu et al., "Biocompatible magnetofluorescent probes: luminescent silicon quantum dots coupled with superparamagnetic iron(III) oxide," *ACS Nano*, vol. 4, no. 9, pp. 5131–5138, 2010.
- [66] D. P. Cormode, T. Skajaa, M. M. Van Schooneveld et al., "Nanocrystal core high-density lipoproteins: a multimodality contrast agent platform," *Nano Letters*, vol. 8, no. 11, pp. 3715–3723, 2008.
- [67] O. Carion, B. Mahler, T. Pons, and B. Dubertret, "Synthesis, encapsulation, purification and coupling of single quantum dots in phospholipid micelles for their use in cellular and in vivo imaging," *Nature Protocols*, vol. 2, no. 10, pp. 2383–2390, 2007.
- [68] R. Koole, M. M. Van Schooneveld, J. Hilhorst et al., "Paramagnetic lipid-coated silica nanoparticles with a fluorescent quantum dot core: a new contrast agent platform for multimodality imaging," *Bioconjugate Chemistry*, vol. 19, no. 12, pp. 2471–2479, 2008.
- [69] K. T. Yong, "Biophotonics and biotechnology in pancreatic cancer: cyclic RGD-peptide-conjugated type II quantum dots for in vivo imaging," *Pancreatology*, vol. 10, no. 5, pp. 553–564, 2010.
- [70] K. T. Yong, I. Roy, W. C. Law, and R. Hu, "Synthesis of cRGD-peptide conjugated near-infrared CdTe/ZnSe core-shell quantum dots for in vivo cancer targeting and imaging," *Chemical Communications*, vol. 46, no. 38, pp. 7136–7138, 2010.
- [71] V. V. Klimov, M. Ducloy, and V. S. Letokhov, "Strong interaction between a two-level atom and the whispering-gallery modes of a dielectric microsphere: quantum-mechanical consideration," *Physical Review A*, vol. 59, no. 4, pp. 2996–3014, 1999.
- [72] J. N. Cha, M. H. Bartl, M. S. Wong, A. Popitsch, T. J. Deming, and G. D. Stucky, "Microcavity lasing from block peptide hierarchically assembled quantum dot spherical resonators," *Nano Letters*, vol. 3, no. 7, pp. 907–911, 2003.
- [73] X. Fan, M. C. Lonergan, Y. Zhang, and H. Wang, "Enhanced spontaneous emission from semiconductor nanocrystals embedded in whispering gallery optical microcavities," *Physical Review B*, vol. 64, no. 11, Article ID 115310, 5 pages, 2001.
- [74] W. Sheng, S. Kim, J. Lee, S. W. Kim, K. Jensen, and M. G. Bawendi, "In-situ encapsulation of quantum dots into polymer microspheres," *Langmuir*, vol. 22, no. 8, pp. 3782–3790, 2006.

Research Article

Gold Nanorod-Mediated Photothermal Modulation for Localized Ablation of Cancer Cells

Yoochan Hong,¹ Eugene Lee,² Jihye Choi,³ Seung Jae Oh,^{2,4,5} Seungjoo Haam,^{3,4}
Yong-Min Huh,^{2,4,6} Dae Sung Yoon,¹ Jin-Suck Suh,^{2,4,6} and Jaemoon Yang^{2,4,5}

¹ Department of Biomedical Engineering, Yonsei University, 234 Maeji, Heungup, Gangwondo, Wonju 220-710, Republic of Korea

² Department of Radiology, College of Medicine, Yonsei University, Sinchon, Seodaemun, Seoul 120-752, Republic of Korea

³ Department of Chemical and Biomolecular Engineering, Yonsei University, Sinchon, Seodaemun, Seoul 120-749, Republic of Korea

⁴ YUHS-KRIBB Medical Convergence Research Institute, Sinchon, Seodaemun, Seoul 120-752, Republic of Korea

⁵ Severance Integrative Research Institute for Cerebral & Cardiovascular Diseases, Yonsei University Health System, Seoul 120-752, Republic of Korea

⁶ Severance Biomedical Science Institute (SBSI), Shinchon, Seodaemun, Seoul 120-752, Republic of Korea

Correspondence should be addressed to Jin-Suck Suh, jss@yuhs.ac and Jaemoon Yang, 177hum@yuhs.ac

Received 15 August 2012; Accepted 20 September 2012

Academic Editor: Haiya Li

Copyright © 2012 Yoochan Hong et al. This is an open access article distributed under the Creative Commons Attribution License, which permits unrestricted use, distribution, and reproduction in any medium, provided the original work is properly cited.

We estimated the photothermal transduction efficiency of gold nanorod (GNR) solutions for different GNR concentrations and irradiation laser power. In particular, we verified that the degree of cell death area could be modulated by GNR concentration and irradiation laser power. The efficacy of GNR-produced photothermal ablation of cancer cells was evaluated by irradiating GNRs in the presence of MDA-MB-231 breast cancer cells with a near-infrared (NIR) laser at different laser power densities and irradiation times. GNR-induced photothermal ablation was applied successfully to cancer cells at various NIR laser power densities and irradiation times and was characterized with live-dead cell staining. Through these techniques, we established the system for not only verification of induced photothermal effect using NIR laser and thermocouple, but also identification of uptake efficiency for GNRs and cell viability using dark field and fluorescence imaging, respectively.

1. Introduction

Photothermal cancer therapy using nanostructures has been an attractive technique for the localized ablation of target cancer cells in a minimally invasive manner [1]. Near-infrared (NIR) light is particularly useful for photothermal therapies because biological tissues are relatively transparent to NIR light [2]. To maximize the photothermal effects, it is important to manufacture well-tailored nanostructures that can absorb NIR light well to transform into heat for localized target cell ablation [3–5]. Recently, there have been many photothermal studies using various nanostructures such as carbon nanotubes [6], gold nanoparticles (GNPs) [7], and gold nanorods (GNRs) [8]. Among them, GNRs are particularly attractive because their longitudinal surface plasmon band is tunable by adjusting the aspect ratio of the rod (length/width) [9]. The longitudinal surface plasmon

band for GNRs is located in the NIR region. Photon excitation of the surface plasmon band of GNRs by NIR light oscillates the free electron cloud. The kinetic energy of the oscillating electrons is then conveyed to the lattice of GNRs through electron-phonon coupling. Accordingly, the lattice also oscillates, and the GNRs reach thermal equilibrium with their environment through heat dissipation [9]. Although substantial efforts have been devoted to photothermal therapy, most previous research has focused on target cell viability after photothermal agent internalization and NIR light exposure and has neglected characterization of the influence of specific conditions, for example, light power density, concentration of agents, and light exposure time, on the generation of heat and the subsequent temperature changes.

In this study, we modulated photothermal effects of GNRs solutions subjected to NIR laser irradiation under

various conditions (i.e., changing power density of NIR laser and GNR concentration). Results were compared to those using GNP solutions as a control photothermal agent. The temperature elevation rates were estimated for each concentration of GNR and GNP solution. The rate of temperature elevation and the photothermal transduction efficiency (the ratio of the energy converted to heat to the energy delivered from by the NIR laser) were measured for each sample. Finally, GNR solutions with high photothermal transduction efficiency were used to ablate MDA-MB-231 breast cancer cells at various NIR laser irradiation powers and durations. Using a series of these processes, we developed the versatile system that can measure the temperature elevation rate of solutions, detect the uptake of photothermal agents, and diagnose the cell viability.

2. Experimental Methods

2.1. Preparation of Gold Nanorods (GNRs). Monodispersed GNRs were synthesized by a seed-mediated growth method according to a previously published protocol, with some modification [10]. In brief, for the preparation of gold seed solution, 0.25 mL of $\text{HAuCl}_4 \cdot 3\text{H}_2\text{O}$ (100 mM) and 7.5 mL of hexadecyltrimethylammonium bromide (CTAB) solution (95 mM) were mixed, and 0.06 mL of ice-cold sodium borohydride solution (100 mM) was added to the mixture under vigorous stirring. The solution mixture was allowed to react for 2 minutes and was stored at room temperature for 3 hours. A growth solution containing 80 μL of silver nitrate solution (100 mM) was prepared by addition of 0.5 mL of $\text{HAuCl}_4 \cdot 3\text{H}_2\text{O}$ (100 mM) and 9.5 mL of CTAB solution (95 mM) under vigorous stirring. After the addition of 55 μL of ascorbic acid solution (100 mM), the color of the solution changed from yellow to colorless. 12 μL of gold seed solution was introduced into the growth solution and stirred for 10 seconds. The product solution was maintained for 24 hours at room temperature without disturbing, and its color changed from colorless to reddish-brown as time went on. The GNR solutions were centrifuged twice at 15,000 rpm for 30 minutes to remove excess CTAB molecules and were then redispersed in 5 mL of deionized water.

2.2. Preparation of Gold Nanoparticles (GNPs). Monodispersed GNPs were also synthesized using a previously published protocol as a control photothermal agent for comparison to GNRs [11]. In brief, GNPs were prepared by the reduction of 1.0 wt% tetrachloroaurate(III) trihydrate (2 mL) in the presence of 80 wt% tetrakis(hydroxymethyl) phosphonium chloride (12 μL) and NaOH (0.5 mL of 1 M) as reducing agents for 10 minutes at room temperature.

2.3. Preparation of PEGylated GNRs (PGNRs). Monodispersed PGNRs were prepared using a previously published protocol [12]. To prepare PGNRs, GNRs were coated with heterobifunctionalized PEG (CM-PEG-SH) as a stabilizer. 50 mg of CM-PEG-SH was added to 5 mL of GNR solution and stirred for 48 hours at room temperature. The mixture was centrifuged at 15,000 rpm for 30 minutes to remove

unbound CM-PEG-SH molecules and resuspended in 5 mL of PBS.

2.4. Characterization of Photothermal Agents. The absorbance of GNRs and GNPs was measured using UV-Vis spectrometer (UV1800, Shimadzu). The chemical structure of the PGNRs was analyzed using a proton-nuclear magnetic resonance ($^1\text{H-NMR}$) spectrometer (JUM-ECP300, JEOL Ltd.) with dideuterium oxide as solvent. The quantities of Au in GNRs and GNPs were determined using inductively coupled plasma atomic emission spectrometry (ICP-AES, Thermo Electron corporation).

2.5. Photothermal Effect Measurement. To prepare samples for photothermal effect studies, 320 μL GNR solutions (0.0295, 0.0394, 0.0492, and 0.0591 mg/mL) and GNP solutions (0.0125, 0.025, 0.05, and 0.1 mg/mL) were prepared in glass vials. The samples were kept at room temperature for at least 30 minutes prior to irradiation to establish a steady-state temperature. The sample vials were enclosed within styrofoam vial racks and were irradiated with an 808 nm diode laser (JOLD-30-FC-12, JENOPTIK) with a 1 mm beam diameter for one minute at power densities of 0.25, 0.5, 1.0, or 2.0 W/cm^2 , respectively. Temperature elevations of GNR and GNP solutions irradiated with a NIR laser were measured using thermocouple (True RMS Multimeter 287, Fluke).

2.6. Cellular Uptake. The uptake efficiency of PGNRs by MDA-MB-231 cells was assessed from dark field images using a high numerical aperture dark field condenser (U-DCW, Olympus), which delivers a very narrow beam of white light from a tungsten halogen lamp to the surface of the sample. Immersion oil (nd: 1.516, Olympus) was used to narrow the gap between the condenser and the glass slide and to balance the refractive index. The dark field images were captured using an Olympus CCD camera.

2.7. Photothermal Ablation of Cancer Cells. To test the photothermal ablation potential of the GNRs, MDA-MB-231 breast cancer cells (5×10^4 cells/well) were incubated using a previously published protocol [9]. The distributions of the live and dead cells were observed using an fluorescence imaging system based on commercial microscopic system (BX51, Olympus) after cellular staining with an acetomethoxy derivative of calcein (calcein AM: live cells) and ethidium bromide (EthBr: dead cells).

3. Results and Discussion

The absorption peaks of GNRs at 520 and 780 nm (UV1800, Shimadzu) due to the oscillation of electrons along the transverse and longitudinal axes of the nanorod, respectively (Figure 1), were in good agreement with previous studies [13]. In contrast to GNRs, GNPs, which maintain a more uniform geometry, only had a peak at 520 nm. Collectively, these results suggest that GNRs have the potential for more efficient photothermal conversion than GNPs in the NIR region.

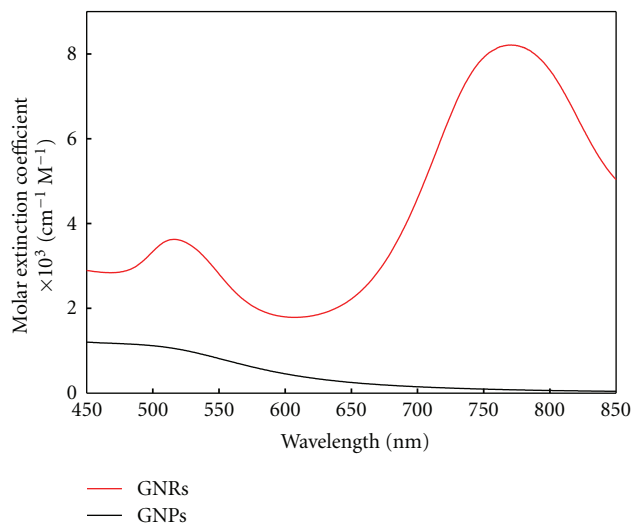


FIGURE 1: Molar extinction coefficient spectra of GNR and GNP solutions.

To investigate the photothermal effects of the samples, first, we designed optical system that optimized for irradiation of NIR laser. A schematic illustration of the temperature measurement system is shown in Figure 2(a). Styrofoam vial racks insulated the samples from ambient temperature variations to improve the accuracy of the measurement of temperature elevations. Temperature elevation rates were estimated from temperature differences during the initial 10 seconds of each experiment. The sample temperatures increased almost linearly with power density. Greater temperature increases were observed with GNR solutions at higher GNR concentrations and higher NIR laser power density, whereas the temperature of GNP solutions increased almost the same degree regardless of the GNP concentration. Linear fits of the temperature elevation rate of each GNR and GNP solution as functions of irradiated power density confirmed these observations (Figure 2(b)).

The photothermal transduction efficiency for each sample was also estimated using previously published calculation method [14]. First, the energy received by each solution used $Q = cm\Delta T$ (where Q is calories, c is specific heat, m is mass, and ΔT is the temperature variation). The specific heat of the solution was assumed to be the same as water ($c_{\text{water}} = 4.179 \text{ J/g}^\circ\text{C}$). The energy delivered to the solutions by NIR laser irradiation was determined as $J = Ws$ (where J is energy, W is laser power, and s is time). The photothermal transduction efficiency η was then estimated as the ratio of the energy received to the energy delivered: $\eta = Q/J$. Figure 2(c) shows the photothermal transduction efficiency of GNR and GNP solutions as a function of mass concentration. Photothermal transduction efficiency increased with increasing GNR concentration (slope = 5.97), whereas the efficiency was nearly constant for GNP solutions (slope = 0.08). The sensitivity of efficiency to the GNR concentration suggests that GNR solutions are suitable as photothermal ablation agents.

Accordingly, the GNR solutions were then used as photothermal ablation agents for cancer cells. A schematic of the approach for photothermal ablation of cancer cells is shown in Figure 3(a). To evaluate GNRs as potential cancer cell photothermal ablation agents, hexadecyltrimethylammonium bromide (CTAB) on the surface of the GNRs must be modified because CTAB molecules exhibit a cytotoxic phenomenon and cellular function interference due to its strong electric potential [15]. $^1\text{H-NMR}$ spectra were obtained to confirm the chemical structure of PGNRs (Figure 3(b)). The characteristic peaks of CTAB (3.1, 1.2, and 0.8 ppm, black line) were not detected, whereas that of PEG (3.6 ppm, red line) was observed in the PGNR spectra (blue line). The peaks at 4.8 ppm were characteristic of dideuterium oxide (D_2O) peaks from the solvent. These results indicated that the CTAB molecules were successfully exchanged with CM-PEG-SH molecules.

Figure 4(a) shows a dark field image of untreated MDA-MB-231 cells as a negative control. The MDA-MB-231 cells appeared dark blue in the dark field image. In Figure 4(b), the scattered light from internalized PGNRs was observed as a dark yellow spot. Images of live-dead stained cells are shown in Figure 5 using fluorescence microscopic imaging. Regions of dead cells stained with EthBr (red region) broaden with increasing laser power density and irradiation time. No damage was observed in samples that were not NIR irradiated, in samples irradiated with 5 W/cm^2 for 10 minutes, or irradiated with 40 W/cm^2 for 30 minutes on MDA-MB-231 cells without PGNRs loading. In samples irradiated with 10 W/cm^2 for 10 minutes, 20 W/cm^2 for 5 minutes, or 20 W/cm^2 for 10 minutes, black dark spots in the calcein AM staining images (first row) and red spots in the EthBr staining images (second row) were observed. The size of the spots did not match the 2 mm spot size of the laser. The laser irradiation spots were bigger than the black dark spot and the red spot in the calcein AM and EthBr stained images, respectively, most likely due to the Gaussian nature of the irradiating beam, which causes cells at the periphery of the laser spot to receive less power [16]. Consequently, the minimum temperature for cell ablation was not achieved, so the black dark spots in the calcein AM staining images and the red spots in the EthBr staining images were smaller than laser irradiation spots. When the cells were irradiated at 40 W/cm^2 for 30 minutes, the black spot in the calcein AM images was larger than the laser irradiation spot, indicating that the heat generated by the PGNRs increased the temperature above that necessary for cell death, and cells in adjacent areas outside the laser spot diameter were also ablated as the excessive heat dissipated away from the PGNRs. In the merged images (the third row), the doughnut-shaped black areas suggest that PGNR-generated heat caused cell shrinkage [16].

We suggest that it is necessary to integrate and optimize a system for investigation about photothermal effect of photothermal agents, uptake efficiency of photothermal agents toward the specific cell lines, and cell viability assay after light irradiation (Figure 6). Thus, we assembled techniques to observe the above-mentioned phenomenon in one place.

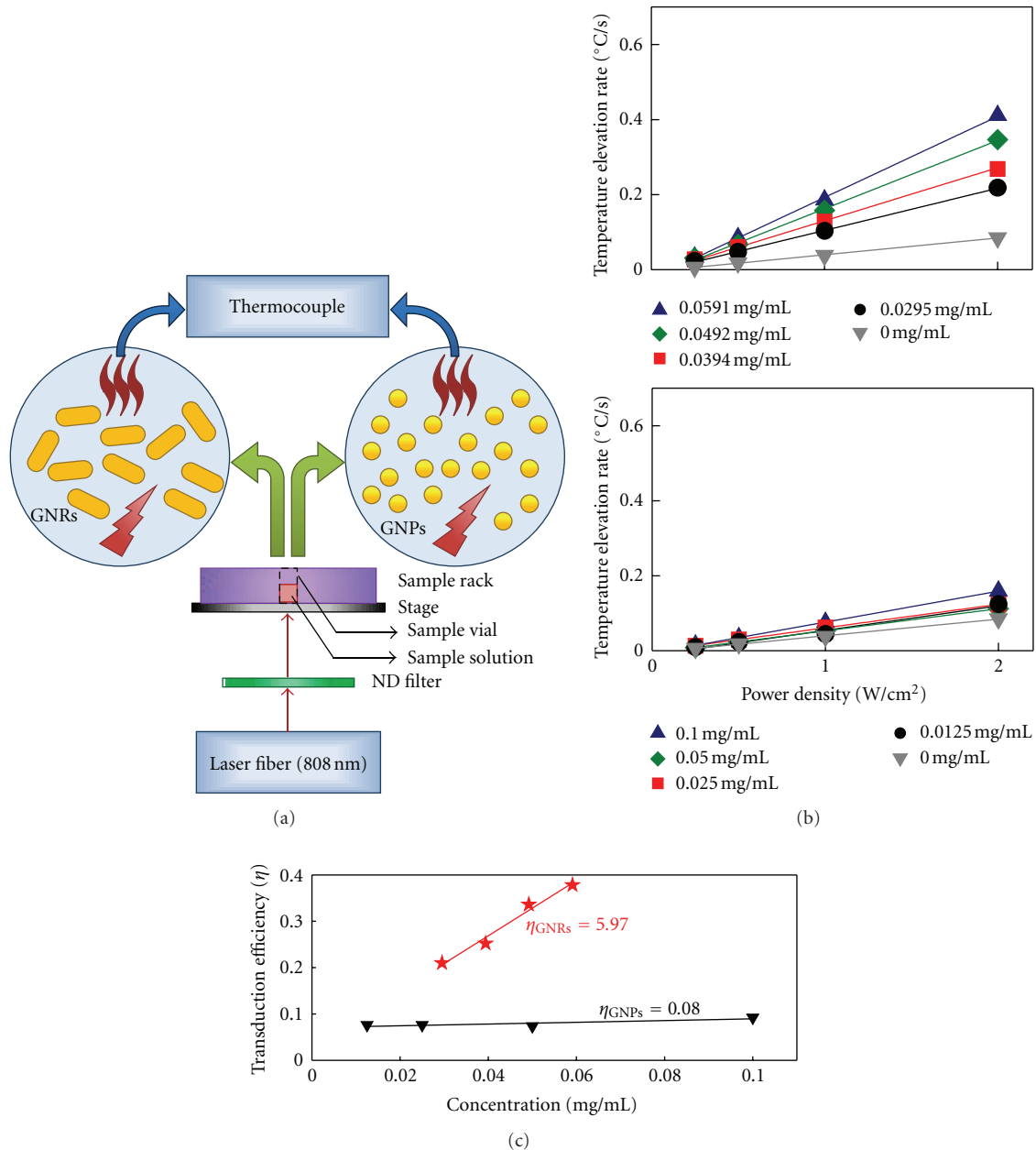


FIGURE 2: (a) Schematic illustration of temperature measurement system. (b) Temperature elevation rate as a function of power density for each GNR and GNP concentration; black: 0.0295 mg/mL, red: 0.0394 mg/mL, green: 0.0492 mg/mL, and blue: 0.0591 mg/mL for GNRs; black: 0.0125 mg/mL, red: 0.025 mg/mL, green: 0.05 mg/mL, and blue: 0.1 mg/mL for GNPs. (c) Photothermal transduction efficiencies of GNR and GNP solutions as a function of mass concentrations; black: GNPs, red: GNRs. Inserted numbers are slope values of each fitted graph.

Firstly, we designed optimized optical system for NIR laser irradiation. The wavelength of NIR laser was 808 nm and GNR have highest absorption in this wavelength, so this wavelength was suitable to investigate the photothermal effect of GNRs as photothermal agents. Second, we measured temperature of the samples in quasi-insulated system using thermocouple. The temperature elevation rate was analyzed depending on sample concentration and irradiated power density, and then, we calculated photothermal transduction

efficiency using simple mathematical methods for each sample. Third, we conducted dark field imaging for confirmation of GNR uptake efficiency toward the cancer cells. The MDA-MB-231 cells appeared dark blue, whereas internalized PGNRs were observed as a dark yellow spot. The dark field image analysis was reliable method for assessment of uptake efficiency as nanoparticles and cells have different light scattering colors. Finally, we classified live and dead cells using fluorescence images that have distinct color

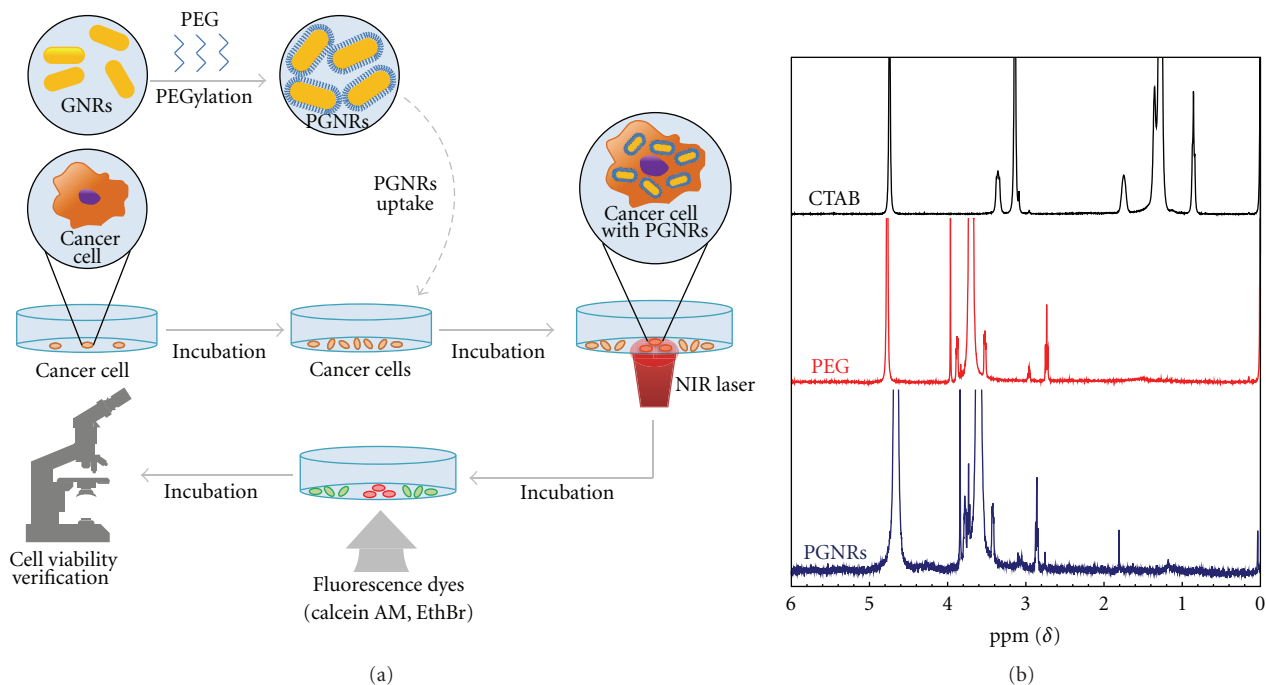


FIGURE 3: (a) Schematic of photothermal ablation with GNRs for cancer cells. (b) Proton-nuclear magnetic resonance ($^1\text{H-NMR}$) spectrum; black: CTAB, red: PEG, and blue: PGNRs.

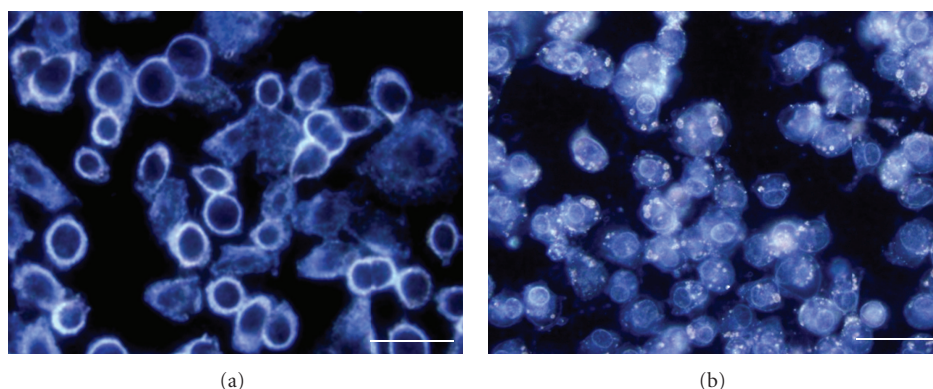


FIGURE 4: Dark field image of (a) nontreated MDA-MB-231 cells and (b) MDA-MB-231 cells treated with PGNRs. Scale bars: $20\ \mu\text{m}$. (c) Fluorescence images of MDA-MB-231 cells treated with PGNRs after NIR laser irradiation. Dotted lines mean NIR laser irradiated spot. Beam diameter of NIR laser is 2 mm. All scale bars: $400\ \mu\text{m}$.

differences according to cell viability. Moreover, we show that modulation of the degree for cell viability according to GNRs concentration and irradiation laser power. We propose a series of technique processes for assessment of photothermal effect at once because these techniques are essential for execution and evaluation of photothermal therapy.

4. Conclusions

In conclusion, we modulated the photothermal transduction capabilities of GNRs and GNPs solutions for the ablation of cancer cells. The temperature elevations induced by different concentrations of GNRs and GNPs solutions subjected to

different NIR laser power densities were measured. The temperature elevation rates of GNR and GNP solutions were calculated, and the efficiency of photothermal transduction was determined as a function of mass concentration. Finally, GNR-induced photothermal ablation was applied successfully to cancer cells at various NIR laser power densities and irradiation times and was characterized with live-dead cell staining. These results demonstrate the differences in photothermal transduction efficiency between GNRs and GNPs solutions and suggest that photothermal ablation of cancer cells is sensitive to this efficiency as well as the irradiation conditions. Based on these results, we propound a system for photothermal effect analysis. A set of separate techniques

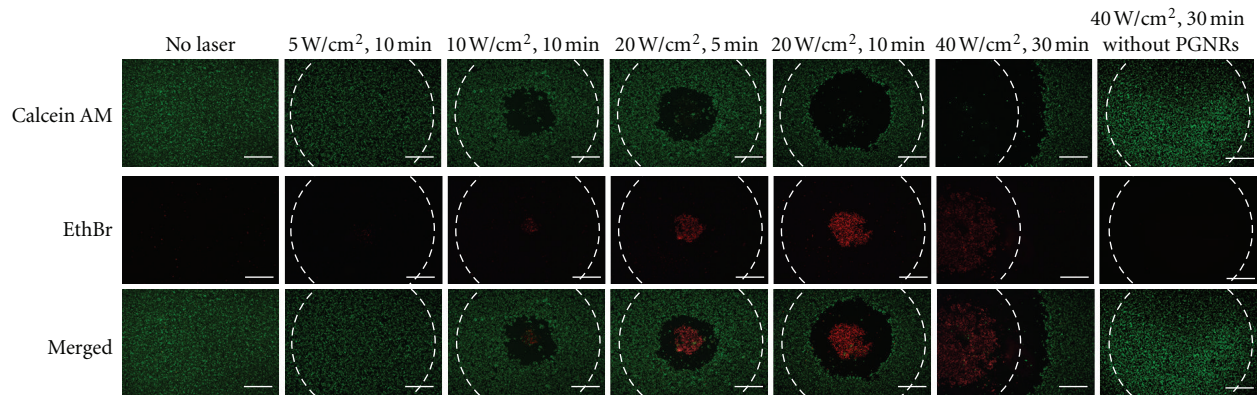


FIGURE 5: Fluorescence images of MDA-MB-231 cells treated with PGNRs after NIR laser irradiation. Dotted lines mean NIR laser irradiated spot. Beam diameter of NIR laser is 2 mm. All scale bars: $400\ \mu\text{m}$.

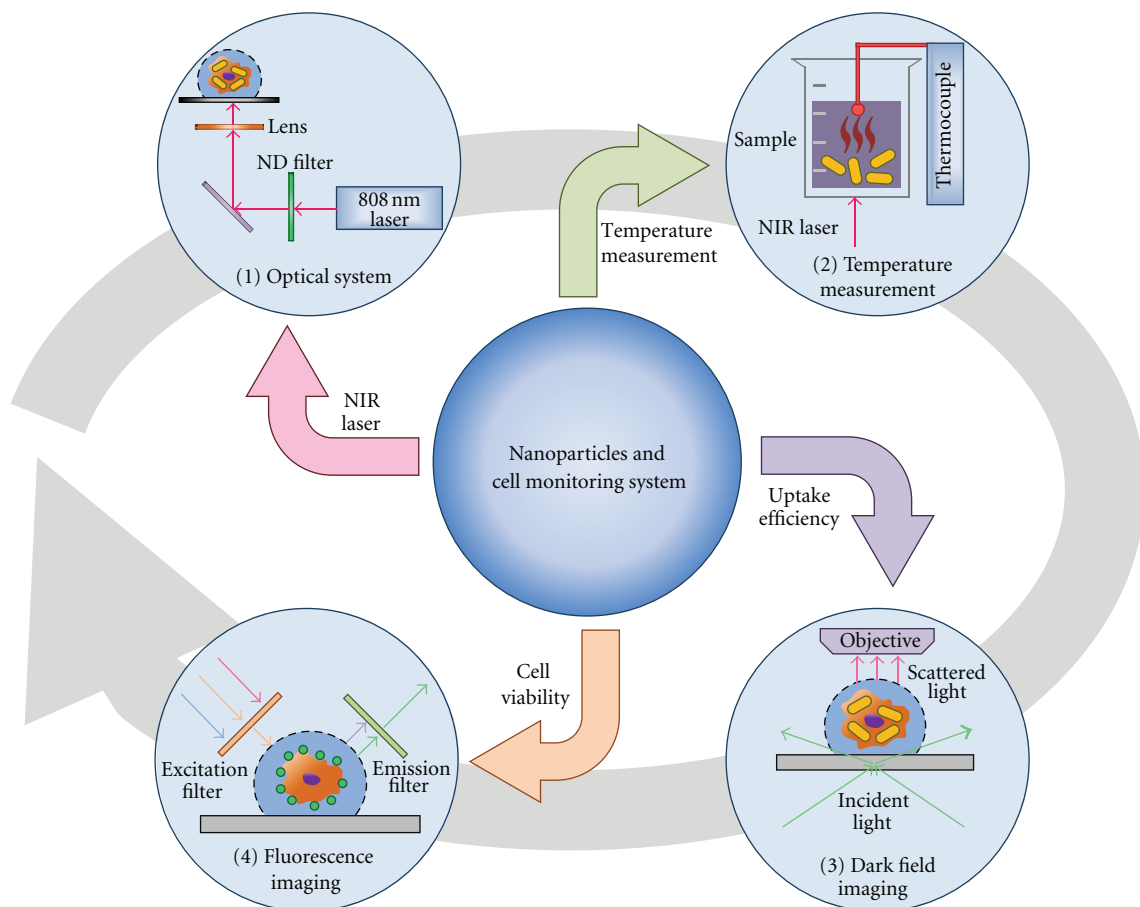


FIGURE 6: Schematic illustration of developed system for investigation of photothermal effect.

converged to a point with the aim of accurate evaluation for photothermal therapy. This system will present a way about precise photothermal therapy evaluation.

Conflict of Interests

The authors do not have a direct financial relation with the commercial identity mentioned in our paper (Shimadzu,

JEOL Ltd., Thermo Electron Corporation, JENOPTIK, Fluke, and Olympus).

Acknowledgments

This work was supported by the National Research Foundation (NRF) Grant funded by Korea Government, Ministry of Education and Science Technology (MEST) (2011-0026073).

This study was supported by a grant from the Korean Health Technology R&D Project of the Ministry for Health, Welfare & Family Affairs, Republic of Korea (A101954).

References

- [1] J. Yang, J. Lee, J. Kang et al., "Smart drug-loaded polymer gold nanoshells for systemic and localized therapy of human epithelial cancer," *Advanced Materials*, vol. 21, no. 43, pp. 4339–4342, 2009.
- [2] R. Weissleder, "A clearer vision for *in vivo* imaging," *Nature Biotechnology*, vol. 19, no. 4, pp. 316–317, 2001.
- [3] X. Huang, P. K. Jain, I. H. El-Sayed, and M. A. El-Sayed, "Gold nanoparticles: interesting optical properties and recent applications in cancer diagnostics and therapy," *Nanomedicine*, vol. 2, no. 5, pp. 681–693, 2007.
- [4] H. Park, J. Yang, J. Lee, S. Haam, I. H. Choi, and K. H. Yoo, "Multifunctional nanoparticles for combined doxorubicin and photothermal treatments," *ACS Nano*, vol. 3, no. 10, pp. 2919–2926, 2009.
- [5] P. K. Jain, I. H. El-Sayed, and M. A. El-Sayed, "Au nanoparticles target cancer," *Nano Today*, vol. 2, no. 1, pp. 18–29, 2007.
- [6] P. Chakravarty, R. Marches, N. S. Zimmerman et al., "Thermal ablation of tumor cells with antibody-functionalized single-walled carbon nanotubes," *Proceedings of the National Academy of Sciences of the United States of America*, vol. 105, no. 25, pp. 8697–8702, 2008.
- [7] X. Huang, P. K. Jain, I. H. El-Sayed, and M. A. El-Sayed, "Plasmonic photothermal therapy (PPTT) using gold nanoparticles," *Lasers in Medical Science*, vol. 23, no. 3, pp. 217–228, 2008.
- [8] H.-C. Huang, K. Rege, and J. J. Heys, "Spatiotemporal temperature distribution and cancer cell death in response to extracellular hyperthermia induced by gold nanorods," *ACS Nano*, vol. 4, no. 5, pp. 2892–2900, 2010.
- [9] S. Link and M. A. El-Sayed, "Shape and size dependence of radiative, non-radiative and photothermal properties of gold nanocrystals," *International Reviews in Physical Chemistry*, vol. 19, no. 3, pp. 409–453, 2000.
- [10] R. Choi, J. Yang, J. Choi et al., "Thiolated dextran-coated gold nanorods for photothermal ablation of inflammatory macrophages," *Langmuir*, vol. 26, no. 22, pp. 17520–17527, 2010.
- [11] J. Yang, K. Eom, E. K. Lim et al., "In situ detection of live cancer cells by using bioprobes based on Au nanoparticles," *Langmuir*, vol. 24, no. 21, pp. 12112–12115, 2008.
- [12] J. Choi, J. Yang, D. Bang et al., "Targetable gold nanorods for epithelial cancer therapy guided by near-IR absorption imaging," *Small*, vol. 8, no. 5, pp. 746–753, 2012.
- [13] S. Link, M. B. Mohamed, and M. A. El-Sayed, "Simulation of the optical absorption spectra of gold nanorods as a function of their aspect ratio and the effect of the medium dielectric constant," *The Journal of Physical Chemistry B*, vol. 103, no. 16, pp. 3073–3077, 1999.
- [14] F.-Y. Cheng, C.-T. Chen, and C.-S. Yeh, "Comparative efficiencies of photothermal destruction of malignant cells using antibody-coated silica@Au nanoshells, hollow Au/Ag nanospheres and Au nanorods," *Nanotechnology*, vol. 20, no. 42, Article ID 425104, 2009.
- [15] A. M. Alkilany, P. K. Nagaria, C. R. Hexel, T. J. Shaw, C. J. Murphy, and M. D. Wyatt, "Cellular uptake and cytotoxicity of gold nanorods: molecular origin of cytotoxicity and surface effects," *Small*, vol. 5, no. 6, pp. 701–708, 2009.
- [16] L. B. Carpin, L. R. Bickford, G. Agollah et al., "Immuno-conjugated gold nanoshell-mediated photothermal ablation of trastuzumab-resistant breast cancer cells," *Breast Cancer Research and Treatment*, vol. 125, no. 1, pp. 27–34, 2011.